AB INITIO MODELING OF MOLECULAR MAGNETS

RISHU KHURANA

A thesis submitted for partial fulfilment of the

degree of Doctor of Philosophy

Institute of Nano Science and Technology, Mohali,
Knowledge city, Sector-81, SAS Nagar, Manauli PO, Mohali 140306, Punjab, India
Indian Institute of Science Education and Research, Mohali,
Knowledge city, Sector-81, SAS Nagar, Manauli PO, Mohali 140306, Punjab, India

November 2022

Dedicated to my beloved husband...

Declaration

The work presented in this thesis has been carried out by me under the guidance of Prof. Md. Ehesan Ali at the Institute of Nano Science and Technology, Mohali. This work has not been submitted in part or in full for a degree, a diploma, or a fellowship to any other university or institute. Whenever contributions of others are involved, every effort is made to indicate this clearly, with due acknowledgement of collaborative research and discussions. This thesis is a bona fide record of original work done by me and all sources listed within have been detailed in the bibliography.

Rishu Khurana

In my capacity as the supervisor of the candidate's thesis work, I certify that the above statements by the candidate are true to the best of my knowledge.

Prof. Md. Ehesan Ali

Acknowledgment

This PhD has been a long-time dream, come true. Undertaking this PhD has been a remarkably rewarding experience for me and it would not have been possible without the support of many people. With a sense of gratitude, I extend immeasurable appreciation and deepest gratitude to the people who have been there beside me on this journey.

First and foremost, I would like to express my deepest gratitude and sincere thanks to my supervisor ***Prof. Md. Ehesan Ali*** for introducing me to this exciting research of molecular magnetism. His constant motivation, enthusiastic temperament, dedicated help, continuous support, out of box thinking helped me in all times of my research. He taught me how to raise new possibilities and how to use systematic thinking and serendipity to solve problems. He has always been very appreciative of my interest and provided me the privilege to choose my own problems. From the art of expressing the results in the form of manuscripts and presentations, broadening my critical thinking approach, to polishing my communication skills, my sincere appreciation to him for all these, which would be my lifelong treasures. I am extremely thankful to him for his constant guidance not only in research but also in other facets of my life.

I would like to extend my sincere thanks to my PhD committee members: ***Prof. Asish Pal*** and ***Dr. Jayamurugan Govindasamy*** for their insightful comments and feedback in the annual evaluation meetings. I would also like to thank ***Prof. Neetu Goel*** for being an external evaluator during my CSIR upgradation evaluation.

I am thankful to the ***Council of Scientific and Industrial Research (CSIR), India*** for providing me with the fellowship and to ***INST*** for the infrastructural and computational facilities. I acknowledge ***INST*** and ***DST-SERB*** for providing financial support to attend the international conference.

I had the pleasure of being in TSCM lab with ***Dr. Aashish Bhatt***, ***Dr. Prabhleen Kaur***, ***Shikha Sharma***, ***Ashima Bajaj***, ***Aritra Mukhopadhyay***, ***Shahjad Ali***, ***Sakshi Nain*** as my labmates. I would like to thank them for helping me proofread this thesis. ***Ashima Bajaj*** deserves a special mention for mentoring me in the initial days of my PhD, and for being a companion as a roommate and a friend. Thanks should also go to ***Sameer Gupta*** for a fruitful collaborative project. I am delighted to meet ***Manish***, ***Prateek***, ***Asesh*** and ***Ambuj*** as project and intern students. I am also grateful to ***Mrs. Anjum Ismail*** for always cheering us.

A heartfelt thanks goes to my friends- ***Mitali***, ***Himani***, ***Meenakshi***, ***Priyanka***, ***Tanvi*** for their pleasant and refreshing company.

This would not have been possible without the unconditional love and constant support from my family. My parents, who motivated me to pursue this path, and my parents-in-law, who always stood beside me. My brother-in-law, ***Pankaj***, who was just a call away and always supported me, my sis-in-law, ***Priyanka***, my sisters, ***Anjali*** and ***Sonam***, my brother, ***Sourabh***, and my brother-in-law, ***Robin***, who have always been constant source of energy and motivation in my tough times. Their infallible love and support have always been my strength. Much love to little ***Reyansh, Smayra, Arnav, Vivanshi*** for being my mood boosters. With heartfelt gratitude, I express my thanks to my grand-father who always inspired me to achieve my goals.

Finally, this thesis is dedicated to my husband, ***Dr. Raman Khurana***, who has made it all possible. *"Behind every successful woman, there is a man who is always progressive. And in my life, it's my husband."* Words fall short to express my gratitude for him. He was my go-to person on this journey. A best friend, a great mentor, the best advisor-my one in all person. His constant love, care, and confidence in me have taken the load off my shoulder.

Lastly, I bow down to the Almighty for giving me the strength to pursue this path.

Abstract

A surge toward the miniaturization of quantum technological devices has brought a burst of research in the field of molecular magnetism. Molecular magnets manifest promising applications in spin qubits and high-density data storage devices. However, obtaining such molecules that exhibit exotic magnetic properties at room temperature is the key challenge that limits its practical applications. First-principle based quantum chemical calculations provide a way to design and screen such magnetic molecules that will operate at finite temperatures. In this context, we have computationally investigated the magnetic properties of organometallic complexes that possess large magnetic anisotropy and are generally known as single-molecule magnets, along with metal-free organic molecular magnets that exhibit substantial isotropic ferromagnetic exchange interactions.

Single-molecule magnets (SMMs) are magnetically bi-stable molecules exhibiting slow relaxation of magnetization, which is characterized by an energy barrier, U_{eff}, to magnetic moment reversal. Although the field is primarily dominated by 4f systems due to large spin-orbit coupling in the lanthanides, the research on transition metal complexes has recently gained momentum due to their potential to create strongly coupled spin systems which is in complete contrast to the lanthanides complexes. In transition metal complexes, the large magnetic anisotropy is achieved by complexes exhibiting unquenched first-order orbital angular momentum which is manifested by complexes with high axial symmetry or low coordination numbers. Moreover, the transition metal complexes also show the phenomenon of spin-crossover brought out by the application of some external stimuli like temperature, pressure, magnetic field, etc. In this thesis, we have studied axially symmetric complexes in the presence and absence of equatorial ligands to obtain insights into magnetic anisotropy and spin-crossover properties employing density functional theory and multireference (e.g., CASSCF/NEVPT2) methods. In this regard, firstly the trigonal bipyramidal complexes based on Fe(III) are studied to probe the effect of the ligand environment on the ground-spin state and magnetic anisotropy of the complexes. Additionally, these complexes are stabilized in an intermediate spin as the ground state and are found to exhibit a high spin excited state in close vicinity of the ground state and thus are investigated for spin-crossover properties. It has been observed that magnetic anisotropy is significantly influenced by axial ligands. From these observations, we further advanced our studies to the more exotic systems based on Fe(I) bearing explicitly axial ligands. These systems provide enhancement in the magnetic anisotropy due to large unquenched orbital angular momentum. Thus, molecular engineering by the systematic reduction in the coordination number is proposed as a suitable strategy to enhance the magnetic anisotropy in the transition metal based SMMs.

Organic molecular magnets (OMMs) are magnetic materials in which the spin-carriers are based on organic moieties. Open-shell organic diradicals with large isotropic ferromagnetic exchange interactions, high-spin ground-states, and persistent stability at

room temperature are the holy grail of OMMs. In this thesis, we aim to design organic diradicals with strong ferromagnetic exchange interactions and a high-spin ground state based on stable radicals. In this context, at first, we studied the electronic structure of one of the super-stable, Blatter's radical. The unique delocalization of the spin density among the three nitrogen atoms provides the merostabilization to the radical. Subsequently, based on this radical, several diradicals are designed with the sole aim to enhance the magnetic exchange interactions. It has been observed that due to the delocalization of spin density on the three nitrogen atoms, the three micromagnetic centers are created at each radical center giving rise to a total of nine possible exchange pathways in the diradicals and the resultant of these multiple pathways provided the nature of exchange in the diradical. Additionally, we provided a unique strategy to tune the inherent diamagnetic zwitterionic ground-state of tetraphenylhexaazaanthracene (TPHA), a molecule embracing two Blatter's monomers, to antiferro- and ferromagnetically coupled diradicals by systematically increasing the length of the coupler between the two radical moieties.

Keywords: Single-Molecule Magnets, Organic Molecular Magnets, Magnetic anisotropy, Isotropic magnetic exchange interactions, Blatter's radical, DFT, CASSCF/NEVPT2.

Contents

List of Abbreviations

DFT	Density Functional Theory
BOA	Born-Oppenheimer Approximation
HF	Hartree-Fock
CSF	Configuration State Function
SD	Slater Determinant
CI	Configuration Interaction
KS	Kohn-Sham
LDA	Local Density Approximation
GGA	Generalized Gradient Approximation
B3LYP	Becke, 3-parameter, Lee–Yang–Parr
SCF	Self Consistent Field
MC-SCF	Multiconfigurational Self Consistent Field
CASSCF	Complete Active Space Self Consistent Field
SA-CASSCF	State Average Complete Active Space Self Consistent Field
SS-CASSCF	State Specific Complete Active Space Self Consistent Field
NEVPT2	N-Electron Valence Perturbation Theory
SMM	Single Molecule Magnets
SIM	Single Ion Magnets
ZFS	Zero Field Splitting
QTM	Quantum Tunneling of Magnetization
TA-QTM	Thermally Assisted Quantum Tunneling of Magnetization
OMM	Organic Molecular Magnets
SO	Spin Orbitals
HDvV	Heisenberg-Dirac-van Vleck
UDFT	Unrestricted Density Functional Theory
UHF	Unrestricted Hartree Fock
CAS-CI	Complete Active Space Configuration Interaction
BS	Broken-Symmetry
SF	Spin-Flip

CBS	Constraint Broken-Symmetry
SOMO	Singly Occupied Molecular Orbital
SOC	Spin-Orbit Coupling
BP	Breit Pauli
SSO	Spin-Same-Orbit
SOO	Spin-Other-Orbit
SOMF	Spin-Orbit Mean Field
SH	Spin Hamiltonian
Ze	Zeeman
HOMA	Harmonic Oscillator Model of Aromaticity
TBP	Trigonal Bipyramidal
SCO	Spin-Crossover
HS	High-Spin
IS	Intermediate-Spin
LS	Low-Spin
def2-TZVPP	Valence triple-zeta with two sets of polarization functions
DC	Direct Current
PBE	Perdew–Burke-Ernzerhof
TM	Transition Metal
Ln	Lanthanides
NHC	N-Heterocyclic carbene
CAAC	cyclic (alkyl)(amino)carbene
DDCI3	Difference dedicated CI 3-degrees of freedom
DKH	Douglas-Kroll-Hess
QDPT	Quasi-Degenerate Perturbation Theory
AILFT	Ab initio ligand field theory
CASPT2	Complete Active Space with 2nd Order Perturbation Theory
MS-CASPT2	Multi-State Complete Active Space with 2nd Order Perturbation Theory
ANO	Atomic Natural Orbitals
AMFI	Atomic Mean-Field spin-orbit Integral
KDs	Kramer Doublets
NN	Nitronyl Nitroxide
OVER	Oxoverdazyl
DTDA	Dithiadiazolyl
IN	Imino Nitroxide
TPHA	Tetraphenylhexaazaanthracene
CSS	Closed Shell Singlet
OSS	Open-Shell Singlet
T	Triplet

EDG	Electron Donating Group
EWG	Electron Withdrawing Group
RI	Resolution of Identity
TD-DFT	Time-Dependent Density Functional Theory
SF	Spin-Flip
UNO	Unrestricted Natural Orbital
HONO	Highest Occupied Natural Orbital
LUNO	Lowest Unoccupied Natural Orbital
LSCF	Local Self-Consistent Field
UNO	Unrestricted Natural Orbital

List of Figures

List of Tables

CHAPTER 1

Introduction

1.1 Molecular Magnets

The thrust towards the miniaturization of electronic devices led to the idea of utilizing molecules as magnets.[1] In comparison to today's devices, each bit created by molecular magnets is a thousand times smaller. As a result, molecular magnets could replace conventional storage devices, allowing for much higher storage capacities. The development of magnetic molecules has triggered the shift of research from magnetic "materials to molecules". Molecular magnets play a vital role in the emerging field of molecular electronics and spintronics. These materials are particularly attractive because their magnetic properties are highly tunable. Molecular magnets gained attention in the last few decades before which the idea of magnetism was limited to metallic and ionic lattices ranging from magnetite to iron. These magnetic molecules are characterized by either the presence of large magnetic anisotropy or substantial isotropic magnetic exchange interactions or both depending on the spin-containing system present in them. In this thesis, we have discussed two kinds of molecular magnets where the first part of the thesis focuses on transition-metal based single-molecule magnets (SMMs). The latter part deals with the study of metal-free organic molecular magnets (OMMs).

1.2 Single-Molecule Magnets (SMMs)

Single-molecule magnets are distinct molecules that show hysteresis loop and exhibit slow relaxation of magnetization below a certain temperature called blocking temperature (T_B). This slow relaxation of magnetization is characterized in terms of en-

ergy barrier, U_{eff}, to reversal of spin magnetic moment from one direction to another. The field of single-molecule magnets gained attention after the synthesis of $[Mn_{12}O_{12}(CH_3COO)_{16}(H_2O)_4].2CH_3COOH.4H_2O$ complex by Lis et al.[2] in 1980, however, it was characterized with the slow relaxation of magnetization in the absence of magnetic field by R. Sessoli in 1993.[3] As a result, the research in this area sparked a huge interest in the development of molecular magnets with possible applications in quantum computing,[4,5] molecular spintronics,[6,7] classical data storage,[8] molecular spin qubits,[9,10] magnetic sensors,[11–13] etc. Ultimately, the aim of these researches endeavors to attain magnetically bi-stable molecules which show blocking of magnetization at higher temperatures so as to be utilized in potential applications.

1.2.1 Magnetic Anisotropy

The origin of the magnetically bi-stable spin state is the presence of magnetic anisotropy in a complex, which separates the bi-stable ground states by an energy barrier (U_{eff}).[14] This is well-represented with a double-well potential energy diagram as plotted against magnetization direction (Figure 1.1a). For a molecule to possess SMM behavior, it is essential to have unpaired electrons with ground-spin state S. The magnetic anisotropy splits the M_S levels of a molecule with total spin S into $2S+1$ levels under zero field. This splitting of the degeneracy of the ground state in the absence of a magnetic field is known as zero-field splitting (ZFS). The energy barrier corresponding to the reversal of spin from one orientation to another is related to the ground-spin S and axial zero-field splitting (D) as

$$U_{eff} = |D|S^2 \tag{1.1}$$

$$U_{eff} = |D|\left(S^2 - \frac{1}{4}\right) \tag{1.2}$$

Eq. 1.1 and 1.2 corresponds to spin-reversal barriers for integral and non-integral spins respectively for the transition metal based SMMs.[15]

Now, when $D < 0$, the energy levels with the largest M_S states will be the lowest in energy. Each $M_S = \pm S$ sublevel has its own orientation along the axial anisotropy axis, and $M_S = S$ represents spin-up and $M_S = -S$ represents spin-down orientation. The switching of the orientation of the magnetization direction from $M_S = +S$ to $M_S = -S$, the system requires the energy barrier, U_{eff}. The difference between the highest excited state and its ground state determines the barrier value. It implies that if the system possesses thermal energy (E_T) less than U_{eff}, it will stay in the potential energy minima i.e., at $M_S = +S$ and will be unable to reorient its magnetic moment randomly. In contrast, when $D > 0$, the low energy levels will have the smallest M_S states and it leads to the inversion of the orientation of the sub-levels (Figure 1.1b). In this con-

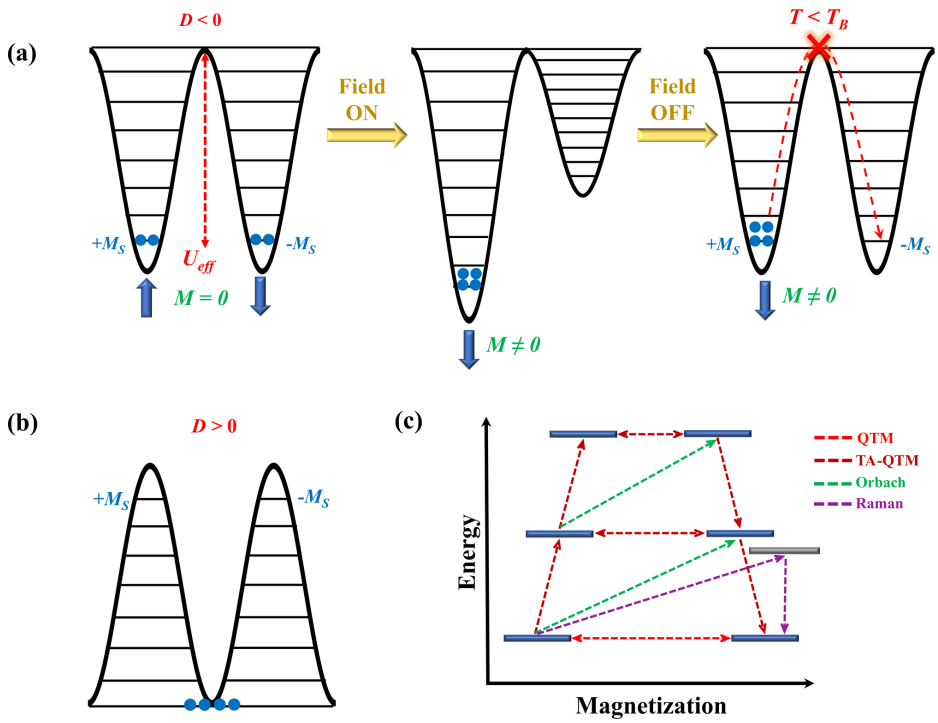

Figure 1.1: a) Double-well potential for complexes with $D < 0$ with magnetization projection in absence of external polarizing magnetic field (left), the magnetization of the complex under applied external magnetic field (center), and blocking of magnetization below T_B when the external magnetic field is turned off (right) (b) Inverted double-well potential for complexes with $D > 0$ (c) Different possible relaxation pathways in single-molecule magnets.

dition, the possibility of a bi-stable ground state is eliminated and hence, the complex does not show any SMM behavior, apart from some uncommon exceptions.[16,17] Therefore, the presence of negative D values characterizes SMMs. However, for lanthanide mononuclear complexes, S and L individually is not a good quantum number and the ground-state of these systems is best described by spin-orbit coupled quantum number J.

1.2.2 Relaxation of magnetization

For $M_S = \pm S$, when the magnetic field is absent, both the sub-levels are energetically degenerate and are equally populated. It implies the absence of magnetization in the system (Figure 1.1a, left). However, in the presence of an external polarizing magnetic field in a particular direction, one M_S sub-level gets lower in energy compared to the other M_S sub-level. It induces magnetization in the system as all the molecular spins orient in the same direction (Figure 1.1a, center). When the external polarizing magnetic field is removed, the ground state again gets energetically degenerate. Now if E_T

$> U_{eff}$, the system will again attain the equilibrium between the two orientations, and hence, the magnetization will be lost. Nevertheless, when $E_T < U_{eff}$, it will block the magnetization, and hence, the molecule will show magnetic behavior. This situation arises when $T < T_B$ (blocking temperature) (Figure 1.1a, right). From this understanding, it can be concluded that a higher energy barrier will lead to a higher magnetic retention temperature. Although, in reality, it does not always (or very often) work that way. In case, if reorienting the magnetization would only be possible by crossing the energy barrier all the way through the excited states, each and every system with $U_{eff} \sim 300$K would show SMM behavior and memory effect at room temperature. Nonetheless, because of their quantic nature, they possess complex and diverse relaxation mechanisms.[18] Usually, three spin-lattice relaxation mechanisms are prevalent in the complexes.[19]

1.2.2.1 Quantum Tunnelling of Magnetization (QTM)

Instead of crossing all the higher excited states to return to their original state after switching off the external polarizing magnetic field, when the particles tunnel through the opposite M_S (or M_J) states in the ground state, it is called QTM (represented by red lines in Fig. 1.1c). Although QTM is usually more apparent in systems with integral spins than in half-integral spin systems due to van Vleck's cancellation principle.[20] The probability of QTM increases when the mixing of coefficients of the opposite M_S states becomes high. For the half-integral spin systems, due to Kramer's theorem of degeneracy, the M_S states have negligibly small mixing of coefficients of opposite M_S states for a free ion providing extremely low probability for QTM. In contrast, for integral spin systems, due to the non-applicability of Kramer's theorem, there is strong mixing of coefficients of opposite M_S states leading to the splitting of non-Kramers states. For the later cases, instead of QTM, the term tunnel splitting is more generally used in the description of relaxation behavior. Therefore, the higher the tunnel splitting between the two-degenerate states, the faster the relaxation through that state.

1.2.2.2 Thermally Assisted Quantum Tunnelling of Magnetization (TA-QTM)

When the particles, instead of relaxing through the ground state via QTM, absorb the phonons and get excited to the higher state, and then, the relaxation occurs through the excited states with opposite M_S states, then the relaxation mechanism is known as TA-QTM. This relaxation pathway is shown by brown lines in Fig. 1.1c.

1.2.2.3 Orbach/Raman Relaxation

An Orbach process is the one in which the system absorbs phonon and jumps to the excited state and then the relaxation takes place to either of the ground $M_S = \pm S$ by the emission of phonon (green lines in Fig. 1.1c). It requires large energy for the Orbach process to take place, so, it mainly operates at higher temperatures.[21] Raman process is analogous to Orbach process with the exception that the relaxation is mediated by the virtual excited state (purple lines in Fig. 1.1c).[22]

In reality, there exist multiple relaxation pathways in a system, and depending on different temperatures, the various mechanisms are operational.

1.2.3 Polynuclear Single-Molecule Magnets

Followed by the characterization of the slow relaxation of magnetization in the Mn_{12} cluster with $S = 10$ ground state and an effective spin-reversal barrier of 43 cm^{-1},[3] many attempts were made to synthesize molecules with a significant spin-reversal barrier to magnetization. Since the spin reversal barrier scales as the power of 2 i.e., S^2 as shown in Eq. 1.1 and 1.2, it was believed that increasing the spin (S) in the system will enhance the U_{eff}. Nevertheless, several large-spin clusters were synthesized in an effort to obtain higher U_{eff}. In an attempt to increase the spin in the system, Fe_{19} cluster was synthesized by Heath and co-workers with S=33/2 ground-state. However, the spin reversal barrier of 11 cm^{-1} was reported for the cluster.[23] Further, Christou et al. synthesized the Mn_{25} complex with $S = 51/2$, however, with no significant enhancement in the U_{eff} which was reported to be 14 cm^{-1}.[24] Subsequently, a much higher ground-spin state of S=83/2 arising due to ferromagnetic couplings of all the metal centers was reported in Mn_{19} cluster but with a negligibly small $U_{eff} \sim 0$ cm^{-1}.[25] Similarly, Fe_{42} with all the metals coupled ferromagnetically leading to the large ground-spin state of $S = 45$ was synthesized but again with $U_{eff} \sim 0$ cm^{-1}.[26]

Apart from transition-metal based complexes, bimetallic to octametallic lanthanides complexes are also reported.[27] Polymetallic lanthanide complexes tend to have weak intramolecular exchange coupling due to the radial nature of the f-orbitals. Therefore, it is necessary to model lanthanide complexes featuring large magnetic anisotropy and strong magnetic exchange coupling. The strong intramolecular exchange coupling could be achieved by employing the radical as a bridging ligand between the two lanthanides. In light of this, $[N_2]^{3-}$ ligand with S=1/2 was employed by Long et al. to synthesize dilanthanide complexes based on Tb, Ho and Er with magnetic hysteresis upto 14 K and U_{eff} = 227 cm^{-1} for Tb complex.[28] Recently, Demir and group employed other radicals like 2,2′-bipyrimidine, bisbenzimidazole as bridging ligands to obtain large exchange coupling between the lanthanides.[29,30] Other polymetallic lan-

thanides complexes featuring high large spin-reversal barrier includes $[Ho_5O(O^iPr)_{13}]$, $[Dy_5O(O^iPr)_{13}]$ and $[Dy_4K_2O(O^tBu)_{12}]$, with U_{eff} of 278, 368 and 481 cm^{-1}, respectively.[31–33]

It can be manifested that increasing the spin in the system does not necessarily increase the spin-reversal barrier of the system and the synthetic efforts put to increase the spin of the system so as to enhance the U_{eff} have fallen short of expectations. Particularly, magnetic anisotropy is subtle towards the alignment of the individual Jahn-Teller axes and is reduced substantially when the anisotropic axes of the individual nuclei are misaligned in the multimetallic clusters.[34,35] Therefore, increasing S is not a good approach, and increasing $|D|$ will be a better choice to accomplish a large spin-reversal barrier.[36]

1.2.4 Mononuclear Single-Molecule Magnets

Mononuclear complexes based on lanthanides (Ln) have gained much popularity as propitious candidates for SMMs since the report of phthalocyanine Tb(III) complex, $TbPc_2$ in 2003 owing to huge magnetic anisotropy and large spin ground state by Ishikawa et al. It was reported to possess spin-reversal barrier of 230 cm^{-1}.[37] Followed by this, a plethora of Ln-based complexes have been synthesized and characterized with high anisotropic energy barriers.[38–40] They exhibit large unquenched angular momentum and strong spin-orbit coupling, which are solely responsible for their magnetic behaviors.[27,41–43] The recent progress in the field is marked by the synthesis of dysprosium metallocene complex which shows magnetic hysteresis upto 80 K, attaining blocking temperature beyond that of liquid nitrogen.[44] A theoretical model providing a correlation between angular dependence of f orbitals and electron distribution has been formulated by Long et al. to act as a guide for the design of single-molecule magnets based on f-elements.[45] In accordance with the model, it is reported that Ce^{III}, Pr^{III}, Nd^{III}, Tb^{III}, Dy^{III} and Ho^{III} ions possess an oblate shape of electron density while prolate electron density is possessed by Pm^{III}, Sm^{III}, Er^{III}, Tm^{III} and Yb^{III}. Gd^{III} and Lu^{III} with f^7 and f^{14} electrons respectively exhibit spherical electron density. Thus, in an effort to obtain large magnetic anisotropy in a complex, the complex should be designed in such a way that electrostatic repulsion between the metal and ligands should be minimal. This implies that for complexes with oblate electron density, the ligand field should be along z-axis and vice-versa for prolate electron density.

Transition metal (TM) complexes have also entered the spotlight in recent years, offering tantalizing alternatives to be utilized in prospective applications.[19,46–48] In this regard, in mononuclear complexes containing 3d-metal ions, it is essential to maintain the first-order orbital angular momentum to accomplish large magnetic anisotropy on a

level comparable with Ln based complexes.[49–52] Controlling various chemical modifications in the coordination environment, such as the coordination number, geometry of the complex and nature of ligand atoms directly bonded to the metal center, assists in the conservation of the first-order orbital angular momentum. In TM complexes with coordination number greater than 4, the ligand field quenches the orbital angular momentum as a result of Jahn Teller distortion.[53] However, the complexes with high axial symmetry, show signs of unquenched angular momentum and hence moderate magnetic anisotropy, but the molecules with high local symmetry are quite scarce.[54,55] The breaking of symmetry significantly lowers the magnitude of magnetic anisotropy as elegantly reported by Feng et al. where the Fe(III) complex i.e. $[(PMe_3)_2FeCl_3]$ with appropriate local symmetry results in D = -50 cm^{-1} which lowers to -17 cm^{-1} in $[(PMe_2Ph)_2FeCl_3]$ complex with the broken symmetry.[56] Yao et al. also reported the effect of symmetry breaking on the energy barrier where Co(II) complex possessing high local symmetry possess 10-fold higher U_{eff} value than the other complex with broken symmetry.[54] To overcome these ligand field effects, the low-coordinate complexes (coordination number <4) renewed the interest of researchers, since, they favor degenerate ground states resulting in minimal quenching of orbital angular momentum. To this end, linear or quasi-linear two-coordinate complexes emerge as the choicest complexes for mitigating these effects and eventually resulting in large anisotropic energy barriers.[57–60] The stability and isolation of these low coordinated complexes necessitate sterically encumbered ligands. A copious number of two- and three-coordinate complexes featuring Fe(II) center are already reported with intriguing magnetic properties.[19,46,61–63] Nearly, all these complexes anchorage sterically bulky ligands. A large spin-reversal barrier of 226 cm^{-1} is reported for a prominent example of two co-ordinate Fe(I) complex. The large barrier of 450 cm^{-1} is observed for a two-coordinated Co complex by Bunting et al. which is the highest among the 3d based SMM reported so far.[64]

1.3 Spin-Crossover Complexes

The phenomenon of spin-crossover (SCO) is one of the most apparent examples of molecular bistability in transition metal complexes. It is generally observed in paramagnetic centers having electronic configuration of $3d^4$ to $3d^7$.[65] The spin-state of such complexes can change from ground-spin state to energetically low lying excited spin states that could be brought by application of external stimuli such as magnetic field, redox reaction, temperature, pressure or photo irradiation.[66–69] Spin-crossover is observed in situation where the ligand field splitting is comparable to spin pairing energy. At the molecular scale, the driving force of the spin conversion is the entropy variation

due to the metal-ligand bond length changes.[70] The change in molecular spin states is accompanied by the change in magnetic as well as structural properties. Observation of spin-crossover phenomenon along with the slow magnetic relaxation at high blocking temperature is highly anticipated for potential use as molecular qubits and logic devices.[71,72] This will revolutionize the field of quantum devices for high-density data storage and fast processing of information. Mononuclear 3d transition metal complexes hold promise in this direction with both evident properties of magnetism and spin-crossover at the molecular level.[73,74] Understanding ligand field-derived modulation of anisotropy in conjunction with SCO property can help in designing molecules with both properties.

1.4 Organic Molecular Magnets

These are the molecular magnets based upon purely organic materials i.e., the unpaired electron spin resides in the p-orbitals. They are prepared from abundant raw materials i.e. C, O, N, S, etc. Recent decades have seen an increase in research on purely organic magnetic materials. Organic Molecular Magnets (OMMs) have the advantage over conventional inorganic magnets as they are highly soluble in organic solvents, require no energy-intensive metallurgical preparation, and their magnetic properties are highly tunable. Ferromagnetic ordering for an organic-based magnet was first realized for $Fe(C_5Me_5)_2]^+[TCNE]^{\cdot-}$ (TCNE = tetracyanoethylene) below its T_c of 4.8 K.[75]

1.4.1 Organic Radicals

The building blocks for the OMMs are the organic radicals that contain unpaired electrons. In general, organic radicals are very reactive and unstable due to the presence of unpaired electrons in their highest occupied molecular orbitals and thus, they can easily couple to dimers or undergo recombination, hydrogen abstraction, disproportionation, etc. to fulfill their valency.[76] The stability of the radical can be enhanced by increasing the delocalization of the unpaired electron over the large part of the molecule. By doing so, they are less likely to be able to donate an electron, and their stability increases. An alternative way to obtain persistent radicals is to screen the radical center with the bulky substituents so as to prevent it from further reactions.[77]

The synthesis of the first persistent triphenylmethyl radical by Gomberg et al. came up as a landmark finding providing inspiration for the synthesis of robust radicals.[78] The stability of the radical is due to the protection of the radical center by the three phenyl rings. However, increasing the strain by polychlorination to obtain polychlorinated triphenylmethyl (PTM) radical makes it chemically inert by providing essential

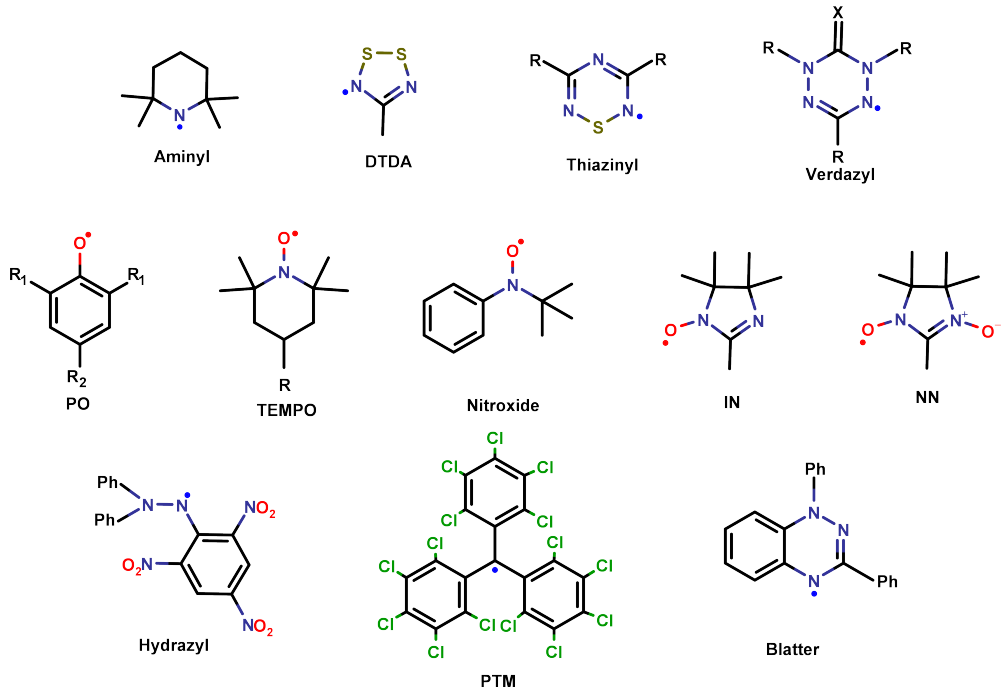

Figure 1.2: Molecular structures of some stable known organic monoradicals.

shielding by the additional chlorine atoms.[79] TEMPO (2,2,6,6,-tetramethylpiperidin-N-oxyl) is a highly stable radical due to the four methyl groups providing steric protection to the radical center.[80] Another venerable class of radicals is the phenoxyls (PO) radicals, where the *o* and *p* substitutions provide large stability.[81] Many stable radicals are based on the N and O as spin carriers which include but are not limited to aminyl, hydrazyl, verdazyl, nitroxides, imino nitroxides (IN), nitronyl nitroxides (NN), etc. The first purely organic ferromagnet was synthesized by Kinoshita and co-workers based on nitronyl nitroxide radical.[82] The other class of radicals that have gained attention contains the heavy element S as the spin source, which includes dithiadiazolyl (DTDA), thiazinyl, etc.[77] One of the super stable radical is the benzotriazinyl (Blatter's) radical which was synthesized in 1968.[83] However, the radical has gained considerable attention recently after easy synthetic strategies developed by Koutentis et al.[84,85] Stable organic radicals appear as superior examples of molecular building blocks on the way to obtaining multifunctional molecular materials.

On the basis of the number of unpaired electrons in a molecule, the radicals are classified into monoradical, diradical, triradical, and polyradicals. As the name suggests, the monoradical contains one unpaired electron (S=1/2) with spin multiplicity as a doublet. All the prospective examples discussed above belong to monoradicals.

1.4.1.1 Diradicals

When the molecule contains two unpaired electrons in degenerate molecular orbitals, then it is known as diradical. They can be classified into Kekulé and non-Kekulé molecules.[86] In Kekulé structures, there exists a "resonance hybrid" between the open shell and closed-shell configurations.[87] In the open shell diradical configuration, the aromatic six-membered rings are formed, which can vanquish the energy for the breaking of a carbon-carbon π-bond. However, in non-Kekulé structures, some electrons are unpaired due to the topology of the π-electron arrangement.[88] Due to the existence of two unpaired electrons, the diradicals can be in the triplet or singlet state depending on the orientation of electrons i.e., parallel or antiparallel respectively. The ground state of a diradical is determined by the relative energies of the two spin states. Further, the singlet-triplet energy gap can be calculated from the electron exchange interaction ($2J$), with $\Delta E_{ST} = E_S - E_T = 2J$. The sign of $2J$ will provide the ground state of the molecule with positive (negative) $2J$ indicating triplet (singlet) as the ground state. For an in-depth understanding of the nature of the exchange interactions in these molecules, the prerequisite is to understand the nature of the coupler between the two spin centers. It has been postulated that the shorter coupler provides large magnetic exchange interactions and vice versa for the larger coupler. Moreover, the dihedral angle should be low so as to have efficient spin propagation between the two radical moieties. It has been demonstrated by Shil et al. that, in crowded diradicals with large dihedral angles, the itinerant exchange between two magnetic sites through π network is forbidden due to non-planarity.[89] In such diradicals, the radical sites being closer in space participate in the direct exchange, which usually favors the ferromagnetic coupling following Hund's rule.[90] A conventional example of coupler that manifests ferromagnetic interactions is the m-phenylene coupler which is suitable for both carbon-centered as well as nitrogen-centered radicals such as nitroxyl and nitronyl nitroxide (NN) radicals.[91,92] Although in some cases, it is observed as an antiferromagnetic coupler. In that case, it depends on the conformation of the spin sources with respect to the coupler.[93,94] It has been observed that when the dihedral angle between the spin sources and coupler is large enough, it forbids the conjugation between the radical and coupler. Hence, the well-known nature of the ferromagnetic coupling of the coupler is overturned. Apart from the coupler, the magnetic properties can be tuned by other modifications in the system. The introduction of EDG and EWG on the molecule can modulate the magnetic exchange interactions.[95] A recent study by Burnea et al. demonstrated the significance of non-covalent interactions, specifically hydrogen bonding, in enhancing magnetic coupling in a diradical.[96]

Several synthetic efforts have been put forward to obtain robust and highly stable diradicals. Nitroxide radicals are at the forefront as stable spin-carriers in the design of

diradicals based on it, being highly stable at ambient temperature.[97,98] Numerous diradicals based on stable known radicals, like nitronyl nitroxide, imino nitroxide, verdazyl, oxoverdazyl etc., have been synthesized extensively.[99–103] Utilizing Blatter radical as a spin source, Rajca et al. synthesized the stable diradicals by coupling the Blatter's radical with nitronyl nitroxide and imino nitroxide and di-Blatter diradical with superior magnetic properties.[104–106] The exceptional air and moisture stability and thermally robust properties of Blatter's radical also led Wudl and group to synthesize stable benzotriazinyl diradicals.[107,108] Thereafter, Zheng et al. proposed the synthesis of Blatter's diradicals by coupling the two monomers of Blatter's radical.[109,110]

1.4.1.2 Diradicaloids

The diradicaloids are the molecules in which the two molecular orbitals containing unpaired electrons are nearly degenerate. These are identified by two weakly interacting electrons with similar energy. After the pioneering reports of carbon-centered diradicaloids, namely Thiele's hydrocarbons in 1904[111] and Tschitschibabin's hydrocarbon in 1907,[112] the research on this class of compounds has been unrolled widely. A series of diradicaloids which includes bisphenalyenyls,[113,114] quinodimethanes,[115] diiendenoacenes,[116] indenofluorenes,[117] zenthrenes,[118] and anthenes[119] etc. have been synthesized. Diradicaloids exhibit unique electronic, optical, and magnetic properties that promise to be extremely useful in organic electronics and spintronics.[107,120]

1.4.2 Magnetic Exchange Interactions

In organic molecules, the magnetism arises from the interaction of the unpaired electrons with each other and the long range spin-spin alignment. The underlying parameter to characterize the interactions between the electrons is the magnetic exchange coupling ($2J$) between the spin-centers. When the two spin-centers possess electrons with parallel orientation with respect to each other, it results into ferromagnetic coupling with $2J > 0$. Contrary to this, the antiferromagnetic coupling arises when the two interacted spins are anti-parallel to each other and $2J < 0$. Additionally, the temperature plays a crucial role in the magnetism of organic molecules. For most of OMMs, the spins tend to remain in the parallel orientation in the same direction below a certain temperature called critical temperature (T_C) and thus, possess bulk ferromagnetic properties. However, when the temperature exceeds T_C, the thermal energy becomes larger in comparison to the electronic exchange interactions leading to random orientation of the neighbouring spins. In this case, the radicals show paramagnetic properties.

1.5 Perspective of the Thesis

An increasing drive towards the miniaturization of electronic devices has brought a rush along the road to molecular magnetism. Molecule-scale magnets are required to exhibit enhanced magnetic properties such as magnetic anisotropy, magnetic exchange interactions, etc. at room temperature for their practical applications. These magnetic molecules can be obtained by exploring the synthetic routes to these molecules. However, computational chemistry employing first-principle calculations could provide a blueprint that allows the investigation of their magnetic properties beforehand and presents an essential source of rationalization for the observed properties. Further, it allows to tune their magnetic properties by studying magneto-structural correlations. From a computational perspective, designing new generation molecular magnets requires a thorough understanding of the multispin Hamiltonian parameters, that is, magnetic anisotropy, and exchange interactions to further model magnetic molecules with superior magnetic properties. These magnetic properties mainly originate from the unpaired spin of the open-shell systems which presents complexity to understand their electronic structure and requires sophisticated methods that can include electron correlations explicitly. Therefore, the computation of these parameters requires reliable methods beyond traditional DFT based methods to reproduce the experimental observations. The wavefunction based methods make it possible to include static and dynamical correlations and provide a proper description of multideterminantal nature of the wavefunction and thus, are a method of choice to compute the magnetic parameters. Applying these *ab initio* wavefunction based methods, this thesis focus on gaining an in-depth understanding of the electronic structure, magnetic properties and further establishing magneto-structural correlations to eventually provide a predictive tool for designing new magnetic materials. In this context, we intend to understand the role of the ligands at axial and equatorial ligands in modulating the magnetic anisotropy in transition-metal based mononuclear single-molecule magnets. Further, exploiting the knowledge acquired from the role of ligands, the complexes are chosen with the aim to enhance the magnetic anisotropy. In the latter part of the thesis, we investigated the isotropic magnetic exchange interactions of various designed diradicals based on Blatter's radical and studied multiple pairwise exchange interactions arising due to the micromagnetic centers created by the delocalization of the spin-density equally on the three nitrogen atoms of the triazinyl ring. Further, a unique strategy to fine-tune the ground state of the diradicals is provided to obtain ferromagnetically coupled diradicals.

To accomplish these objectives, the entire work is presented in four chapters *(Chapters 3-6)* where the first two chapters focus on the investigation of magnetic anisotropy

of organometallic single-molecule magnets. The latter two chapters deal with the understanding of isotropic ferromagnetic exchange interactions in metal-free organic molecular magnets. The thesis is outlined as follows:

- In single-molecule magnets, the transition metal complexes with axial symmetry are the sought-after candidates to possess large magnetic anisotropy. In this context, we chose to study complexes with axial symmetry in the presence and absence of equatorial ligands. Firstly, Fe(III) trigonal bipyramidal complexes are studied to investigate the effect of axial and equatorial ligands on the ground state and the magnetic anisotropy of the complexes. Moreover, the transition metal complexes also show spin-crossover properties brought out by some external stimuli like temperature, pressure, light, etc. Therefore, the complexes are investigated for spin-crossover properties (*Chapter 3*). Further, the complexes with only axial ligands are chosen to study the effect of coordination number on magnetic anisotropy. The origin of magnetic anisotropy is studied with the help of magnetic relaxation pathways and the pattern of d-orbital splitting in different complexes (*Chapter 4*).

- Organic diradicals with high-spin ground state and large ferromagnetic exchange interactions are potential contenders for metal-free organic molecular magnets. We aim to model several diradicals based on the highly stable Blatter's radical with the goal to obtain ferromagnetically coupled diradicals and understanding the origin of magnetic coupling (*Chapter 5*). Furthermore, we also provided a unique strategy to fine tune the inherent zwitterionic ground-state of the tetraphenylhexaazaanthracene (TPHA), the molecule containing two Blatter's radical moieties to antiferro- and ferromagnetically coupled diradicals by increasing the length of the coupler and *push-pull* substitution (*Chapter 6*).

CHAPTER 2

Theoretical Background and Computational Methods

In this chapter, the computational tools used for studying organic molecular magnets and single-molecule magnets are briefly described. In the beginning, a brief overview of the Hartree-Fock method followed by the MC-SCF methods are discussed with special emphasis on CASSCF and NEVPT2. Further, the description of density functional theory and the various functionals are briefly explained. Further, the phenomenological Hamiltonian used to describe the magnetic exchange interactions in localized spin centers is discussed. In the subsequent section, different methods within DFT and WFT based methods to compute magnetic exchange interactions are quickly explained. Furthermore, the spin-orbit coupling introduced as a perturbation is presented. Thereafter, the Hamiltonian for zero-field splitting is discussed.

2.1 The Many-body Problem

The electronic structure of a molecular system can be obtained by finding an approximate solution to the non-relativistic time-independent Schrödinger equation,

$$\hat{H}\Psi(r_1, r_2, ..., R_1, R_2, ...) = E\Psi(r_1, r_2, ..., R_1, R_2, ...) \tag{2.1}$$

where $\Psi(r_1, r_2, ..., R_1, R_2, ...)$ is a wave function corresponding to the position of electrons (r_i) and nuclei (R_I). $\hat{H}$ is the Hamiltonian operator which consists of kinetic energy and potential energy operators, neglecting relativistic effects, and takes the form:

$$\begin{aligned}\hat{H} &= \hat{T} + \hat{V} \\ &= \hat{T}_e + \hat{T}_n + \hat{V}_{ee} + \hat{V}_{ne} + \hat{V}_{nn} \\ &= -\frac{1}{2}\sum_i \nabla_i^2 - \frac{1}{2}\sum_I \frac{\nabla_I^2}{M_I} + \sum_{i\neq j}\frac{1}{r_{ij}} - \sum_{i,I}\frac{Z_I}{R_{iI}} + \sum_{I\neq J}\frac{Z_I Z_j}{R_{IJ}}\end{aligned} \tag{2.2}$$

where i and j are the indices of electrons and I and J of nuclei. The mass of nuclei is denoted by M_I. Z_I is the atomic number of the I^{th} atom. The first two terms in Eq. 2.2 represent the kinetic energies of the electron and nuclei. The remaining terms involve the potential energy arising from the Coulomb interactions i.e., electron-electron repulsion, the attraction between electron and nucleus, and inter-nuclear repulsion respectively. The analytic solutions of the Eq. 2.2 could be obtained for simple systems (typically one electron systems), for example, for the hydrogen atom and molecule. Thus, for broader applicability in many-electron systems, it becomes necessary to apply approximations. The first and foremost approximation uses the significant difference between the mass of electron and nuclei and considers the nuclei to be static and only the motion of the electron is considered. Thus, the nuclei are taken as frozen related to electrons. This is the basis of Born-Oppenheimer Approximation (BOA). Within this framework, the total wave function in Eq. 2.1 can be factorized into the wave function of electrons and ions as

$$\psi = \psi_e(r_1, r_2, ...)\psi_N(R_1, R_2, ...) \tag{2.3}$$

Under the Born-Oppenheimer Approximation, the kinetic energy of the nuclei (second term in Eq. 2.2) and the inter-nuclear repulsion (last term in Eq. 2.2) can be taken as constant and thus, the Hamiltonian becomes explicitly electronic Hamiltonian given by

$$\hat{H}_e = -\frac{1}{2}\sum_i \nabla_i^2 + \sum_{i\neq j}\frac{1}{r_{ij}} - \sum_{i,I}\frac{Z_I}{R_{iI}} \tag{2.4}$$

This approximation simplified the solution of the many-body Schrödinger equation however, the problem still persists in solving it for many-electron systems. Therefore, other alternatives to solve the many-body problem are required.

2.2 The Hartree-Fock Method

One of the methods of approximation for determining the wave function and energy of the many-body system in a static state is the Hartree-Fock method. This method involves averaging the electron-electron repulsion term in Eq. 2.4 and thus, calculating

the effective repulsion experienced by an electron due to the average field of all the electrons, instead of calculating the repulsion for all the different electron pairs. This method assumes that the N-body wave function is composed of the product of one electron wave function, in which each electron moves in an average potential created by the nucleus and all other electrons. The wave function of the molecule can thus be written by a single Slater determinant as,

$$\Psi^{e}_{HF}(x_1, x_2, ...x_N) = \frac{1}{\sqrt{N!}} \begin{vmatrix} \chi_1(x_1) & \chi_2(x_1) & \cdots & \chi_N(x_1) \\ \chi_1(x_2) & \chi_2(x_2) & \cdots & \chi_N(x_2) \\ \vdots & \vdots & & \vdots \\ \chi_1(x_N) & \chi_2(x_N) & \cdots & \chi_N(x_N) \end{vmatrix} \tag{2.5}$$

where x_1, x_2, ..., x_N are collectively denoted by the three spatial coordinates r_1, r_2, ..., r_N and one spin coordinate ω_1, ω_2, ..., ω_N of N-electron system and $\chi_i(x_i)$ denotes one-electron wave functions which are a linear combination of atomic orbital wave functions. One can obtain the minimum energy wave function by applying the variational principle. This leads to the energy eigenvalue equation as,

$$f(x_i)\chi(x_i) = \epsilon_i\chi(x_i) \tag{2.6}$$

where ϵ_i is the energy eigenvalue of atomic orbitals. $f(x_i)$ is the Fock operator. Thus, the Hamiltonian can be written as,

$$\hat{H}_e = -\frac{1}{2}\nabla_i^2 - \sum_I \frac{Z_I}{R_{iI}} + V^{HF}(r_i) \tag{2.7}$$

where V^{HF} is the average potential experienced by the i^{th} electron due to other electrons. By using the fock operator, the multi-electron Schrödinger equation can be broken down into a set of one-electron equations. However, the V^{HF} (Hartree-Fock potential) depends on the total wave function making it a non-linear problem. This need to be solved iteratively by self-consistent field procedure. Although Hartree-Fock's method is capable of reproducing 99% of the total exact energy within a sufficiently large basis set limit, the remaining 1% is vital for the entire chemistry. This remaining energy accounts for the electron correlation energy (E_{corr}) which is completely neglected in the HF method. The electron correlation energy is defined as the difference between the exact nonrelativistic energy of the system (ε_o) and the HF energy obtained in the limit of complete basis (E_o) given by

$$E_{corr} = \varepsilon_o - E_o \tag{2.8}$$

Thus, different approaches are available to account for the electron correlation.

2.3 Multiconfigurational Self Consistent Field (MC-SCF) methods

MCSCF method is a useful method for the description of the electronic structure of molecular systems with strongly correlated electrons for which the single configuration wave function becomes inadequate. In MCSCF theory, the wave function is written as a linear combination of all possible configurations i.e., CSFs. Thus, in MCSCF, static correlations can be improved by expressing the wave function in terms of more than one determinant.

$$\psi_{MCSCF} = \sum_i c_i \phi_i \tag{2.9}$$

where c_i is the expansion coefficient and ϕ_i is the Slater determinant.

2.3.1 CASSCF and NEVPT2

CASSCF method is one of the *ab intio* multi-reference methods where the wave function is generated by the linear combination of all the CSFs which arises from a particular number of electrons present in a specific number of orbitals. The method is based on the efficient partitioning of molecular orbitals generated from the Hartree-Fock orbitals into three sets of orbitals i.e., inactive orbitals, active orbitals, and virtual orbitals. The inactive orbitals are always doubly occupied and the virtual ones are always empty. The remaining electrons present in the active space span the explicitly correlated orbitals. The active orbitals can have an occupancy between 0 to 2, depending on the nature of the molecular system. The active space is designated as (*n,N*) where *n* is the number of electrons in *N* number of orbitals. Within this active space, a full CI is performed to construct the CASSCF wave functions. The active space is chosen manually keeping in mind the chemical aspects of the problem to be studied. For example, for 3d transition metal complexes, it is important to include the *d* orbitals in the active space. And sometimes, a double *d*-shell is taken into account by adding an additional set of five *d* orbitals. Similarly, for 4f complexes, the active space is composed of the seven *f*-orbitals of the metal. However, complexes of 4d, 5d and 5f are not so simple as their metal center features radially extensive magnetic orbitals with significant ligand interactions. Moreover, in some complexes with weakly covalent metal-ligand bonding, the minimal active space is not enough to account for the electron correlation and

one needs to expand the active space by incorporating the ligand orbitals into the active space. Based on the choice of active space, a number of configuration state functions (CSFs) are generated. The increase of active space subsequently increases the number of CSFs in CI space. CASSCF calculation takes into account a certain number of CSFs where the weightage of each CSF is optimized together with the orbitals. In a CASSCF calculation, the solution can be obtained either for a single state or for the average of a number of states. Accordingly, the calculation is called state-specific (SS-CASSCF) or state-average (SA-CASSCF) respectively. The selection of the number of states (roots) should be done manually and carefully, taking into consideration, a less number of roots that are low-lying and thus take part actively in the mixing of states.

Although the CASSCF wave function identifies static correlation nicely well, only a small number of electrons in the active orbitals are correlated. While the correlation including inactive electrons, i.e., dynamical correlation, is overlooked. With a good approximation to the zeroth order wavefunction, the perturbation theory could be employed to account for the effects of dynamic correlations where the effect of full CI can be approximated. The N-electron valence state perturbation theory (NEVPT2) is a perturbative method that adds the dynamical correlations to the CASSCF wave function by using multiconfigurational second-order perturbation theory and generally takes into account a large number of single and double electronic transitions on the wave function generated by CASSCF in order to approximate the full CI energies.

2.4 Density Functional Theory (DFT)

The dependence of the Hamiltonian on the total number of electrons comes up with an idea of utilizing a physical observable i.e., electron density ρ, as its integration over the entire space results in the total number of electrons N, i.e.,

$$N = \int \rho(r) dr \tag{2.10}$$

Thus, the number of degrees of freedom is reduced to three as the electron density is a function of three variables, irrespective of the size of the system. This makes Density Functional Theory (DFT) the most popular and useful computational tool to study many-electron systems. The concept of density functional was proposed in the work of Fermi and Thomas in the 1920s for the first time.[121] The modern DFT relies on Hohenberg, Kohn, and Sham, which state that the sum of the exchange and correlation energies of a uniform electron gas could be determined by using its electron density.[122,123] In the Kohn-Sham formalism, the total ground state electronic energy (E) is summed over three energies, viz. the kinetic energy of a uniform electron gas (T), electron-

electron repulsion energy (V_{ee}), and electron-nuclear attraction energy (V_{Ne}). It was further extended by Dirac who introduced the exchange-correlation energies between the electrons.[124] Therefore, the total ground state energy of the system is written as,

$$E_o = E[\rho(r)] = T[\rho(r)] + V_{Ne}[\rho(r)] + V_{ee}[\rho(r)] + E_{XC}[\rho(r)] \tag{2.11}$$

Within the Kohn-Sham formalism, the energy of the ground state of a system with n electrons and N nuclei is written as,

$$\begin{aligned} E[\rho] = -\frac{1}{2}\sum_{i=1}^{n}\int \psi_i^*(r_1)\nabla_i^2\psi_i(r_1)dr_1 - \sum_{\chi=1}^{N}\int \frac{Z_\chi}{r_{\chi i}}\rho(r_1)dr_1 \\ +\frac{1}{2}\int\int \frac{\rho(r_1)\rho(r_2)}{r_{12}}dr_1dr_2 + E_{XC}[\rho] \end{aligned} \tag{2.12}$$

where ψ_i's are the Kohn-Sham (KS) orbitals. The first term represents the kinetic energy of the non-interacting electrons, the second term denotes electron-nuclear repulsion, and the last two terms account for Coulombic repulsion between electrons and exchange-correlation term respectively. The ground-state electron density ρ(r) at a point r in terms of KS orbitals is represented as

$$\rho(r) = \sum_{i=1}^{n} |\psi_i(r)|^2 \tag{2.13}$$

Therefore, the ground state energy (E_o) can be obtained from the electron-density (ρ) using Eq. 2.12 and 2.13 if the KS orbitals and E_{XC} is known. The KS orbitals can be found by solving the KS equation employing the variational theorem,

$$\hat{h}_i\psi_i(r_i) = \varepsilon_i\psi_i(r_i) \tag{2.14}$$

Here, $\hat{h}_i$ is the KS Hamiltonian and ε_i is the respective orbital energy. The KS Hamiltonian is written as

$$\hat{h}_i = -\frac{1}{2}\nabla_i^2 - \sum_{\chi=1}^{N}\int \frac{Z_\chi}{r_{\chi i}} + \int \frac{\rho(r_2)}{r_{12}}dr_2 + V_{XC}(r_1) \tag{2.15}$$

where V_{XC} is the functional derivative of the exchange-correlation energy given by

$$V_{XC}(r) = \frac{\delta E_{XC}[\rho(r)]}{\delta\rho(r)} \tag{2.16}$$

Thus, V_{XC} can be determined from the E_{XC} term. In KS DFT, beginning from the tenta-

tive charge density ρ, the dependence of E_{XC} is used to calculate V_{XC}. After obtaining the initial set of KS orbitals, these orbitals are further used to obtain the superior electron density from Eq. 2.13. This process is repeated over and again until there is no further deviation in density and KS orbitals. Lastly, the ground-state electronic energy is calculated employing Eq. 2.12.

The exchange-correlation energy (E_{XC}) is defined as the sum of the exchange term (E_X), the interactions between the electrons of the same spin, and the correlation term (E_C), the interactions between the opposite spin electrons given as

$$E_{XC} = E_X + E_C \tag{2.17}$$

2.4.1 Local Density Approximation (LDA)

The calculations of total energy require approximations for the exchange-correlation energy. One of the approximations is the local density approximations (LDA). Based on the LDA, it is assumed that the exchange-correlation energy density is constant at every position in space for the molecule as it would be for the homogenous electron gas having the same density as found at that position.

$$E_{XC}^{LDA}[\rho] = \int \rho(r)\varepsilon_{XC}(\rho(r))dr \tag{2.18}$$

where ε_{XC} refers to the exchange-correlation energy per particle of a homogeneous electron gas with charge density ρ. For the extension to spin-polarized systems, the exchange term can be easily obtained, however, for the correlation term, there is a need for further approximation as it involves two spin-densities (ρ_α and ρ_β) with total spin (ρ) equals to the sum of the density of α and β spins i.e., $\rho = \rho_\alpha + \rho_\beta$. Thus, E_{XC} takes the form,

$$E_{XC}^{LSDA}[\rho_\alpha, \rho_\beta] = \int \rho(r)\varepsilon_{XC}(\rho_\alpha(r), \rho_\beta(r))dr \tag{2.19}$$

2.4.2 Generalized Gradient Approximation (GGA)

Since LDA assumes that the electron density is constant in the complete space, it overestimates the correlation energy and underestimates the exchange energy.[125] For a real system with non-local density variations, the exchange-correlation energy differs significantly from that of uniform electron distribution. Thus, a possible extension in the LDA formalism is the inclusion of the gradient of the charge density also. This approximation is called the generalized gradient approximation (GGA). Within the GGA formalism, E_{XC} takes the form,

$$E_{XC}^{GGA}[\rho_\alpha, \rho_\beta] = \int \rho(r)\varepsilon_{XC}(\rho_\alpha(r), \rho_\beta(r), \nabla\rho_\alpha(r), \nabla\rho_\beta(r))dr \tag{2.20}$$

2.4.3 Hybrid functionals

The exchange term E_X is not well described in both LDA and GGA approximations. Thus, hybrid functionals are proposed for better performance of DFT. The fraction of Hartree-Fock exchange energy is included in the exchange functional, thus, taking the form

$$E_{XC}^{hybrid} = aE_X^{HF} + (1-a)E_X^{DFT} + E_C^{DFT} \tag{2.21}$$

Here, a determines the amount of non-local exchange in the hybrid approximation. E_X^{HF} is the exact HF exchange energy. In this thesis, the hybrid functional B3LYP is used which contains 20% exact exchange admixture.

2.5 Computation of Magnetic Exchange Interactions

A simplified approach to estimating the magnitude of magnetic exchange interactions in a wide range of systems including organic diradicals, dinuclear complexes, etc. is based on the Heisenberg-Dirac-van Vleck Hamiltonian. The magnetic exchange interactions ($2J$) between the two magnetic sites A and B appear in the phenomenological Hamiltonian as

$$\hat{H}_{HDvV} = -2J\hat{S}_A\hat{S}_B \tag{2.22}$$

where $\hat{S}_A$ and $\hat{S}_B$ are the fictitious local spin operators for the interacting sites A and B, respectively, and $2J$ is the exchange coupling parameter. This Hamiltonian leads to a ladder of spin states from $S_{max} = S_A + S_B$ down to $S_{min} = |S_A - S_B|$ with S_A and S_B being the spin quantum numbers. With a positive $2J$, the high-spin triplet state is lower in energy, with ferromagnetic coupling between the two spin carrier sites. A negative $2J$ represents the low-spin singlet as a ground state with antiferromagnetic interactions. For a diradical with two unpaired electrons ($S_A = S_B = 1/2$) on each magnetic site, $2J$ can be represented as the energy difference between the singlet ($E_{S=0}$) and triplet ($E_{S=1}$) spin states i.e.,

$$2J = E_{S=0} - E_{S=1} \tag{2.23}$$

The electronic configuration with both the spins up corresponds to the triplet state (S=1). On the contrary, the configuration with one up spin and one down spin electrons

corresponds to the singlet state (S=0). But for S=0 state, there is a possibility of more than one electronic configuration, i.e., both the electrons at site A, both the electrons at site B, configuration with spin up electron at site A and spin down electron at site B and vice versa. Thus, $E_{S=1}$ provides the correct energy of the triplet state, however, the multideterminantal nature of the singlet state makes it challenging to compute its correct energy, $E_{S=0}$. It becomes difficult to obtain a pure singlet state from UDFT or UHF approach and multiconfigurational methods such as CAS-CI, MCSCF, etc. are required to accurately represent low-spin states. As an alternative approach, the broken-symmetry approach can be employed within the DFT framework.

2.5.1 Broken-Symmetry DFT

The broken-symmetry formalism was proposed by Noodleman in 1981, to compute the magnetic exchange interactions in dinuclear complexes.[126] According to Noodleman, when the two singly occupied molecular orbitals called magnetic orbitals of the two spin bearing sites are allowed to interact by overlapping in the SCF procedure, a state of mixed spin symmetry and lowered space symmetry is obtained. This is called the mixed spin or broken symmetry (BS) state. Any mixed spin states can be approximated by the weighted average of the other spin states. As per the description of BS state by Ruiz et al.,[127] for a system with two unpaired electrons in two nonorthogonal orbitals a and b localized on two different atoms, the $M_S = 1$ component of the high-spin state in terms of Slater determinant is given as

$$\Phi(S = 1, M_S = 1) = \frac{|ab|}{\sqrt{(2 - 2\langle a|b\rangle^2)}} \tag{2.24}$$

The energy of the high-spin state can be determined easily. The BS wave functions describe the low-spin singlet state and the two solutions are possible given by

$$\sigma^{I}_{BS} = \frac{|a\bar{b}|}{\sqrt{2}} \tag{2.25}$$

$$\sigma^{II}_{BS} = \frac{|\bar{a}b|}{\sqrt{2}} \tag{2.26}$$

The bar over the orbital signifies the occupancy of the orbital with the spin-down electron. A linear combination of these two BS determinants results in the adequate singlet function provided by[128]

$$\Phi(S = 0) = \frac{\sigma^{I}_{BS} - \sigma^{II}_{BS}}{\sqrt{2 - 2\langle \sigma^{I}_{BS} | \sigma^{II}_{BS} \rangle}} \tag{2.27}$$

For $M_S = 0$ component of the triplet state also, a wave function can be constructed from the two BS solutions as[128]

$$\Phi(S = 1, M_S = 0) = \frac{\sigma^I_{BS} + \sigma^{II}_{BS}}{\sqrt{2 + 2\langle\sigma^I_{BS}|\sigma^{II}_{BS}\rangle}} \tag{2.28}$$

Calculating the energy for the wave function in Eq. 2.27 and subtracting from the energy of the triplet yields the singlet-triplet gap as:

$$2J = \frac{2(E_{BS} - E_T)}{1 - \langle\sigma^I_{BS}|\sigma^{II}_{BS}\rangle} \tag{2.29}$$

where $\langle\sigma^I_{BS}|\sigma^{II}_{BS}\rangle$ is the overlap integral between the two BS solutions. Neglecting the spin polarization of the inner shells, the integral can be approximately calculated from the overlap integral between the two SOMOs a and b as proposed by Caballol et al.[128] Thus, $2J$ can be re-written as

$$2J = \frac{2(E_{BS} - E_T)}{1 + S^2_{ab}} \tag{2.30}$$

For a sufficiently small overlap between the two orbitals, Eq. 2.30 reduces to

$$2J = \frac{2(E_{BS} - E_T)}{S^2_{max}} \tag{2.31}$$

proposed by Geinsberg, Noodleman and Davidson.[129–131]

For the systems with sufficiently large overlap integral, the Eq. becomes

$$2J = \frac{2(E_{BS} - E_T)}{S_{max}(S_{max} + 1)} \tag{2.32}$$

which was proposed by Bencini and Ruiz et al.[132] and further modified by Illas et al.[133] The modified version of Eq. 2.31 was later proposed by Yamaguchi et al.[134] given by

$$2J = \frac{2(E_{BS} - E_T)}{< S^2 >_{HS} - < S^2 >_{BS}} \tag{2.33}$$

Eq. 2.33 reduces to equations 2.31 and 2.32 in the weak and strong overlap limits respectively.

2.5.2 Spin-decontaminated procedure in BS-DFT

The Yamaguchi formalism leads to overestimated values when the spin polarization of the core becomes important. Therefore, it is required to extract the three main contributions to the magnetic exchange coupling i.e., a) direct exchange contribution, between

the two unpaired electrons, b) kinetic exchange contribution, corresponding to relaxation of magnetic orbitals in singlet state and c) spin polarization contribution, originating from different polarization of the electrons in the core orbitals in triplet and in singlet as proposed by Malrieu and co-workers.[135,136] The resultant of the three contributions provide the accurate magnitude of magnetic exchange coupling free from spin-contamination given by

$$J_{Tot} = J_o + \Delta J_{KE} + \Delta J_{CP} + \Delta J_{Other} \tag{2.34}$$

where J_o, ΔJ_{KE} and ΔJ_{CP} are the contributions from direct exchange, kinetic exchange and spin polarization of the core.

$$J_o = -\frac{E_{HS,RO} - E_{BS,RO}}{\langle S^2\rangle_{HS,RO} - \langle S^2\rangle_{BS,RO}} \tag{2.35}$$

$$\Delta J_{KE} = -\frac{E_{HS,RO} - E_{BS,UFC}}{\langle S^2\rangle_{HS,RO} - \langle S^2\rangle_{BS,UFC}} - J_o \tag{2.36}$$

$$\Delta J_{CP} = \frac{2(E_{BS,UFM} - E_{HS,UFM})}{2 - (\langle S^2\rangle_{BS,UFC} + \langle S^2\rangle_{BS,UFM})/2 + \langle S^2\rangle_{BS,UFC}(\langle S^2\rangle_{BS,UFM} - \langle S^2\rangle_{BS,UFC})/2} - J_o - \Delta J_{KE} \tag{2.37}$$

$E_{HS,RO}$ is the energy obtained from the calculation performed in the HS state in Restricted Open-shell formalism. The spin-flip of one of the magnetic orbitals results in the energy of BS state in Restricted Open-shell formalism i.e. $E_{BS,RO}$. The relaxation of magnetic orbitals in the frozen core orbitals leads to $E_{BS,UFC}$ (UFC stands for Unrestricted with Frozen Core orbitals). The relaxation of core orbitals in (HS,RO) and (BS,RO) leads to $E_{HS,UFM}$ and $E_{BS,UFM}$ (UFM stands for Unrestricted with Frozen Magnetic orbitals).

2.5.3 CASSCF/NEVPT2

The *ab initio* CASSCF/NEVPT2 method is also employed to compute the magnetic exchange interactions between the two radical centers. The initial guess orbitals for the CASSCF calculations can be taken from the unrestricted natural orbitals (UNOs) from DFT. Here, we have obtained these UNOs using the hybrid B3LYP functional. The CASSCF wavefunction is thus used as a reference wavefunction for subsequent NEVPT2 calculations to include dynamical correlations. The energies obtained from state-specific CASSCF/NEVPT2 calculations in the respective singlet and triplet states are then employed to compute the magnetic exchange interactions using Eq. 2.23.

2.6 Spin-Orbit Coupling

The term spin-orbit coupling (SOC) represents the coupling of the spin of the electron with its orbital angular momentum. SOC is the dominant spin-dependent relativistic correction to the Born-Oppenheimer Hamiltonian. The widely used one- and two-electron SOC operator is the Breit-Pauli form. The Breit-Pauli SOC operator is expressed as,

$$\hat{H}_{SOC} = \hat{H}^{(1)}_{SOC} + \hat{H}^{(2)}_{SOC} \tag{2.38}$$

Here, the first term is the one electron term describing the effect of potential of nuclei and the second term, the two electron term, describes the coupling caused by the motion of the electrons. The one- and two-electron SOC contributions are given by

$$\begin{aligned} \hat{H}^{(1)}_{SOC} &= \sum_i \hat{\mathbf{h}}_i^{\mathbf{1el-SOC}} \hat{\mathbf{s}}_i \\ &= \frac{\alpha^2}{2} \sum_i \sum_A Z_A r_{iA}^{-3} \hat{\mathbf{l}}_{iA} \hat{\mathbf{s}}_i \end{aligned} \tag{2.39}$$

$$\begin{aligned} \hat{H}^{(2)}_{SOC} &= \hat{H}^{(2)}_{SSO} + \hat{H}^{(2)}_{SOO} \\ &= \sum_i \sum_{j \neq i} \hat{\mathbf{g}}_{i,j}^{\mathbf{2el-SOC}} \\ &= -\frac{\alpha^2}{2} \sum_i \sum_{j \neq i} r_{ij}^{-3} \hat{\mathbf{l}}_{ij} (\hat{\mathbf{s}}_i + \mathbf{2}\hat{\mathbf{s}}_j) \end{aligned} \tag{2.40}$$

where $\alpha = \mathrm{c}^{-1}$ is the fine structure constant in atomic units, $\hat{I}_{iA} = (\hat{r}_{iA}\ \mathrm{X}\ \hat{p}_i)$ is the angular momentum of the *i*th electron relative to nucleus A at position R_A with atomic charge Z_A. $\hat{r}_i$, $\hat{s}_i$ and $\hat{p}_i$ are the position, spin and momentum operator of the *i*th electron. $\hat{r}_{iA}$ = $\hat{r}_i - R_A$ with magnitude r_{iA} denotes the position of *i*th electron relative to atom A. $\hat{r}_{ij}$ = $\hat{r}_i$ - $\hat{r}_j$ is the interelectronic distance between i^{th} and j^{th} electron and $\hat{I}_{ij} = (\hat{r}_{ij}\ \mathrm{X}\ \hat{p}_i)$ defines the angular momentum relative to this electron. The two-electron term has contributions from the spin-same-orbit (SSO) and spin-other-orbit (SOO) terms and they play an important role in a quantitative treatment of SOC. This operator, without any approximation, would be difficult to handle exactly due to highly expensive computational calculations for larger number of atoms. Thus, the mean field/effective potential approaches in which the operator is written as an effective one-electron operator are commonly used. The corresponding one-electron operator is given by

$$\hat{H}_{SOC} \cong \sum_i \hat{\mathbf{h}}_{\mathbf{i}}^{(\mathbf{eff})} \hat{\mathbf{s}}_{\mathbf{i}} \tag{2.41}$$

The computational complexity of this operator is much lower than that of the full two-electron operator. In this thesis, we have used mean field approach (SOMF) derived and implement by Hess et al. as implemented in Orca.[137,138]

2.7 Zero-Field Splitting Parameters

The lifting of spin-state degeneracy for systems with S ≥1 in the absence of any applied magnetic field is known as zero-field splitting. The ZFS majorly originates from spin-orbit coupling (SOC) and spin-spin coupling (SSC). ZFS originates largely from the SOC constant of a transition metal center and the crystal field effects exerted on it. On the other hand, spin-spin coupling plays a lesser role in governing ZFS.

2.7.1 Spin Hamiltonian for ZFS

The ZFS is described in terms of spin Hamiltonian. The spin Hamiltonian, in the absence of exchange interactions and nuclear spin, is written as

$$\begin{aligned} \hat{H}_{spin} &= \hat{H}_{Ze} + \hat{H}_{ZFS} \\ &= \mu_B \vec{B} g \hat{S} + \hat{S} D \hat{S} \end{aligned} \tag{2.42}$$

Here, μ_B is the Bohr magneton, $\hat{S}$ is the spin operator of the ground state, $\vec{B}$ is the magnetic flux density, and g, and D are the symmetric g- and ZFS-matrices respectively. $\hat{H}_{spin}$ is the model spin Hamiltonian operating of 2S+1 number of basis functions $|S, M_S>$ with M_S = S, S-1, ..., -S.

2.7.1.1 The *D* tensor

D can be diagonalized in a principal axis frame in cartesian coordinate and expressed as

$$\hat{H}_{ZFS} = D\left[S_z^2 - \frac{S(S+1)}{3}\right] + E[S_x^2 - S_y^2] \tag{2.43}$$

D and E are the axial and rhombic ZFS parameters respectively, given as

$$D = D_{zz} - 1/2(D_{xx} + D_{yy}); E = 1/2(D_{xx} - D_{yy}) \tag{2.44}$$

where D_{xx}, D_{yy} and D_{zz} are the diagonal element of the D tensor. The axes for the coordinate system x, y, and z are chosen to fulfill the condition $0 \leq |E/D| \leq 1/3$. The ratio $|E/D|$ is known as the rhombicity parameter.

2.7.1.2 The *g* tensor

The Zeeman term in the spin Hamiltonian that describes the interaction of the magnetic moments of the electrons with the external magnetic field is given by

$$\hat{H}_{Ze} = \mu_B \vec{B} g \hat{S} \tag{2.45}$$

The matrix representation of the Hamiltonian reads as

$$\hat{H}_{Ze} = \mu_B \begin{bmatrix} B_x & B_y & B_z \end{bmatrix} \begin{bmatrix} g_{xx} & g_{xy} & g_{xz} \\ g_{yx} & g_{yy} & g_{yz} \\ g_{zx} & g_{zy} & g_{zz} \end{bmatrix} \begin{bmatrix} \hat{S}_x \\ \hat{S}_y \\ \hat{S}_z \end{bmatrix} \tag{2.46}$$

To describe the direction of magnetization and the magnitude of magnetic anisotropy, only diagonal terms of the g-tensor matrix are examined. If the system is isotropic, all the three diagonal elements will be equal i.e., $g_{xx} = g_{yy} = g_{zz}$ and the system does not have any magnetic anisotropy. If $g_z > g_y \approx g_x$, the z-axis is considered as the easy axis i.e., it is the favorable direction of magnetization and is known as uniaxial anisotropy. In contrast, $g_x \approx g_y > g_z$ signifies easy plane anisotropy and $g_z > g_y > g_x$ represents the case of triaxial anisotropy.

2.8 Harmonic Oscillator Model of Aromaticity (HOMA) index

HOMA is defined as the normalized sum of squared deviations of bond lengths from the optimal value that are assumed for a fully aromatic system. Among the simplest, most successful, and widely used aromaticity indices, it is known for its simplicity, success, and wide usage. The HOMA index according to Kygowski et al.[139,140] is expressed as

$$HOMA = 1 - \frac{\alpha}{n} \sum_{i=1}^{n} (R_i - R_{opt})^2 \tag{2.47}$$

where α is the normalization factor (257.7), n is the number of C-C bonds, R_i is the bond length computed from DFT calculations, R_{opt} is the optimal bond length for aromatic compounds with value of 1.388 Å for C-C bond. For a fully aromatic system, HOMA = 1, and for non-aromatic systems, HOMA = 0.

CHAPTER 3

Investigations of magnetic anisotropy and spin-crossover behavior of Fe(III)-TBP complexes

3.1 Introduction

Current interest of SMMs that exhibit a barrier to the magnetic relaxation lies in their prospective applications in the high-density information storage,[141] quantum computing,[142] molecular spintronics[7,143] and magnetic refrigeration.[144] The slow magnetic relaxation in these molecules is characterized by an energy barrier, U_{eff}, to magnetic moment reversal. The barrier to magnetic relaxation is determined by the magnitude of total spin at the ground state as well as the magnitude of the axial anisotropy.[145] The magnetic properties of single molecule magnets are controlled by the magnitude of magnetic anisotropy, which can be modulated based on rational design of ligands.[48] Mononuclear metal complexes containing rare earth (4f-metal) elements exhibit quite large magnetic anisotropy due to strong spin-orbit coupling and large unquenched orbital contribution to the magnetic moments.[146–155] In parallel development with lanthanides based SMMs, highly symmetric 3d transition metal complexes with relatively smaller magnetic moments are also gaining popularity in the recent years.[51] Mononuclear 3d transition metal complexes with high axial symmetry have shown sign of unquenched orbital momentum with considerable spin-orbit coupling and moderate magnetic anisotropy.[156–158]

A penta coordinated Fe(III) complex was reported by Mossin et al. with the intermediate ground-spin state that exhibits slow magnetic relaxation along with the axial

ZFS with D = -11 cm^{-1}.[159] Feng et al. synthesized two penta-coordinated Fe(III) complexes i.e. $[(PMe_3)_2FeCl_3]$ (here, complex **3.2**) and $[(PMe_2Ph)_2FeCl_3]$ having close to ideal TBP geometry.[160] The IS state was observed to be the ground state from DC susceptibility measurements data. The spin-crossover to HS state was captured in complex $[(PMe_2Ph)_2FeCl_3]$.[160] A very high value of ZFS i.e. D = -50 cm^{-1} for first and a moderate value of -17 cm^{-1} for second complex was observed. The authors claimed that the reported D for the first complex is the maximum among all the reported Fe(III) complexes. Later, these two Fe(III) based complexes were theoretically investigated using *ab initio* calculations by Chowdhury et al. and the magnetic anisotropy was found to be significantly influenced by axial ligands.[161]

In this work, we have explored the electronic structure and magnetic properties of the experimentally synthesized complex i.e. complex **3.2**, applying density functional theory (DFT) and *ab initio* wave function-based multi-configurational methods such as CASSCF and NEVPT2. A close to ideal TBP geometry, small size, neutral charge, and half-integral spin ground state makes complex **3.2** the ideal system to exhibit high magnetic anisotropy with further imposing the question, can we enhance the D value by modulating the ligand environment in the Fe(III) TBP complexes? To find an answer, we have modelled 14 complexes (Figure 3.1) with the aim of studying the effect of ligand environment, ligand-metal covalency, and ground-spin state on magnetic anisotropy.

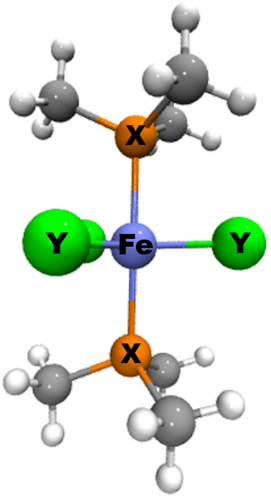

Complex	X(Axial)	Y(Equatorial)	Acronym
3.1	P	F	3.1_{HS}–PF
3.2	P	Cl	3.2_{IS}–PCl
3.3	P	Br	3.3_{IS}–PBr
3.4	P	I	3.4_{IS}–PI
3.5	N	F	3.5_{HS}–NF
3.6	N	Cl	3.6_{HS}–NCl
3.7	N	Br	3.7_{HS}–NBr
3.8	N	I	3.8_{HS}–NI
3.9	As	F	3.9_{HS}–AsF
3.10	As	Cl	3.10_{IS}–AsCl
3.11	As	Br	3.11_{IS}–AsBr
3.12	As	I	3.12_{IS}–AsI
3.13	N/P	Br	3.13_{IS}–NPBr
3.14	As/P	Br	3.14_{IS}–AsPBr
3.15	N/As	Br	3.15_{IS}–NAsBr

Figure 3.1: Structure of modelled Fe (III) complexes, $[Fe(XMe_3)_2(Y)_3]$. Here, X = P, N, As, and Y = F, Cl, Br, I. The complexes are acronymed based on the serial number followed by the ground-spin state (as a subscript) and ligands attached to it at axial and equatorial positions respectively. Out of these 15 complexes, complex 3.2 has already been synthesized by Feng et al. Complex 3.2 has been investigated especially for benchmarking purpose.

To explore the ligand environment, the donor atoms from group XV (i.e. N, P, and As) in the axial ligands are varied and the effect on the magnetic anisotropy is investigated. Additionally, the influence of halide ligands (F^-, Cl^-, Br^-, and I^-) at the equatorial position is also studied. A detailed investigation of electronic structure with change in ligand environment is carried out and the origin of the spin-crossover and large zero-field splitting is explored. Complexes **3.1**, **3.3** and **3.4** are designed replacing all the equatorial chloride ligand in **3.2** by fluoride, bromide and iodide respectively. Complexes **3.5**, **3.6**, **3.7** and **3.8** contain trimethylamine and complexes **3.9**, **3.10**, **3.11** and **3.12** contain trimethylarsine at the axial positions replacing trimethylphosphine in complexes **3.1**, **3.2**, **3.3** and **3.4** respectively. Complex **3.13** at axial position contains trimethylamine and trimethylphosphine, while complex **3.14** contains trimethylphospine and trimethylarsine and complex **3.15** has trimethylamine and trimethylarsine with bromide at the equatorial position for the last three complexes.

3.2 Computational Methods

The molecular geometries of all the modelled complexes are optimized applying density functional theory (DFT) using hybrid B3LYP exchange-correlation functional.[162,163] The localized atom centered valence triple-zeta with two sets of polarization functions, def2-TZVPP,[164] basis sets are used for all the calculations. The resolution of identity (RI) approximation, as implemented in ORCA,[137,165] is used to approximate the various integral accuracy to speed up the computations without losing their accuracy. Def2/JK auxiliary basis sets are used along with RI approximation and chain-of-spheres (RIJ-COSX) approximation to exact exchange.[166,167] A reformulated version of Grimme's DFT dispersion correction with Becke-Johnson damping (DFT-D3(BJ)) is included in the geometry optimization.[168,169] It turned out that D3(BJ) produces accurate molecular geometry and is especially crucial to reproduce the experimental axial metal-ligand distances for complex **3.2**. Increased integration grids (Grid 5 in ORCA convention) and tight SCF convergence criteria are used in all the calculations.[170–172] The atomic charges are obtained using Hirshfeld charges. The bond order analysis is based on the Mayer bond order.[173] Single point energies of the DFT optimized structures are calculated using SA-CASSCF/NEVPT2 calculation on top of ground state geometry to look into the spin-crossover phenomenon. For closely lying states, multireference SA-CASSCF calculations are advocated to produce improved results as compared to SS-CASSCF configuration interaction calculation for energy difference between spin-states. SA-CASSCF performs a constraint minimization of a weighted sum over energies of multiple states. With the SA approximation, both ground and excited state wave

functions are described by state-specific configuration interaction (CI) coefficients but use a global single set of orbitals.[174] A similar observation was made by Roemelt et al. that the state-specific energies may not be well converged due to missing balance in the appropriateness of a given active space in recovering part of dynamic correlation.[175]

The ZFS parameters arising from the spin-orbit coupling of the ground state and excited state are extracted using the effective Hamiltonian ($\hat{H}_{eff}$) theory.[176] SOC Hamiltonian, $\hat{H}_{SOC}$, based on an approximated version of Breit-Pauli Hamiltonian, where SOC integrals are treated by spin-orbit mean field approximation,[177] is used to account for the spin-orbit coupling. ZFS parameters are obtained from SO-CI treatment of SOF states obtained from *ab initio* calculations based on the complete active space self-consistent field (CASSCF) approach. The dynamical correlations for SOF states are included using the N-electron valence state perturbation theory (NEVPT2) method.

3.2.1 Selection of active space and number of roots

The proper choice of active space and nroots is crucial to achieve appropriate convergence in the multi-configurational methods. The minimal active space i.e. CAS (5,5) containing five d-electrons in five d-orbitals of Fe does not predict the correct ground-spin state of the complex **3.2**. Chowdhury et al. noticed that the spin state of the complex is sensitive to the axial Fe-P bond and suggested to include the p_z-orbitals of axial P ligands in the active space.[161] Hence, the expanded active space i.e. CAS (9,7) which includes the four p_z-electrons of P-atom along with the five d-electrons of Fe in two p_z-orbitals of P and five d-orbitals of Fe is used for all the calculations. The active orbitals are shown in Figure 3.2a.

The effect of inclusion of nroots of excited state and their contribution to magnetic anisotropy is important and is well explained by Llanos et al.[178] The choice of nroots of particular multiplicity is important for reducing the computational cost and to include only those low-lying excited states (roots), which actively participate in the mixing of states. Also, including states lying higher in energy affects the description of optimized orbitals of lower lying states which are important.[176,179] The selection of nroots is system specific and for the complexes under study, the procedure followed for the inclusion of appropriate nroots of particular multiplicity is thoroughly explained. It is observed that by the inclusion of all the roots of respective multiplicities, the calculated D value is -18.25 cm^{-1}(Table A.1) from SA-CASSCF calculations which is very small in comparison to -50 cm^{-1} reported experimentally[160] and we are not able to perform the NEVPT2 calculations on all the roots due to huge computational resource requirement of the calculation. It marks the significance of inclusion of only low lying excited roots of different multiplicities. The selection of nroots is based on the energy

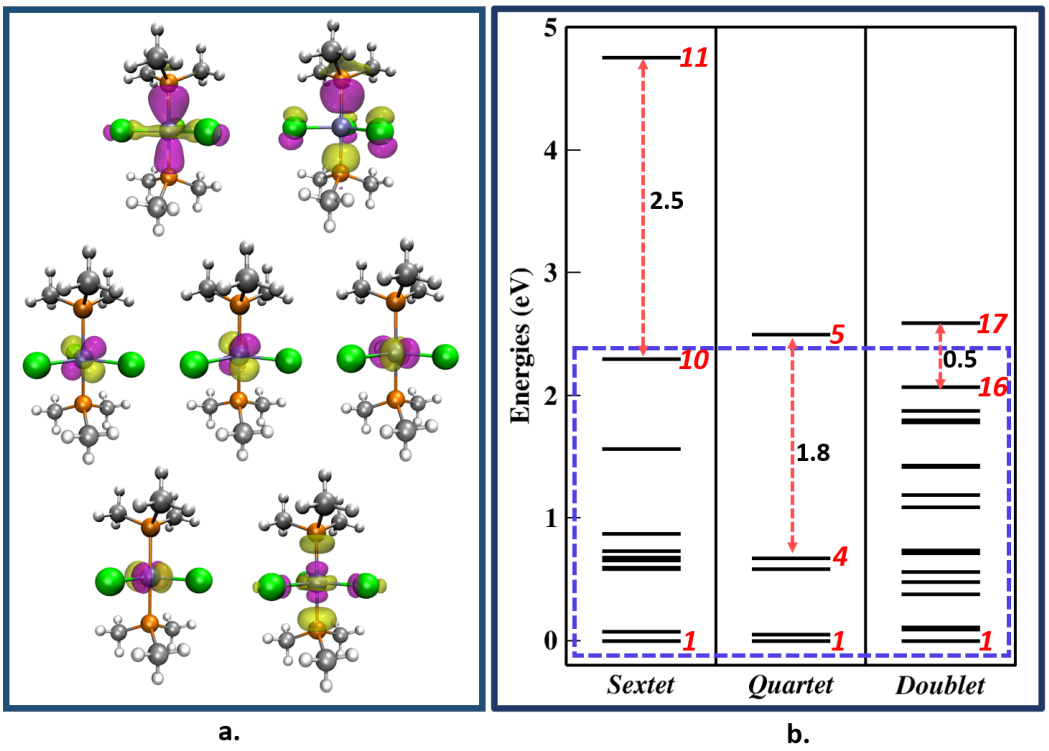

Figure 3.2: (**a**.) Active orbitals generated after SA-CASSCF calculations with active space CAS (9, 7). (**b**.) Energy spectra of nroots of multiplets obtained from converged SA-CASSCF(9,7) calculation with 21 roots of sextet, 224 roots of quartet and 490 roots of doublet. Only a few roots are shown in the diagram to highlight the energy difference between the chosen nroots and the one higher in energy. Here, the relative energies of all the roots with respect to the lowest root of the respective multiplicities are plotted.

spectra of nroots of multiplets of complex **3.2** which is obtained from the converged SA-CASSCF(9,7) calculation with 21 roots of sextet, 224 roots of quartet and 490 roots of doublet (Figure 3.2b). It can be observed from the energy spectra that 10 roots of sextet, 4 roots of quartet and 16 roots of doublet are low-lying and closer in energies and lies within the range of ~2 eV. Further, for sextet state, the energy gap between 10^{th} and 11^{th} number of root is quite large. Therefore, only 10 roots of sextet out of total 21 roots are considered for further calculations. For quartet state, although the 5^{th} root is close to 2 eV, but due to large energy gap between 4^{th} and 5^{th} root, only 4 low-lying roots are considered. On a similar basis, 16 roots of the doublet are taken into consideration. Hence, 10 roots of sextet, 4 roots of quartet, and 16 roots of doublet out of total 21, 224, and 490 roots of respective multiplicities are considered. All the states of a given multiplicity are equally weighed.

3.3 Results and Discussion

A detailed investigation of the electronic structure and magnetic properties of all the complexes is done. In the following subsections, firstly the discussion of ground-spin state of all the complexes is presented. Followed by a comprehensive discussion, the spin-state energetics and the observation of spin-crossover in some complexes is discussed. The origin of large zero field splitting is addressed in the subsequent subsection.

3.3.1 Ground-Spin State

The complex **3.2** is optimized in the three possible spin states, i.e. HS (S=5/2), IS (S=3/2) and LS (S=1/2) state. The geometry optimizations and the corresponding energy minima at the high-, low- and intermediate-spin states are confirmed by the absence of any imaginary vibrational frequencies. From the DFT optimized geometries, the IS quartet state is found to be the ground-spin state with the adiabatic energy difference of 20.40 kJ/mol with respect to HS sextet state and 70.97 kJ/mol compared to LS doublet state. The IS ground state for the complex is also observed by Feng et al.[160] from DC susceptibility measurements data and Chowdhury et al.[161] from *ab initio* calculations respectively. All the other modelled complexes are optimized employing the same B3LYP-D3/def2-TZVPP method. The DFT optimized energies of all the complexes (**3.1-3.15**) in all spin states (HS, IS and LS) are tabulated in Table A.2 and the optimized structural parameters are given in Table A.3 and A.4. From the comparison of energies of complexes in HS, IS and LS state, it is observed that for all the complexes, the LS state is always higher in energy. The IS state is found to be the ground-spin state for complexes **3.2**, **3.3**, **3.4**, **3.11**, **3.12**, **3.13** and **3.14**. Further, the prediction of ground-spin state for these complexes from DFT is also validated with SA-CASSCF/NEVPT2 calculations. All the multireference calculations are performed using the CAS(9,7) active space. The vertical excitation energies are calculated at the ground-spin state geometry of the respective complexes obtained from DFT. In agreement with DFT calculations for complex **3.2**, **3.3**, **3.4**, **3.11**, **3.12**, **3.13** and **3.14**, IS state is stabilized as ground state. Along with these, complex **3.10** and **3.15**, are also observed to be in IS ground state for which the HS state is predicted to be the ground state from DFT. To understand the dissimilarity for these two complexes, the energy difference between the HS and IS state is investigated and is tabulated in Table 3.1.

From the energy difference data, it is realized that the adiabatic energy difference between the HS and IS state from DFT is very small for complex **3.10** and **3.15**. A small energy gap is also observed for complex **3.13**. It has already been reported that hybrid functionals tend to stabilize the HS state as the ground state when the energy difference

Table 3.1: Adiabatic energy difference ($\Delta E^{adia.}_{HS-IS}$) (kJ/mol) between the HS and the IS state from DFT obtained at B3LYP-D3/def2-TZVPP level and the vertical excitation energies ($\Delta E^{vert.}_{HS-IS}$) (kJ/mol) between the ground quartet and excited sextet states from SA-CASSCF (9,7)/NEVPT2. The vertical excitation energies are calculated at the ground-spin state geometry of the respective complexes obtained from DFT. Energy difference is positive when the complex is stabilized in IS state and negative for HS stabilized complex.

Complex	Acronym	$\Delta E^{adia.}_{HS-IS}$	$\Delta E^{vert.}_{HS-IS}$	
		DFT	**SA-CASSCF**	**SA-NEVPT2**
3.1	3.1_{HS}-PF	-37.3	-132.4	-135.5
3.2	3.2_{IS}-PCl	20.4	53.9	12.9
3.3	3.3_{IS}-PBr	27.1	66.6	25.9
3.4	3.4_{IS}-PI	33.2	132.2	85.1
3.5	3.5_{HS}-NF	-64.3	-203.1	-156.9
3.6	3.6_{HS}-NCl	-56.2	-69.6	-139.1
3.7	3.7_{HS}-NBr	-58.4	-103.3	-127.2
3.8	3.8_{HS}-NI	-62.9	-24.1	-106.2
3.9	3.9_{HS}-AsF	-54.2	-66.4	-183.2
3.10[a]	3.10_{IS}-AsCl	-0.6 (9.1)	53.6	04.1
3.11	3.11_{IS}-AsBr	12.2	66.2	22.3
3.12	3.12_{IS}-AsI	21.8	77.6	40.1
3.13[a]	3.13_{IS}-NPBr	0.6 (13.4)	66.4	14.9
3.14	3.14_{IS}-AsPBr	20.1	65.3	23.1
3.15[b]	3.15_{IS}-NAsBr	-4.8 (8.7)	70.7	19.5

[a] The values in bracket are calculated with reparametrized B3LYP with 15% HF exchange. [b] For this complex, 10% HF exchange is considered.
These values are chosen to match the DFT ground-spin state that is consistent with SA-NEVPT2.

between the two states is not too large. Therefore, for complexes with small energy difference i.e. **3.10**, **3.13** and **3.15**, we performed calculations with different hybrid and gradient corrected functionals like OPBE, PBE0, PBE, and BLYP with the same basis set. To this end, the hybrid functionals i.e. OPBE and PBE0 are found to be biased towards the HS state whereas the gradient corrected functional i.e. PBE predicted the IS spin state as ground state. From BLYP functional, IS is observed to be ground state for complex **3.10** whereas HS for complex **3.13** and **3.15** (Table A.5). It has been proposed that the reparametrization of hybrid functionals by balanced admixture of exact and local exchange is necessary to produce the correct spin-state energetics.[180,181] Therefore, we also reparametrized the hybrid B3LYP functional by varying the percentage of exact exchange admixture from 0 to 25% (originally it is 20% for B3LYP) for complexes **3.10**, **3.13** and **3.15**. It has been found that decreasing the percentage of exact exchange

leads to a correct ground-spin state as predicted by multireference calculations. A linear relationship is observed in $\Delta E^{adia.}_{HS-IS}$ and percentage of exact exchange admixture (Figure 3.3) as found by Reiher et al.[180–182]

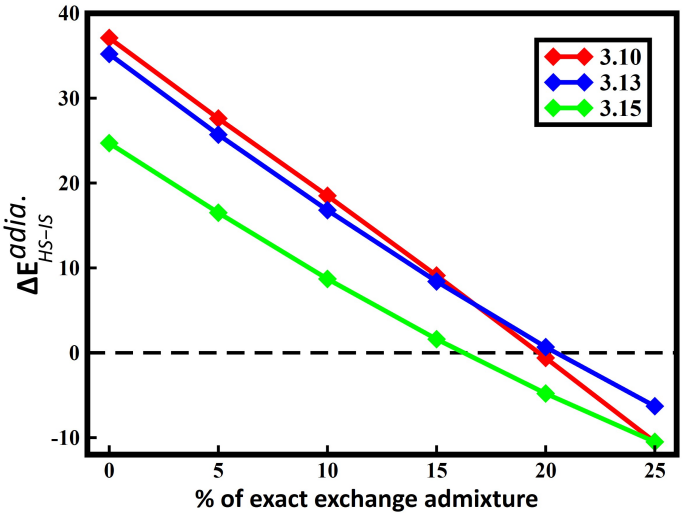

Figure 3.3: Variation of $\Delta E^{adia.}_{HS-IS}$ with the % of exact exchange admixture in the hybrid functional B3LYP for complex **3.10**, **3.13** and **3.15**. Originally there is 20% exact exchange admixture in the B3LYP functional.

For the rest of the complexes, good correspondence is noticed in adiabatic energy difference from DFT and the vertical excitation energies from multireference methods. For complexes **3.1**, **3.5**, **3.6**, **3.7**, **3.8** and **3.9**, HS state is stabilized as the ground state with both DFT and multireference calculations.

3.3.2 Spin-Crossover

The spin-crossover (SCO) appears in systems with small energy difference in the spin-states with IS state being more stable than the HS state. SCO in molecules is driven by the increase in entropy (ΔS) due to an increase in the metal-ligand (M-L) bond lengths accompanying the transition from IS to HS state. In the complexes under study, the major structural changes associated with the change in spin state are the M-L bond lengths along the symmetry axis i.e. Fe-P for experimentally synthesized complex **3.2**. The elongation of Fe-P bond lengths from 2.33 to 2.55 Å i.e. a change of 0.22 Å is obtained while switching from IS to HS state. The increase of M-L_{axial} bond lengths in HS state is due to population of electrons in the antibonding d_z^2 orbital of central metal which is directed towards the axial metal-ligand bonds. Therefore, the ligands pointing towards this direction experience more coulomb repulsion in HS state. In all the complexes, the change in M-L_{axial} bond length is observed in the range of 0.20 - 0.30

Å. However, a minor decrease of 0.01 Å is observed for the M-$L_{equatorial}$ bond lengths for complex **3.2**. For all the complexes, the change in equatorial bond lengths is not much pronounced (Table A.3). The entropy is observed to increase for all the complexes while switching from IS to HS state due to increase in M-L bond lengths along axial direction. The different contributions to ΔS are ΔS_{el}, ΔS_{vib}, ΔS_{rot} and ΔS_{trans}. The last two, i.e. ΔS_{rot} and ΔS_{trans} corresponding to the entropy variation due to rotation and translation respectively do not vary much. However, in a crossover from IS to HS state, the entropy change is dominated by the variation in the first two terms i.e. ΔS_{el} and ΔS_{vib}. The first term i.e. ΔS_{el} is the electronic entropy variation which is due to difference in degeneracy of HS and IS electronic states and hence, is same for all the complexes. Therefore, the major variation in ΔS is due to ΔS_{vib} (Table A.6). It suggests that SCO phenomenon is dominated by M-L bond lengths in axial direction only.

Table 3.2: Adiabatic energy difference ($\Delta E^{adia.}_{HS-IS}$), free energy change ($\Delta G^{adia.}_{HS-IS}$), enthalpy change ($\Delta H^{adia.}_{HS-IS}$) and entropy change ($T\Delta S^{adia.}_{HS-IS}$) in kJ/mol for all the complexes obtained at B3LYP-D3/def2-TZVPP level. $\Delta G^{adia.}_{HS-IS}$, $\Delta H^{adia.}_{HS-IS}$ and $T\Delta S^{adia.}_{HS-IS}$ are calculated at 300K.

Complex	**Acronym**	$\Delta E^{adia.}_{HS-IS}$	$\Delta \mathbf{G}^{adia.}_{HS-IS}$	$\Delta \mathbf{H}^{adia.}_{HS-IS}$	$\mathbf{T\Delta S}^{adia.}_{HS-IS}$
3.1	3.1_{HS}-PF	-37.3	-43.1	-38.3	4.7
3.2	3.2_{IS}-PCl	20.4	11.9	18.9	7.1
3.3	3.3_{IS}-PBr	27.1	20.8	25.5	4.9
3.4	3.4_{IS}-PI	33.2	24.6	34.1	9.1
3.5	3.5_{HS}-NF	-64.3	-72.1	-66.2	5.5
3.6	3.6_{HS}-NCl	-56.2	-64.5	-58.6	6.1
3.7	3.7_{HS}-NBr	-58.4	-66.1	-60.6	5.2
3.8	3.8_{HS}-NI	-62.9	-70.4	-65.4	4.9
3.9	3.9_{HS}-AsF	-54.2	-58.6	-57.2	1.3
3.10[a]	3.10_{IS}-AsCl	9.1	0.5	7.5	7.0
3.11	3.11_{IS}-AsBr	12.3	4.6	10.7	5.7
3.12	3.12_{IS}-AsI	21.9	14.7	19.7	4.9
3.13[a]	3.13_{IS}-NPBr	8.4	1.4	6.3	4.9
3.14	3.14_{IS}-AsPBr	20.1	10.8	21.1	10.2
3.15[b]	3.15_{IS}-NAsBr	8.7	0.7	6.3	5.8

[a] The values are calculated with reparametrized B3LYP with 15% HF exchange.
[b] For this complex, 10% HF exchange is considered.

Adiabatic energy difference from DFT provides an indication of SCO phenomenon. For the observation of spin-crossover, the energy gap between the two spin-states (i.e. $\Delta E^{adia.}_{HS-IS}$) was suggested to be 0 to 25 kJ/mol by Neese et al.[183] However, the more rational approach is to compare the Gibbs free energy difference i.e. $\Delta G^{adia.}_{HS-IS}$, which takes into account thermic and entropic corrections as well. The small value of Gibbs

free energy difference between the spin-state for some complexes indicates the possibility for the observation of spin-crossover between them (Table 3.2). From the table, it is observed that $\Delta G^{adia.}_{HS-IS}$ is small (< ~10 kJ/mol) for complexes **3.10, 3.11, 3.13, 3.14** and **3.15**, indicating switching between the bi-stable spin-states and hence these will behave as the superior spin-crossover materials. It is also observed that by varying the ligands at axial positions, with increasing softness of ligands, i.e. from N to As, $\Delta G^{adia.}_{HS-IS}$ decreases. However, by varying the ligands at equatorial positon i.e. from F to I, $\Delta G^{adia.}_{HS-IS}$ increases.

3.3.3 Zero Field Splitting

For the emergence of magnetic anisotropy in a molecule, both the sign and the magnitude of zero field splitting (ZFS) parameters are important. The large uniaxial anisotropy is signified by the negative sign of D and its large magnitude together with small E, which influences the possibility of observing slow magnetic relaxation.

For complex **3.2**, ZFS parameter, D, calculated by SA-CASSCF (9,7) calculation for intermediate ground-spin state geometry is -37.27 cm^{-1} (Table A.1) which further improves to -44.78 cm^{-1} (Table 3.3) upon inclusion of dynamical correlations using NEVPT2 calculation. The value is in nice agreement with the experimentally reported value of -50 cm^{-1}. From these NEVPT2 results, it is manifested that dynamical correlations play an important role in the calculation of ZFS value. Therefore, for all the modelled systems, D value is reported by the inclusion of dynamical correlations. The D values obtained from SA-CASSCF are provided in the Table A.7. The reason for the observed high value of D for complex **3.2** is the presence of axial symmetry which leads to quenching of Jahn-Teller distortion.[161] This is also reflected in very small degeneracy breaking of lowest lying d_{xz} and d_{yz} orbitals (Figure 3.4). With such a small splitting of d-orbitals in systems with close to ideal axial symmetry, ground and first excited states lie very close to each other in quasi-degenerate manner and lead to effective mixing and high first order spin-orbit coupling. This is reflected in the ZFS value contribution of first excited state which accounts for the major part of total ZFS.

Following the results for complex **3.2**, the zero-field splitting is calculated from NEVPT2 calculations on the wavefunction generated by SA-CASSCF for all the complexes in HS as well as IS state on their corresponding geometries. For complexes **3.2**, **3.3**, **3.4**, **3.10**, **3.11**, **3.12**, **3.13**, **3.14** and **3.15**, the large negative ZFS in the range of -40 to -60 cm^{-1} is calculated in the IS state on the respective optimized geometry. The value reduces to a relatively smaller magnitude, < -3 cm^{-1} for the HS state on the geometry optimized in the HS state. An exception is observed for complex **3.4** and **3.12** where a notable spin-orbit coupling is coming from a heavy iodide ligand.[184] The large

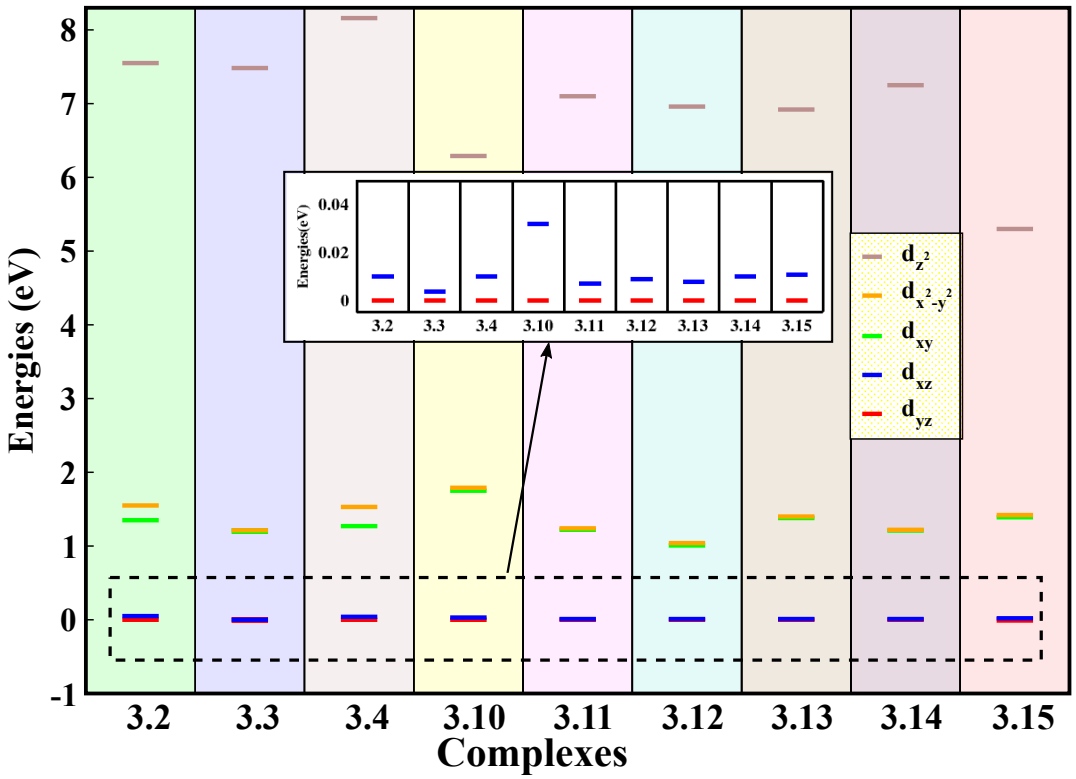

Figure 3.4: The 3d-orbital energy levels obtained from the SA-CASSCF(9,7) calculations for all the 9 predicted SMMs. The ground state 3d-orbitals occupations for these complexes are $d^2_{yz}d^1_{xz}d^1_{xy}d^1_{x^2-y^2}d^0_{z^2}$. The inset plot is the zoomed view of the energy difference between d_{yz} and d_{xz} orbitals.

SOC in these complexes lowers the energy of the quartet excited state and brings it closer to the sextet ground state and provides a D value of -9.78 and -18.02 cm^{-1} respectively. However, for other complexes which are stabilized in the HS state, a very small amount of zero-field splitting, < -4 cm^{-1}, is observed in both the spin-states on their respective geometries. The reason for the lower value of ZFS in the case of the HS state is the quenching of orbital angular momentum in Fe(III) ion with d^5 electronic configuration with the five singly occupied d-orbitals in the HS state. In the case of an isotropic electronic distribution as in Fe(III) HS state, the D value should ideally be zero.[185] This is due to the fact that the first-order spin-orbit coupling term goes to zero as total orbital angular momentum becomes zero (L=0). The only contribution to ZFS comes from second-order spin-orbit coupling which arises due to the mixing of the ground HS state with the excited IS state. Hence, the complexes with large ZFS in the IS state are studied in more detail and are discussed in the following discussion.

The ZFS can be correlated with the energy difference between the quartet ground and excited spin-free states. It has been well recognized that the excitation of electron between the same $|m_l|$ states in spin-conserved case leads to negative contribution

Table 3.3: D value (cm^{-1}) of all complexes from SA-NEVPT2 calculations on top of CASSCF (9,7) in HS and IS state on their respective geometries.

Complex	Acronym	D value (cm^{-1})	
		HS	IS
3.1	3.1_{HS}-PF	-01.29	-03.66
3.2	3.2_{IS}-PCl	-01.56	-44.78
3.3	3.3_{IS}-PBr	-02.43	-58.09
3.4	3.4_{IS}-PI	-09.78	-42.06
3.5	3.5_{HS}-NF	-01.82	-02.94
3.6	3.6_{HS}-NCl	-00.84	-02.21
3.7	3.7_{HS}-NBr	-01.45	-02.13
3.8	3.8_{HS}-NI	-00.45	-02.29
3.9	3.9_{HS}-AsF	-00.31	-01.72
3.10	3.10_{IS}-AsCl	-01.30	-51.66
3.11	3.11_{IS}-AsBr	-01.80	-54.89
3.12	3.12_{IS}-AsI	-18.02	-54.94
3.13	3.13_{IS}-NPBr	-02.06	-57.42
3.14	3.14_{IS}-AsPBr	-02.10	-54.86
3.15	3.15_{IS}-NAsBr	-01.67	-51.87

to D whereas between the different $|m_l|$ states in spin-conserved case leads to positive contribution to the overall value of zero field splitting.[186,187] In CASSCF converged CI ground state wavefunction, major contribution comes from $d^2_{yz}d^1_{xz}d^1_{xy}d^1_{x^2-y^2}d^0_{z^2}$ configuration and that of first excited state from $d^1_{yz}d^2_{xz}d^1_{xy}d^1_{x^2-y^2}d^0_{z^2}$ configuration following the excitation of electron from d_{yz} to d_{xz}. For second and third excited state, it comes from $d^1_{yz}d^1_{xz}d^2_{xy}d^1_{x^2-y^2}d^0_{z^2}$ and $d^1_{yz}d^1_{xz}d^1_{xy}d^2_{x^2-y^2}d^0_{z^2}$ configuration respectively. Since the excitation from d_{yz} to d_{xz} takes place between the same $|m_l|$ states, it will give negative contribution to D whereas the excitation between d_{yz} and d_{xy} or $d_{x^2-y^2}$ leads to positive contribution due to transition between different $|m_l|$ state within the spin-conserved environment (Table 3.4). Further, the magnitude of negative or positive contribution to D depends on the energy difference between the ground and excited sub-levels. Since, there is a slight energy difference between the ground and first excited sub-levels in these complexes, therefore, the energy required for electronic transition from ground state to first excited state is quite low, leading to enhancement of spin-orbit coupling between the ground and the first excited state. It leads to large negative contribution to D from the first excited state. However, due to larger energy gap between the ground state and second and third excited state, the magnitude of positive contribution is small compared to the larger negative contribution from first excited state, resulting in overall negative D value for the complexes (Table 3.4).

In modeled complex **3.3**, with bromide at equatorial position replacing chloride in complex **3.2**, an increase in D value is observed. It can be seen from Table 3.4 that the

Table 3.4: Lowest spin-free energy levels (cm^{-1}) of the complexes for quartet excited states along with their individual contribution to D and E (cm^{-1}) computed using SA-CASSCF/NEVPT2 method with (9,7) active space. Here, the wavefunction of the excited states 1, 2 and 3 presents the major contribution from $d^1_{yz}d^2_{xz}d^1_{xy}d^1_{x^2-y^2}d^0_{z^2}$ [12110], $d^1_{yz}d^1_{xz}d^2_{xy}d^1_{x^2-y^2}d^0_{z^2}$ [11210] and $d^1_{yz}d^1_{xz}d^1_{xy}d^2_{x^2-y^2}d^0_{z^2}$ [11120] configurations respectively.

Complex	Excited states	Spin-free states	Contb. D	Contb. E
3.2	1 (0.87)	389.8	-40.68	-0.465
	2 (0.87)	6465.0	01.80	1.830
	3 (0.87)	7568.4	01.20	-1.196
3.3	1 (0.84)	126.4	-60.95	-0.491
	2 (0.64)	5603.8	01.72	1.497
	3 (0.64)	5663.5	01.66	-1.396
3.4	1 (0.87)	215.0	-48.79	0.116
	2 (0.87)	5903.2	01.78	-1.830
	3 (0.87)	7711.7	01.12	1.108
3.10	1 (0.84)	424.7	-44.13	-1.474
	2 (0.83)	6269.3	01.82	0.965
	3 (0.83)	7460.3	01.30	-0.348
3.11	1 (0.81)	162.2	-57.38	-0.418
	2 (0.83)	5473.0	01.79	1.535
	3 (0.82)	5594.6	01.67	-1.380
3.12	1 (0.70)	123.7	-60.58	-0.310
	2 (0.80)	4187.9	02.23	-2.210
	3 (0.80)	4414.3	02.24	2.193
3.13	1 (0.52)	107.0	-57.53	-0.812
	2 (0.77)	4697.2	01.25	-1.495
	3 (0.77)	4802.4	01.82	1.643
3.14	1 (0.82)	164.9	-57.63	-0.437
	2 (0.74)	5506.3	01.65	-1.508
	3 (0.74)	5627.6	01.80	1.626
3.15	1 (0.70)	123.7	-53.13	0.224
	2 (0.72)	4670.2	00.91	-1.098
	3 (0.72)	4727.5	01.86	1.098

energy difference between the ground and first excited state decreases from complex **3.2** to **3.3**, i.e. from 389.8 to 126.4 cm^{-1} respectively. Hence, the electronic transition energy also decreases for complex **3.3**, leading to a larger D value. From the calculated d-orbital splitting diagram also, it can be seen that the energy difference between d_{yz} and d_{xz} decreases from complex **3.2** to **3.3**, indicating greater contribution to D for complex **3.3** (shown in inset of Figure 3.4). However, for complex **3.4**, the energy difference is larger than that for **3.3** leading to largest contribution to D from first excited state in case of complex **3.3**.

The overall D value for complexes **3.2**, **3.3** and **3.4** is related to the covalent charac-

Table 3.5: Average M-$L_{ax.}$ and M-$L_{equa.}$ Mayer bond order and Hirshfeld atomic charges obtained at B3LYP-D3/def2-TZVPP level in conjunction with def2/J auxiliary basis set. $L_{ax.}$ and $L_{equa.}$ are axial and equatorial ligands respectively.

Comp -lex	Acronym	Mayer bond order		Hirshfeld atomic charges		
		M-$L_{ax.}$	M-$L_{equa.}$	Fe	P/N/As	Cl/Br/I
3.2	3.2_{IS}-PCl	0.57	0.80	0.11	0.25	-0.27
3.3	3.3_{IS}-PBr	0.56	0.76	0.08	0.25	-0.25
3.4	3.4_{IS}-PI	0.59	0.79	0.01	0.24	-0.20
3.10	3.10_{IS}-AsCl	0.49	0.79	0.10	0.30	-0.28
3.11	3.11_{IS}-AsBr	0.48	0.76	0.07	0.28	-0.28
3.12	3.12_{IS}-AsI	0.51	0.79	0.07	0.28	-0.25
3.13	3.13_{IS}-NPBr	0.30/0.63	0.83	0.13	-0.04/0.27	-0.24
3.14	3.14_{IS}-AsPBr	0.64/0.44	0.83	0.07	0.28/0.25	-0.25
3.15	3.15_{IS}-NAsBr	0.23/0.62	0.84	0.13	-0.04/0.31	-0.25

ter of the Fe-halide bonds. This is reflected in the Mayer's bond order (Table 3.5) where bond order of Fe-Br (0.76) is smaller and Fe-Cl (0.80) and Fe-I (0.79) have comparable bond order leading to largest D value for complex **3.3** with Br as equatorial ligand and similar D value for complex **3.2** and **3.4** with comparable bond order. The halogen ligands are known for their π-donation ability, which increases from Cl to I in the group. From the Hirshfeld charge analysis (Table 3.5), it is observed that the positive charge on Fe and negative charge on halide decreases from Cl to I due to more charge transfer from halogen to ligand as we progress down the group. Hence, the D value is expected to increase with the increase in π-donation strength. The trend is followed from Cl to Br where D value is observed to be increased. However, an unexpected decrease is observed with I at equatorial position. This unexpected decrease is due to larger bond order of Fe-I than the Fe-Br bond. The same trend is observed in Co(II) complexes by Drahos et al. by varying the halide ligands at axial position which is a result of interplay between ligand field splitting by the halide ligand and the M-X covalency.[188]

For complexes **3.10**, **3.11** and **3.12**, trimethylarsine are positioned at the axial position. It is well known that softness of atom increases while progressing down the group. It is expected that with heavier and softer ligand i.e. As in place of P, the value of D should increase. Therefore, the D values for As containing ligands are larger than that of P containing ligands. From the analysis of Mayer bond order (Table 3.5), it is observed that the bond order of Fe-As (0.40-0.51) is smaller than Fe-P (0.51-0.59) bond order, accounting for the reason of more D value for As containing ligands than the P containing ligands. Also, with soft ligand i.e. As, there will be more charge transfer from axial ligand to metal, which is observed from the Hirshfeld atomic charges where positive charge on Fe decreases whereas on As, it increases as compared to that with P ligand, indicating easy transfer of electrons from ligand to metal in case of As. Hence,

increase in D value is observed with trimethylarsine ligands. The increase in D value in complexes **3.10**, **3.11** and **3.12** with the replacement of halide ligands can be elucidated from the increased charge transfer while progressing from Cl to I at the equatorial position. Less charge transfer from ligand to metal for complex **3.10** accounts for the smaller D value. Complexes **3.11** and **3.12** have comparable charge transfer leading to almost equal D values. Complexes **3.13**, **3.14** and **3.15** with asymmetric ligands exhibit zero field splitting in the range from -52 to -58 cm^{-1} in the IS ground state. The proportional energy difference between the quartet ground and first excited sub-level for the three complexes affirms the observed comparable D value.

Almost negligible rhombicity, $|E/D| < 0.03$ is calculated for these complexes which point towards high axiality of the magnetic anisotropy and leads to a reduction in the transition probability of relaxation through quantum tunneling (Table A.8).

From the above discussion, complexes **3.10, 3.11, 3.13, 3.14** and **3.15** possess Gibbs free energy difference below 10 kJ/mol and in parallel, possess large zero-field splitting in the IS state and reduce to small value in the HS state. Hence, these complexes emerge to be possible candidates for both spin-crossover and molecular magnetic materials.

3.4 Conclusions

We have modelled fourteen Fe(III)-TBP based complexes, out of which nine are stabilized in the IS ground state. They exhibit high magnetic anisotropy with D values in the range -40 to -60 cm^{-1} due to quasi-degenerate ground and first excited states. The ZFS is well correlated with the energy difference between the quartet ground and excited sub-levels. The ZFS is increased by varying the ligands from N to As at axial position. Among ligands at equatorial position, highest D value in the series is observed with the bromide ligand followed by iodide and chloride. The complexes containing fluoride at equatorial position possess HS ground state and hence, are not a good choice as ligands for SMM materials. Parallel to this, complexes with N at axial position also possess HS ground state. However, the complexes containing P or As in combination with N ligands provide superior materials. These asymmetric ligands point towards a new avenue in modelling of single ion magnets giving a way to design and synthesize SMMs based on asymmetric ligand substitution. For the observation of spin-crossover phenomenon, adiabatic energy difference between the two spin states and more relevant Gibbs free energy difference is a decisive parameter. It is observed that $\Delta G^{adia.}_{HS-IS}$ decreases with increasing softness of ligands at axial position i.e. from N to As whereas it increases when the ligands are substituted from F to I at equatorial position. Complexes **3.10**, **3.11**, **3.13**, **3.14** and **3.15** among all the designed complexes possess small $|\Delta G^{adia.}_{HS-IS}|$ (i.e. $< \sim$10.0 kJ/mol) indicating the spin-crossover behavior of these systems.

CHAPTER 4

Single-molecule magnetism in linear Fe(I) complexes

4.1 Introduction

Transition metal (TM) complexes with low coordination numbers show signs of unquenched orbital angular momentum. To this end, linear or quasi-linear two-coordinate complexes emerge as the choicest complexes for large anisotropic energy barriers.[57–60,64] An ample number of two- and three-coordinate complexes featuring Fe(II) center are already reported with intriguing magnetic properties.[19,46,61–63] However, in Fe(II) based complexes, the slow relaxation of magnetization is observed only in the presence of d.c. field owing to Fe(II) being a non-Kramer ion. Therefore, taking advantage of Kramer's theorem and thus, attenuating quantum tunneling of magnetization (QTM) within ground doublet, Zadrozny et al. reported the first prominent example of two co-ordinate complexes of Fe(I) i.e. $[Fe(C(SiMe_3)_3)_2]^{-1}$ with an exceptionally high energy barrier of 226 cm^{-1} under zero applied field with magnetic blocking upto 4.5 K.[189,190] Later on, Werncke et al. reported another Fe(I) complex, $[Fe(N(SiMe_3)_2)_2]^{-}$, but with a comparatively small energy barrier of 64 cm^{-1} which is attributed to the reduced symmetry of the complex.[191] Further, two linear and one T-shaped Fe(I) complexes employing bulky NHC (N-heterocyclic carbene) ligands were synthesized by Ouyang et al.[192] Later on, they carried the magnetic characterization of these complexes explaining multiple magnetic relaxation pathways existing in the three co-ordinate complexes.[193]

In recent years, although two-coordinate Fe(I) complexes with sterically bulky ligands have been synthesized,[192,194,195] but a thorough study to underpin the origin of

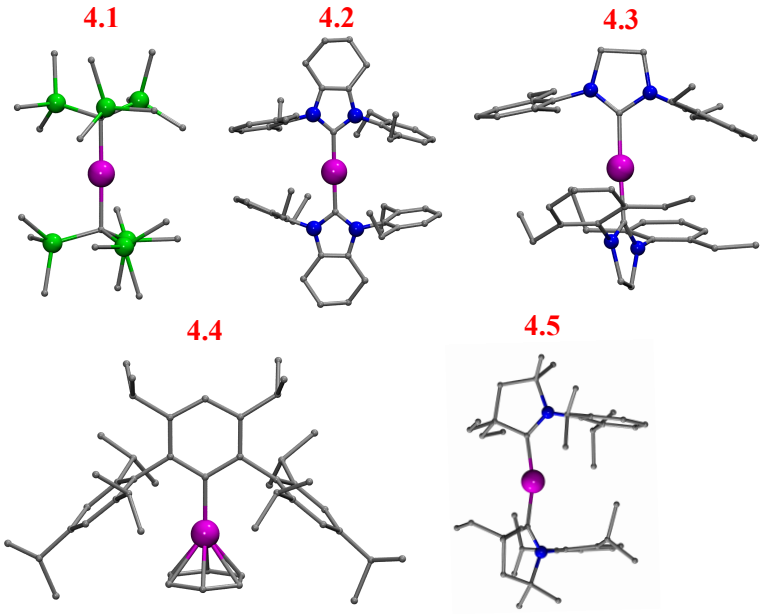

Figure 4.1: Complexes under study. $[Fe(C(SiMe_3)_3)_2]^{-1}$ **(4.1)**; $[Fe(cyIDep)_2]^{+1}$ **(4.2)**; $[Fe(sIDep)_2]^{+1}]$ **(4.3)**; $[(\eta^6\text{-}C_6H_6)FeAr^*\text{-}3,5\text{-}Pr^i_2]$ **(4.4)**; $[(CAAC)_2Fe]^{+1}$ **(4.5)**. $SiMe_3$ = trimethylsilyl; cyIDep = 1,3-bis(2′,6′-diethylphenyl)-4,5-$(CH_2)_4$-imidazol-2-ylidene; sIDep = 1,3-bis(2′,6′-diethylphenyl)-imidazolin-2-ylidene; Ar*-3,5-Pr^i_2 = C_6H-2,6-$(C_6H_2$-2,4,6-$Pr^i_3)_2$-3,5-Pr^i_2 ; CAAC = cyclic (alkyl)(amino)carbene. Colour code: Pink for Fe, Blue for N, Green for Si, Gray for C. Hydrogens are omitted for clarity.

magnetic anisotropy in these complexes has not been done yet. The present work aims to gain an in-depth understanding of magnetic anisotropy in a series of linear two-coordinate Fe(I) complexes, employing *ab initio* calculations. To this end, we have chosen five experimentally reported Fe(I) complexes, namely, $[Fe(C(SiMe_3)_3)_2]^{-1}$ **(4.1)**,[190] $[Fe(cyIDep)_2]^{+1}$ **(4.2)**, $[Fe(sIDep)_2]^{+1}]$ **(4.3)**,[192] $[(\eta^6\text{-}C_6H_6)FeAr^*\text{-}3,5\text{-}Pr^i_2]$ **(4.4)**[194] and $[(CAAC)_2Fe]^{+1}$ **(4.5)**[195] as shown in Figure 4.1. Since complex **4.1** is experimentally characterized with high spin-reversal barrier, it is plumped for benchmarking the methodology. Complexes **4.2** and **4.3** are experimentally synthesized and are reported to possess large axial zero field splitting parameter with opposite signs (-62.4 cm^{-1} for **4.2** and +34.0 cm^{-1} for **4.3**) from *ab initio* DDCI3 calculations. Despite the large values reported for the complexes, both are experimentally reported with absence of SIM behavior under any applied fields. We have explicitly studied the electronic structure of these complexes to have a fundamental understanding of this peculiar behavior. We strive to accomplish this by probing their magnetic relaxation pathways. Complexes **4.4** and **4.5** are also experimentally synthesized by Ni et al.[194] and Ung et al.[195] respectively. However, to the best of our knowledge, there is no report on the study of magnetic anisotropy of the complexes. Possessing underlying requisites for superior SIMs i.e., linear structure and Fe(I) metal center and hence, unquenched orbital angular

momentum, we speculate if the later complexes could manifest themselves as potential contenders for SIMs. Consequently, we have scrutinized the two complexes to investigate their magnetic anisotropy and hence, their potential to act as SIMs.

4.2 Computational Methods

All the ground and excited state energies and wave function calculations are performed on the experimentally reported X-ray crystal structures' geometries. The molecular coordinate system is chosen in such a way that Fe(I) is the origin of the coordinate system and the z-axis points approximately towards the donor atoms of the ligands. In complex **4.4**, the z-axis is oriented towards the centroid of the benzene ring bonded in the η^6 fashion. The correlated calculations are done using Complete Active Space Self Consisent Field (CASSCF)[196] together with N-Electron Valence Perturbation Theory (NEVPT2).[197] The Fe(I) possess d^7 electronic configuration giving rise to 10 quartets (S=3/2) and 40 doublets (S=1/2) states. To benchmark the methodology, we performed the calculation for complex **4.1** considering all the roots of quartet and doublet and another calculation with all roots of quartet only. However, the doublet states do not show any significant contribution to the D values, therefore, the calculations are performed accounting for only 10 quartet states (Table B.1). The CASSCF energy levels are obtained by state-averaging these states in the active space consisting of 7 electrons distributed in 5 3d orbitals i.e., CAS (7,5). The effect of dynamical correlations is included by performing NEVPT2 calculations on top of CASSCF converged wavefunction.

Scalar relativistic effects are taken into account by employing second-order Douglas-Kroll-Hess triple-DKH-def2-TZVP basis set[198] (DKH2/CASSCF/NEVPT2/SOC/DKH-def2-TZVP) and auxiliary basis set is generated automatically using AUTOAUX keyword.[199] Tight self-consistent field (SCF) convergence criteria (10^{-10} au) is used in all the calculations. The spin-orbit interactions along with the Zeeman interactions are incorporated by the quasi-degenerate perturbation theory (QDPT) approach.[200,201] Magnetic parameters (D, $|E/D|$ and g-tensors) have been computed using effective Hamiltonian theory as implemented in the ORCA (4.0.1.2) program package.[137,202] Ab initio ligand field theory (AILFT) analysis based on wavefunction obtained from SA-CASSCF/NEVPT2 has been employed to obtain precise d-orbital splitting pattern of the studied complexes.[203] Ab initio blocking barriers for relaxation mechanisms have been computed from SINGLE_ANISO module[204,205] as implemented in Orca v5.0.1.[138] The spin-phonon coupling coefficient, C_k, in all the three directions i.e., x, y and z, is calculated using Eq. 4.1 as the second derivative of the g component in x, y or z direction with respect to the distortion in the structure, Q_k corresponding to the vibrational

mode k as[206]

$$C_k = \frac{\hbar}{4\pi}\left(\frac{\delta^2 g}{\delta Q_k^2}\right)\frac{1}{m_k \nu_k} \tag{4.1}$$

where m_k and ν_k are the reduced mass and the frequency of the k^{th} vibrational mode. To include the effect of the thermal population of the vibrational mode, B_k is calculated using Bose-Einstein statistics as

$$B_k = \frac{C_k}{e^{\nu_k/k_B T} - 1} \tag{4.2}$$

A detailed procedure to calculate the C_k is provided in Appendix, Sec. B.6. The *ab initio* CASSCF and CASPT2 calculations are also performed in OpenMolcas (19.11).[207,208] For CASSCF calculations in OpenMolcas, the relativistic contracted atomic natural orbital type basis sets i.e., [ANO-RCC...5s4p2d] for Fe, [ANO-RCC...4s3p] for Si, [ANO-RCC...3s2p] for N and C and [ANO-RCC...2s] for H are employed.[209] To account for spin-orbit effects, AMFI spin-orbit operator is used and DKH Hamiltonian is considered for scalar relativistic effect. The resolution-of-identity approximation is employed to accelerate the calculation.[210]

4.3 Results and Discussion

4.3.1 ZFS parameters and *g* tensors

For complex **4.1**, the alternating current magnetic susceptibility measurements yield high value of spin reversal barrier i.e., U_{eff} = 226 cm^{-1}.[189] The large U_{eff} value is the result of unquenched orbital angular momentum, thereby, maximizing the magnetic moment. The computed D value from SA-CASSCF calculations is -102.16 cm^{-1} which further enhances to -109.13 cm^{-1} when dynamical correlations are taken into account employing NEVPT2. Since for non-integral spin complexes, U_{eff} corresponds to $|D|(S^2\text{-}1/4)$, the D value of -109.13 cm^{-1} leads to U_{eff} of 218.26 cm^{-1}. The value is in nice agreement with the experimentally observed value of 226 cm^{-1}. Moreover, the D value of -108.55 cm^{-1} is obtained from MS-CASPT2 calculations, in nice agreement with that obtained from NEVPT2. For all the studied complexes, the SA-CASSCF/NEVPT2 and MS-CASPT2 computed D values are collected in Table 4.1. For complexes **4.2**, **4.4** and **4.5**, negative D value is obtained from NEVPT2 with moderate magnitude in the range -33 to -80 cm^{-1}. However, a positive D value of 40.30 cm^{-1} is observed for complex **4.3**. CASPT2 also results in negative D values for complexes **4.2**, **4.4** and **4.5** with comparable magnitude as obtained from NEVPT2 calculations.

However, a discrepancy is observed between the computed D value for complex **4.3** for which NEVPT2 yields +40.30 cm^{-1} in contrast to the CASPT2 value of -25.84 cm^{-1}, although +34 cm^{-1} is reported by DDCI3 calculations by Meng et al.[193] This discrepancy is considered as a calculation artifact in case of complexes with triaxial aniostropy ($g_z > g_y > g_x$)(explained in detail in following paragraphs) i.e., when the ratio of $|E/D|$ approaches 1/3. In that case, the sign of D is ill-defined.[211] Owing to the large D value, complex **4.4** proffers itself as the second Fe(I) centered complex with large ZFS among other linear Fe(I) complexes reported so far with a relatively low spin-reversal barrier.

Table 4.1: SA-CASSCF/NEVPT2 and MS-CASPT2 computed D values for all the studied Fe(I) complexes.

Complexes	SA-CASSCF[a]		SA-NEVPT2[a]		SA-CASSCF[b]		MS-CASPT2[b]	
	D	***|E/D|***	***D***	***|E/D|***	***D***	***|E/D|***	***D***	***|E/D|***
4.1[c]	-102.16	0.0004	-109.13	0.0004	-106.08	0.0003	-108.55	0.0002
4.2[d]	-68.89	0.1745	-33.32	0.0475	-78.85	0.1223	-28.32	0.0824
4.3[d]	42.38	0.0918	40.30	0.2475	45.34	0.1244	-25.84[e]	0.3219
4.4	-90.23	0.0038	-79.06	0.0046	-90.29	0.0049	-67.97	0.0067
4.5	-24.77	0.2837	-65.10	0.0467	-27.24	0.2071	-21.96	0.2282

[a]The calculations are performed with DKH-def2-TZVP basis set in Orca.
[b]The calculations are performed with ANO-RCC-VDZ basis set in OpenMolcas.
[c]The U_{eff} value of 226 cm^{-1} is reported experimentally instead of D value.[190]
[d]The D values of -62.4 and 34.0 cm^{-1} are reported for complex 4.2 and 4.3 respectively from DDCI3 method by Meng et al.[193]
[e]The sign of D is ill-defined for complexes with $|E/D|$ values approaching to 1/3.

For complexes with negative value of D, the Kramers doublet with the maximum spin projection is the ground-state while reverse is true with positive D value.[212] The negative value of D for all complexes except **4.3** implies that the Kramers doublets (KDs), with the projection of total angular momentum $m_J = \pm 7/2$ is the ground state for these complexes. However, for complex **4.3** with positive D value, the ground state KDs has $m_J = \pm 1/2$ as the projection of total angular momentum.

For a molecule to possess uniaxial anisotropy with slow relaxation of magnetization under no applied field, apart from negative axial ZFS (D), the negligibly small rhombicity i.e., $|E/D|$ ratio is required.[213] The non-zero value of E allows mixing of $\pm M_s$ levels, leading to spin relaxation through quantum tunneling.[214] The SA-CASSCF/NEVPT2 computed $|E/D|$ ratio of all the complexes are collected in Table 4.1. Complexes **4.1** and **4.4** exhibit negligibly small rhombicity i.e., $|E/D|$ <0.005 (Table 4.1) indicating infinitesimal transition probability of relaxation through quantum tunneling of magnetization (QTM) within the ground-state Kramers doublet. Complexes **4.2** and **4.5** possess small $|E/D|$ ~0.04, implying partial relaxation through quantum tunneling of magnetization within the ground-state Kramers doublet. However, for complex **4.3**,

large $|E/D|$ is observed indicating relaxation of magnetization through the ground-state Kramers doublet. Besides ZFS parameters, the g tensor corresponding to a pair of KDs, which imparts the preferential direction of magnetization in a particular spin-orbit state, is an important parameter for governing the efficiency of SIMs.[215]

Table 4.2: Computed g tensors for the lowest four Kramers doublets for all the complexes.

Complexes	KD (cm^{-1})	g_x	g_y	g_z	g_z-angle (deg)
4.1	0	0.002	0.002	9.970	0
	218.27	0.985	0.986	5.876	0.05
	460.56	0.964	1.007	1.874	0.41
	710.06	0.011	0.015	2.036	0.02
4.2	0	0.388	0.412	10.25	0
	66.88	2.760	3.650	7.328	67.51
	124.74	0.371	0.884	7.941	89.14
	328.16	0.277	0.642	9.101	83.49
4.3	0	1.634	3.205	7.522	0
	87.70	1.887	1.967	5.522	89.98
	754.08	0.703	1.905	8.647	89.88
	940.57	2.350	3.343	3.479	4.07
4.4	0	0.029	0.029	9.516	0
	158.13	3.404	3.412	4.246	0.0
	523.70	0.208	3.243	3.572	89.99
	701.54	0.114	0.132	2.643	0.0
4.5	0	0.310	0.361	9.720	0
	130.64	0.403	0.904	5.727	6.17
	293.58	1.841	3.027	4.301	89.27
	584.26	1.564	1.885	3.659	89.71

Complexes with $g_z > g_y \approx g_x$ are characterized with easy axis anisotropy with g_z as the favorable direction of magnetization. In contrast, $g_x \approx g_y > g_z$ signifies easy plane anisotropy and $g_z > g_y > g_x$ represents the case of triaxial anisotropy.[211] The g tensors for the ground-state and the lowest three excited states of all the complexes are

shown in Table 4.2. For complexes **4.1** and **4.4**, the computed g tensors in the ground-state KDs are observed to show $g_z >> g_y \approx g_x$, indicating g_z as the favorable direction of magnetization with strong Ising type nature. This uniaxial magnetic anisotropy signifies negligible relaxation of magnetization from the ground state Kramers pair. However, for the first and higher excited states, the extent of uniaxiality is reduced. Moreover, along with the changes in g, the direction of magnetization of the excited state from the ground state (measured as g_z angle in Table 4.2) also deviates. These decreased uniaxiality and non-coincidence of the anisotropy axis of excited state with respect to the ground-state leads to faster relaxation of magnetization from the corresponding state.[215]

For complexes **4.2** and **4.5**, although the g-tensor show axiality with $g_z >> g_y \approx g_x$, but lacks pure Ising nature. This suggests partial tunneling within the ground state KDs along with faster tunneling through the excited state with reduced uniaxiality and deviation of anisotropy axis from the ground state. Complex **4.3** is a peculiar case possessing triaxial anisotropy with $g_z > g_y > g_x$. This triaxial anisotropy has been observed earlier also for Co(II) compounds by Møller et al.[211] and Korchagin et al.[216]

4.3.2 Orbital interpretation of magnetic anisotropy

To gain a better understanding of the observed magnitude as well as the sign of D values for the studied complexes, we have analyzed the pattern of molecular d-orbitals splitting of these complexes obtained from AILFT analysis as shown in the top panel of Figure 4.2. For **4.1**, the d-orbital splitting is observed where the d_{z^2} is lowest in energy followed by closely degenerate pairs of $d_{x^2-y^2}$ and d_{xy} and then by d_{xz} and d_{yz}. The stabilization of d_{z^2} is a result of strong $3d_{z^2}$-$4s$ mixing as reported by Zadrozny et al.[189] Visual inspection of the shape of d_{z^2} orbital (bottom of Figure 4.2) reveals an appreciable overlap where the donut-like ring in the xy plane of d_{z^2} orbital mixes with the $4s$ orbital. This $3d_{z^2}$-$4s$ mixing is observed for all the complexes. Moreover, this $3d_{z^2}$-$4s$ is also evident from the analysis of Löwdin orbital composition of the $3d$-orbitals (Table B.2). The d_{z^2} orbital is observed to have a composition of ~80% with appreciable s-orbital character (~10%), however, the other d-orbitals are pure with ~95% composition. This pattern of d-orbital ordering of complex **4.1** results into the ground state with dominant electronic contribution from $d^2_{z^2}d^2_{x^2-y^2}d^1_{xy}d^1_{xz}d^1_{yz}$ and the first excited state has the major electronic contribution from $d^2_{z^2}d^1_{x^2-y^2}d^2_{xy}d^1_{xz}d^1_{yz}$. Since the energy gap between the ground and first excited state is very small i.e., 56.0 cm^{-1} (Table 4.3) and the excitation of an electron from ground to first excited state takes place between the same $|m_l|$ states, thus, the spin-conserved transition from $d_{x^2-y^2}$ to d_{xy} leads to large negative contribution to the D value. The second excited state is composed of several determinants with major contribution from $d^1_{z^2}d^2_{x^2-y^2}d^2_{xy}d^1_{xz}d^1_{yz}$. Here, the electron promotes to the states

with different $|m_l|$ values and the energy difference between the ground and second excited state is quite large (Table 4.3), hence, it gives a small positive contribution to the D value. Since the first excited state lies close to the ground-state, it governs the overall sign and magnitude of D leading to a high negative D value of -109.13 cm^{-1} for complex **4.1**.

For complex **4.2**, d_{z^2} orbital is again stabilized, however, in this complex, d_{xz} and d_{yz} orbitals are more stabilized as compared to d_{xy} and $d_{x^2-y^2}$ orbitals which is in contrast to the d-orbital splitting pattern observed for complex **4.1**. The significant interactions of the d_{xz} and d_{yz} orbitals of the Fe atom with the π-orbitals of the carbene ligand via π back-bonding interactions lead to stabilization of d_{xz} and d_{yz}. A considerable overlap between the carbene $p\pi$ type orbitals and metal d_{xz} and d_{yz} orbitals is visualized in Figure 4.2. Although the d_{xz} and d_{yz} are lower in energy, the complex possesses *non-Aufbau* ground state with electronic configuration, $d^2_{z^2}d^1_{xz}d^1_{yz}d^2_{xy}d^1_{x^2-y^2}$. The *non-Aufbau* electronic ground-state was also observed by Bunting et al. for Co(II) complex[64] and Ruiz et al. for ferrocenium complex.[217] The viable reason for this anomalous configuration is the small energy difference of d_{z^2} with d_{xz} and d_{yz} i.e., 0.097 and 0.174 eV respectively (Figure B.1). Since these d-orbitals are quasi-degenerate, therefore, in the *non-Aufbau* configuration ($d^2_{z^2}d^1_{xz}d^1_{yz}d^2_{xy}d^1_{x^2-y^2}$), the inter-electronic repulsion is minimized relative to the *Aufbau* ($d^2_{z^2}d^2_{xz}d^1_{yz}d^1_{xy}d^1_{x^2-y^2}$) configuration. Further, the first excited state will be attained by promoting an electron from d_{xy} to $d_{x^2-y^2}$ with small energy difference (52.0 cm^{-1}) and between same $|m_l|$ states leading to large negative contribution to the D value. The second excited state has the major contribution from $d^2_{z^2}d^1_{xz}d^2_{yz}d^1_{xy}d^1_{x^2-y^2}$ attained by transfer of an electron from d_{xy} to d_{yz} with small energy difference (143.7 cm^{-1}), leading to significant positive contribution to the D value. Thus, although the overall D value is negative but the magnitude is smaller due to large positive contribution from the second excited state.

In complex **4.3**, the imidazolin ylidine ring is substituted as ligand. It is known to exhibit better π accepting ability than imidazol ylidine[218] (in complex **4.2**) rendering more pronounced $d\pi$-$p\pi$ interactions and hence, stabilizes the d_{xz} orbital compared with the d_{z^2} and d_{yz} which are almost degenerate (Figure B.2). As a consequence of this pattern of d-orbital splitting and the different interelectronic repulsion between different d-orbitals, the ground state acquires *non-Aufbau* electronic configuration, $d^2_{xz}d^1_{z^2}d^2_{yz}d^1_{x^2-y^2}d^1_{xy}$ (similar to **4.2**). Since, the first and second excited states are achieved by promoting an electron from d_{yz} to $d_{x^2-y^2}$ and d_{xy} respectively with different $|m_l|$ states, both of them give a positive contribution to the D value. Hence, the complex exhibits an overall positive D value. Thus, the different splitting pattern due to better π-acceptor imidazoline ylidine than imidazol ylidine (in **4.2**) results in opposite signs of magnetic anisotropy for the two complexes. Another difference between

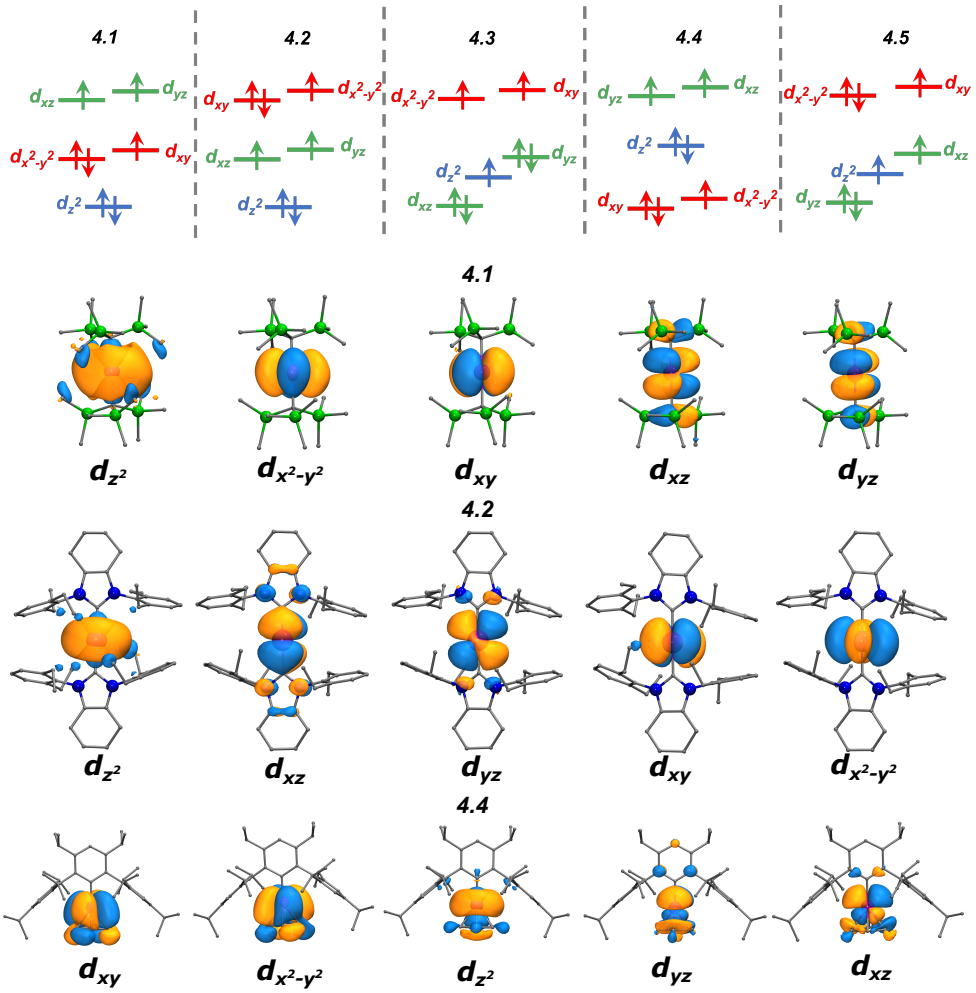

Figure 4.2: The qualitative representation of d-orbital splitting of all the complexes and the molecular d-orbitals in the order of increasing energies obtained from AILFT analysis of the SA-CASSCF/NEVPT2 calculations with active space of CAS(7,5) for complexes **4.1**, **4.3** and **4.4** at an isovalue of 0.02 a.u. The quantitative d-orbitals splitting is provided in the Fig. B.1.

the two molecules is the dihedral angle between the ligands attached to the complexes. Complex **4.2** renders dihedral angle of 14° in contrast to the large dihedral angle of 70° exhibited by complex **4.3** (tabulated in Table B.4). The different dihedral angles can also be the underlying rationale for the contrasting signs of magnetic anisotropy for the complexes **4.2** and **4.3** as also observed in Co complexes by Meng et al.[218]

The complex **4.4** is a peculiar case where quasi-degenerate d_{xy} and $d_{x^2-y^2}$ are lower in energy as compared to d_{z^2}. The analysis of molecular orbitals as shown in Figure 4.2 reveals a substantial overlap between the d_{xy} and $d_{x^2-y^2}$ orbitals of Fe with the π-electron cloud of the benzene ring which is binding to the Fe through η^6 fashion making a half-sandwich complex. The π-electron cloud of the benzene ring and the d_{xy} and $d_{x^2-y^2}$ orbitals of the Fe atom are lying perpendicular to the molecular axis. These orbitals can

Table 4.3: Lowest spin-free energy levels of the complexes with their individual contribution to D computed using SA-CASSCF/NEVPT2 with (7,5) active space.

Complex	Excited states	Spin-free states (cm^{-1})	Contb. D (cm^{-1})
4.1	1	56.0	-119.02
	2	5380.2	02.94
4.2	1	52.0	-103.54
	2	143.7	31.26
4.3	1	791.5	24.41
	2	1459.3	09.85
4.4	1	298.3	-85.19
	2	924.7	01.43
4.5	1	54.0	-112.24
	2	774.0	22.23

be considered as a linear combination of $p\pi$ orbitals of the benzene ring and d-orbitals (d_{xy} and $d_{x^2-y^2}$) of Fe atom indicating significant interactions and hence leading to substantial stabilization of these orbitals followed by d_{z^2} and subsequently by a closely degenerate pair of d_{xz} and d_{yz} orbitals. The outcome of this d-orbital ordering is the ground-state with electronic configuration $d^2_{xy}d^1_{x^2-y^2}d^2_{z^2}d^1_{yz}d^1_{xz}$. The promotion of electron from d_{xy} to $d_{x^2-y^2}$ i.e., between same $|m_l|$ states and with small energy difference (298.3 cm^{-1}) leads to first excitation providing large negative contribution to D value. Further, the second excited state is obtained by transfer of electron from d_{z^2} to $d_{x^2-y^2}$ causing small positive contribution to the D value, with overall negative magnetic anisotropy for the complex.

Complex **4.5**, accomodating CAAC ligand, a good π-accepting ligand, possesses d-orbital splitting pattern similar to that obtained for complex **4.3** with the only difference showing interchange of d_{yz} and d_{xz} orbitals. However, unlike complex **4.3**, the ground state electronic configuration for this complex is different with dominant contribution from $d^2_{yz}d^1_{z^2}d^1_{xz}d^2_{x^2-y^2}d^1_{xy}$ and the first excited state is obtained by transfer of electron from $d_{x^2-y^2}$ to d_{xy} with significant negative contribution to D value due to smaller energy gap (54.0 cm^{-1}). The second excited state is attained by electron transfer from d_{yz} to d_{z^2} giving notable positive contribution to D value. And the complex exhibits overall negative D value.

Thus, the different D values exhibited by these complexes are a result of distinct d-orbital splitting patterns caused by different ligands attached to the metal center, Fe(I).

4.3.3 Mechanism of magnetic relaxation

To have a qualitative understanding of the mechanism of magnetic relaxation, we have plotted *ab-initio* blocking barriers computed from SINGLE_ANISO approach as implemented in Orca as shown in Figure 4.3. The relaxation of magnetization can occur through three probable mechanistic pathways namely a) quantum tunneling of magnetization (QTM) within the ground KDs b) Orbach/Raman relaxation process where Raman relaxation process takes place through virtual transitions c) thermally assisted quantum tunneling of magnetization (TA-QTM) within excited KDs.[19] In the computed relaxation mechanism, the KDs are presented according to their magnetic moments. The numbers at each arrow connecting any two energy levels represent the matrix elements of transition-magnetic-moments between the connecting energy levels.

For complex **4.1** and **4.4**, the transition-magnetic-moment matrix elements between the ground state KDs are negligibly small i.e., 0.0007 and 0.009 respectively, ruling out the possibility of QTM through the ground state in these complexes. In addition to this, the calculated transition-magnetic-moment matrix element between the ground and first excited KDs of opposite magnetic moments are also very small in magnitude (0.0008 and 0.01 for **4.1** and **4.4** respectively), implying slow Orbach relaxation. However, the large transversal-magnetic-moment (0.32 for **4.1** and 1.1 for **4.4**) for the first excited state suggests relaxation to be operative through first excited state via TA-QTM.

In the case of complexes **4.2** and **4.5**, the computed transveral-magnetic-moment is 0.14 and 0.1 respectively in the ground state suggesting partial QTM to be operative through the ground state KDs. The larger magnitude of transition-magnetic-moment matrix elements of 1.3 and 1.1 for **4.2** and **4.5** respectively for the first excited state for both the complexes mark the major relaxation to proceed through this state. Besides, the off-diagonal matrix elements between the ground and first excited KDs of opposite magnetization are also moderate (0.42 and 1.0) opening up further relaxation pathways via Orbach relaxation. Therefore, for these complexes, multiple relaxation pathways are operational. On the other hand, for complex **4.3**, the $m_J = \pm 1/2$ is the ground state with a barrierless potential well which is also signified by the high magnitude of transition-magnetic-moment matrix element i.e., 1.8, suggesting faster relaxation within the ground state for this complex.

These relaxation pathways provide the plausible reason for no SIM behaviors under any applied field for complexes **4.2** and **4.3** as observed by Meng et al.[193] Since for complex **4.2**, due to multiple relaxation pathways i.e., partial QTM through the ground-state KDs and Orbach relaxation, the complex shows absence of SIM behavior. In contrast, complex **4.3** possessing barrierless potential well leads to relaxation within the ground-state KDs. Thus, both the complexes do not show any signatures of SIM

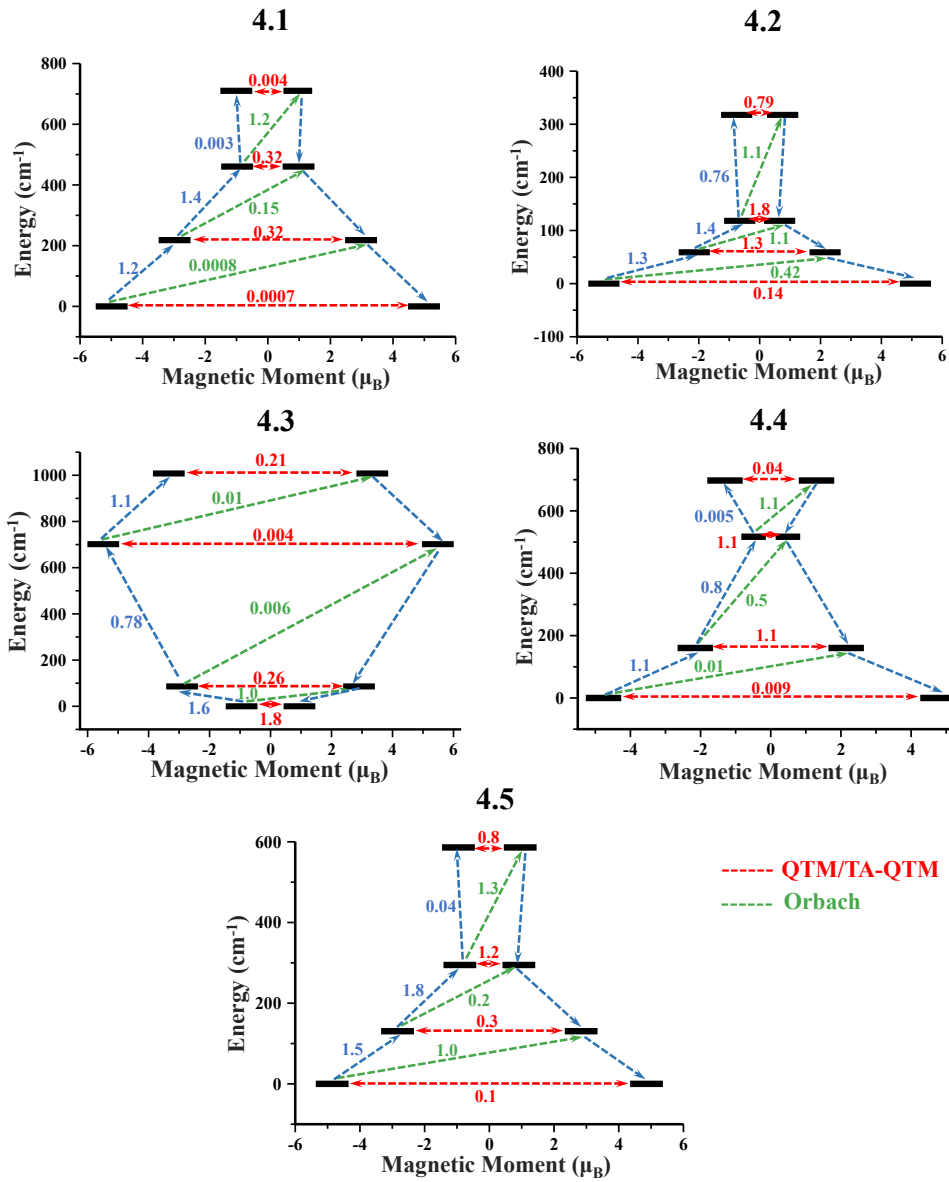

Figure 4.3: Ab initio magnetization blocking barrier for all the complexes. The black lines represent the Kramers doublets (KDs) as a function of the magnetic moment. The dotted red lines represent the QTM/TA-QTM. The dotted green lines denote the Orbach relaxation pathways. The dotted blue lines show the most probable relaxation pathway. The numbers at each connecting arrow represent transition-magnetic-moment matrix elements.

behavior.

4.3.3.1 Spin-phonon coupling

The spin-phonon coupling plays an important role in the spin relaxation process and is explored extensively with different approaches.[206,219,220] Therefore, to have an insight into the relaxation process, we have computed the spin-phonon coupling coefficients

i.e., C_k for complex **4.1** using Eq. 4.1. Since, complex **4.1** possess spin-reversal barrier of 218.26 cm^{-1}, therefore, only low energy vibrational modes with energy lower than the estimated spin reversal barrier (218.26 cm^{-1}) are considered to study the role of these vibrational modes in the relaxation process. The spin-phonon coupling coefficients calculated for all considered vibrational modes are collected in Table B.5. The vibrational modes with the largest intensity are the modes **39** and **50** (Figure B.4). These modes are associated with the vibrations of the methyl groups attached to the silicon atom. However, they possess very small spin-phonon coupling coefficients with computed C_k values of 1.3×10^{-5}, 1.3×10^{-5} and -8.8×10^{-5} in x, y and z directions (Table B.5) for mode **39** and 1.2×10^{-5}, 1.2×10^{-5} and -3.6×10^{-5} in x, y and z directions, respectively, for mode **50**. The thermal population of these modes obtained using Eq. 4.2 is shown in Fig. 4.4. At low temperatures, the thermal population of these modes is negligibly small (~0) and at higher temperatures, i.e., 300K, they are minute, viz. 0.08×10^{-4}(x), 0.08×10^{-4}(y), 0.55×10^{-4}(z) for mode **30** and 0.06×10^{-4}(x), 0.06×10^{-4}(y), 0.19×10^{-4}(z) for mode **50**. Thus, these two modes do not provide any contribution to the relaxation process. The next vibrational mode with large intensity is mode **47** which involves the stretching of Fe-N bond distance along with the methyl groups. They also possess small C_k coefficients (-1.0×10^{-5}, -9.3×10^{-6}, 2.1×10^{-5}) and thermal populations manifesting infinitesimal contribution to the relaxation.

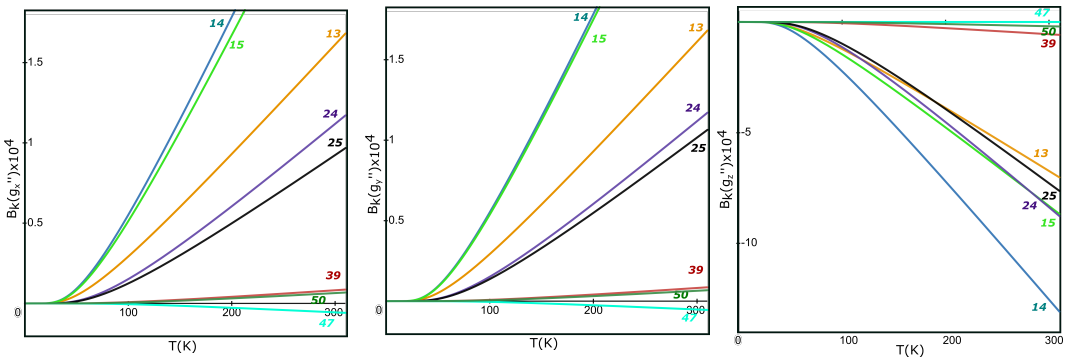

Figure 4.4: Calculated B_k values considering the second derivative of g tensor, in x, y, and z directions, for the low energy vibrational modes calculated at CASSCF level.

Further, the modes that are majorly responsible for the distortion of the coordination environment around the central metal atom are studied to understand their role in spin-phonon coupling. The different vibrational modes associated with the distortion of the Fe(I) center in order of decreasing distortion are modes **15, 14, 24, 25** and **13**. The most relevant vibrational modes are the modes **15** and **14** which are responsible for the large distortion of the Fe(I) center supplemented by the C atom of the ligands directly attached to it. These are mainly the bending vibrations and thus, are expected to

be detrimental contributors to spin-phonon coupling. However, they also possess very small spin-phonon coupling coefficients (Table B.5). At low temperatures, the thermal population of modes **15** and **14** is zero and at higher temperatures also, the population is negligibly small thereby giving a much weaker contribution of these modes to the relaxation process. The next significant vibrational modes associated with Fe centre are modes **24** and **25**. They also possess small C_k coefficients and thermal populations signifying their feeble contribution to the relaxation. The mode **13** is the weak stretching mode involving the variation in the Fe-C bond lengths. Since these vibrations cause very small changes in the bond lengths, they possess minuscule C_k and B_k values. All the other low intensity vibrational modes with energies <220 cm^{-1} also possess spin-phonon coupling coefficients with same orders of magnitude as of the aforementioned modes.

Since, the spin-phonon interactions are weak, the spin-phonon coupling coefficients are also calculated with the linear derivative of the g components using Eq. B.1 and is collected in Table B.6.[221,222] For all the low energy vibrational modes, these are also computed to be negligibly small with the feeble corresponding thermal populations of the different modes (Figure B.5). Thus, there is weak spin-phonon coupling in complex **4.1** and no vibrations are responsible for smaller barrier height for relaxation than the first excited state. Hence, the relaxation will majorly take place via the first excited state through TA-QTM with spin-reversal barrier of 218.26 cm^{-1} complementing well with the experimentally observed barrier of 226 cm^{-1}.

4.4 Conclusions

We have investigated the origin of single molecule magnetic behavior in a series of linear Fe(I) complexes employing state-of-the-art *ab initio* calculations. The different *d*-orbital splitting patterns are manifested by the complexes which is the ramification of the intrinsic nature of the ligands attached to the complex. Since the energetic ordering of *d*-orbitals is the decisive parameter for the magnitude and sign of zero field splitting parameter, all complexes except **4.1**, possess the *non-Aufbau* electronic ground state due to small energy difference in the *d*-orbitals showing a range of *D* values from -33 to -109 cm^{-1} and even positive *D* value for one of the complex. The complex **4.1** is characterized with large spin-reversal barrier of 218.26 cm^{-1} matching well with the experimental data. The calculation of spin-phonon coupling coefficients for the low frequency vibrational modes for the complex reveal weak spin-phonon coupling in the complex manifesting relaxation through the first excited state via TA-QTM. Complexes **4.2** and **4.3** are experimentally reported with absence of SIM behavior under any field, however, opposite signs of *D* value (negative for **4.2** and positive for **4.3**) are shown from *ab initio* calculations.[193] This observation is rationalized based on different patterns of *d*-

orbital splitting and their ground state occupancy. Moreover, the existence of multiple relaxation pathways with partial relaxation within ground state KDs for complex **4.2** and barrierless potential well triggering faster relaxation within the ground state KDs in complex **4.3** provides signatures for the absence of SIM behavior in these complexes. This is in well agreement with the experimentally observed behavior. Thus, moderate magnitude of magnetic anisotropy and faster quantum tunneling of relaxation are found to co-exist in these complexes. Moreover, the experimentally synthesized complexes **4.4** and **4.5** are characterized with large magnetic anisotropy of -79.06 and -65.10 cm^{-1} but complex **4.5** exhibits multiple relaxation pathways with partial tunneling within the ground state KDs. However, complex **4.4** possessing Ising type anisotropy and blocking of ground-state QTM is predicted as the possible candidate for SIM. Moreover, complex **4.4** is the Fe(I) complex to possess large ZFS value of -79.06 cm^{-1} followed by complex **4.1** (D=-109.13 cm^{-1}) among all other Fe(I) linear complexes reported so far.

CHAPTER 5

Investigation of magnetic exchange interactions in Blatter's diradicals obtained by coupling via its fused benzene ring

5.1 Introduction

An emerging interest for organic molecular magnets (OMMs) in the fabrication of spintronic devices has eventually thrust into the investigation of thermally stable organic radicals.[76,223] Being a fundamental source of spin, organic diradicals have attracted substantial attention of researchers for potential applications in the field of spintronics as memory storage and logic devices.[224–226] One of the major challenges faced by the community is obtaining room temperature stable organic radicals that exhibit strong ferromagnetic exchange interactions. Over the past few decades, a number of stable organic radicals including nitronyl nitroxide (NN), oxoverdazyl (OVER), dithiadiazolyl (DTDA) have been successfully developed.[77,227–229] One of the other thermally robust monoradical is benzotriazinyl (Blatter's) radical (shown in Fig. 5.1), which was first reported by Blatter and co-workers in 1968.[230] The radical has gained considerable attention after Koutentis et al. established easy synthetic strategies for super stable Blatter's radical.[84,85] Afterwards, focusing on electronic and magnetic properties, various magneto-structural correlations were also established by them in the π-stacked radicals of Blatter's radical.[231] Along with this, the radical has witnessed a growing interest with applications in spintronic devices. Ciccullo et al. demonstrated the excellent ability of

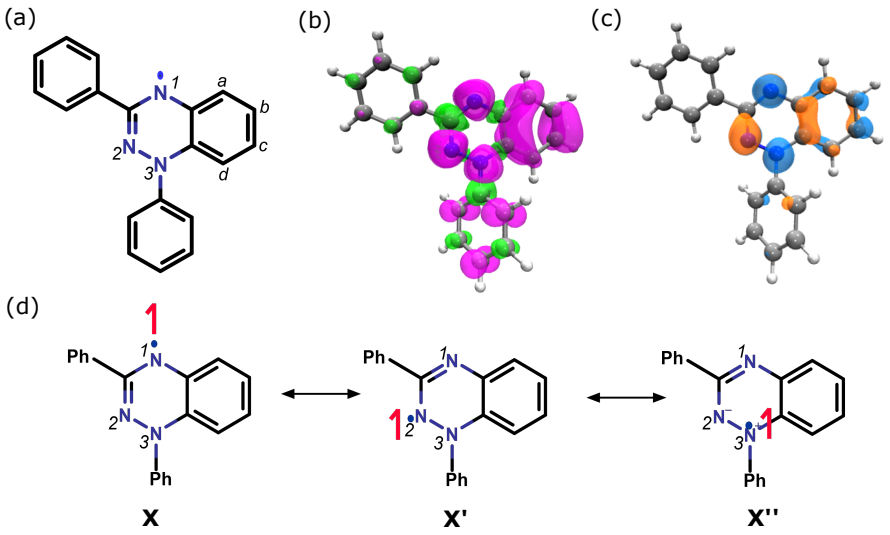

Figure 5.1: **(a)** Parent 1,2,3-benzotriazinyl (Blatter's) radical, **(b)** Löwdin spin density distribution where pink and green colors represents α and β spin with isovalue 1×10^{-3} $\mu_B/\text{Å}^3$ and **(c)** Singly occupied molecular orbital (SOMO) of Blatter's monoradical with isovalue 2×10^{-2} a.u. **(d)** Major contributing resonating structures of Blatter's monoradical indicating the delocalization of unpaired electron on all the three N-atoms.

using a Blatter's radical to create stable thin films, thus, opening the way for the radical to be used in devices.[232] With a biggest challenge to synthesize room temperature stable organic diradicals, Rajca et al. successfully coupled the stable nitronyl nitroxide (NN) as well as imino nitroxide (IN) radical with the Blatter's radical to obtain hybrid diradicals that exhibit reasonably strong ferromagnetic exchange interactions.[233,234] Recently, Zheng et al. reported the synthesis of diradical obtained by coupling the monomeric unit of Blatter's radical itself.[235,236]

For Blatter's monoradical, Löwdin spin density distribution, shown in Fig. 5.1b, reveals that the unpaired electron is not only confined to three N-atoms, but delocalizes across both the triazinyl and fused benzene ring. This unique spin density distribution of the radical makes this super stable spin source an appealing candidate for stable OMMs, further imposing the question, can we couple such mono-radicals to obtain Blatter's diradical with strong ferromagnetic exchange interactions? To find an answer priori to synthesis, in this work, we have computationally investigated the 10 possible isomers of di-Blatter diradical by coupling the monomeric unit of Blatter's radical via its fused benzene ring. Adopting various density based methods along with the multi-reference CASSCF/NEVPT2 calculations, magnetic exchange interactions are computed and are compared with the available experimental observations. As a peculiarity of Blatter's radical, the fractional spin-moment localization on all the three N-atoms yields multiple micro-magnetic centres. The pairwise exchange between the specific micro-magnetic centres is addressed with appropriate computational recipe.

Further, the Löwdin spin density distribution, shown in Fig. 5.1b, also reveals that all the N-atoms possess α-spin (positive spin density). Approximate 0.23 μ_B spin-moment was found on each of the three N-atoms. Even N3-atom also exhibits α-spin due to resonance contributing structures, shown in Fig 5.1d, which is in contrast to the empirical *spin alternation* and the similar *Ovchinnikov's* rule where alternate signs of spin density are expected at the adjacent sites.[237] This α-spin cloud over the triazinyl ring itself gives a first signature that simplest *spin alternation* rule cannot be applied to such radicals. Thus, as an alternative way, in this work, we also proposed a modified version of *spin alternation* rule called here as *zonal spin alternation* rule, which can be applied correctly to predict the nature of magnetic exchange interactions in such systems. Moreover, the presence of heteroatoms in the system is another factor that makes it challenging to predict the sign of exchange interactions according to *spin alternation* rule.

5.2 Computational Methods

For all the isomers of di-Blatter diradical under study, the molecular geometries are first optimized at UB3LYP/def2-TZVP level. The exchange interactions are then investigated applying different density as well as wave function-based *ab initio* multiconfigurational methods.[238–240] All the wave function-based and BS-DFT calculations are performed using *ORCA*,[137] while CBS-DFT calculations in *NWChem*.[241] The magnetic exchange interactions for the DFT based methods are extracted employing Eq. 2.31. The static, as well as dynamical electronic correlations, are accounted through CASSCF and NEVPT2 method respectively wherein the 2J values are obtained by using Eq. 2.23.[242,243] The multi-reference (CASSCF/NEVPT2) calculations of 2J's are benchmarked for a set of active spaces starting from minimal CAS(2,2) to CAS(6,6) for the experimentally observed **c-c** isomer (Appendix Sec. C.2). We observed that the minimum active space (i.e. accounting two SOMOs in the active space) underestimates the 2J values in the CASSCF method, due to lack of dynamical correlations. However, it gets compensated while accounting the dynamical correlations and produce a very close number as observed in the experiments as well as in other theoretical methods. Expanding the active space improves static correlations but overall 2J values get overestimated. These scenarios were also observed previously in the literature.[69,244–246] Considering all these facts, further, all the calculations are performed using CAS(2,2) active space along with the static and dynamic correlations.

5.3 Results and Discussion

All the possibilities of coupling the Blatter's radical with itself via fused benzene ring are investigated. As illustrated in Fig. 5.1a, fused benzene ring exhibits four distinct unsubstituted positions (marked as a,b,c and d in Fig. 5.1a) through which it can be coupled to other Blatter's moiety. So, in total 4×4, i.e. 16 constitutional isomers of di-Blatter diradical can be formed, but 6 of them being repetitive in combination (as **a-b** and **b-a** denotes the same isomer) give rise to 10 possible isomers with distinct atomic connections. Out of these 10 possibilities, isomers obtained by coupling the radical moieties via connecting sites "a" or "d" are sterically hindered with distorted geometry and large torsional angles. On the other hand, coupling via connecting sites "b" or "c" results in nearly planar geometry and less torsional angles. Fig. 5.2 illustrates the relative energies and the dihedral angle ϕ between two monomeric units optimized at UB3LYP/def2-TZVP level for all the 10 isomers. Among the 10 possibilities, the isomers with connecting sites "b" and "c", i.e., **b-b, b-c** and **c-c** are found to be energetically stable exhibiting a dihedral angle of $\sim 35^{\circ}$ as compared to those with connecting site "a" and "d" exhibiting large dihedral angles. Among the stable isomers, the diradical with mirror connecting cite "c", i.e. **c-c** (shown in inset of Fig. 5.2) has already been synthesized, however, the other two isomers i.e. **b-b** and **b-c** are also potentially stable candidates and are yet to be synthesized. The magnetic properties of the former were also studied applying SQUID magnetometry by Zheng and co-workers wherein an anti-ferromagnetic exchange with a $2J$ value of -444.19 cm^{-1} was observed by them.[235,236]

The computed $2J$ values for all the 10 isomers are summarized in Table 5.1. The isomers in which the radical moieties are coupled via one of the less sterically hindered connecting site "b" or "c" are observed to be anti-ferromagnetic in nature except the case of **c-d** isomer. On contrary, small ferromagnetic exchange is obtained for the distorted isomers in which both the connections are made with the sterically hindered connecting sites "a" and "d" i.e. **a-a, a-d** and **d-d**. This variation of the nature of the magnetic exchange interactions with the connecting sites can also be seen from Fig. 5.2 where red and green bars denotes anti-ferro and ferromagnetic exchange respectively. The nature of exchange coupling is further verified by using various density and wave function-based multi-configurational methods and is found to be concordant. For the experimentally synthesized **c-c** isomer, a good match is obtained by using traditional BS-DFT, which further improves by constraining the appropriate amount of magnetic moment on the spatially confined zones in CBS-DFT. The detailed criteria for zone selection in CBS-DFT calculations is discussed in Appendix, Sec. C.1.1. CASSCF calculations with minimal active space, i.e. CAS(2,2) provides underestimated exchange coupling as compared to the experimental value of -444.19 cm^{-1} which improves sig-

nificantly by the inclusion of dynamical correlation with NEVPT2 method.

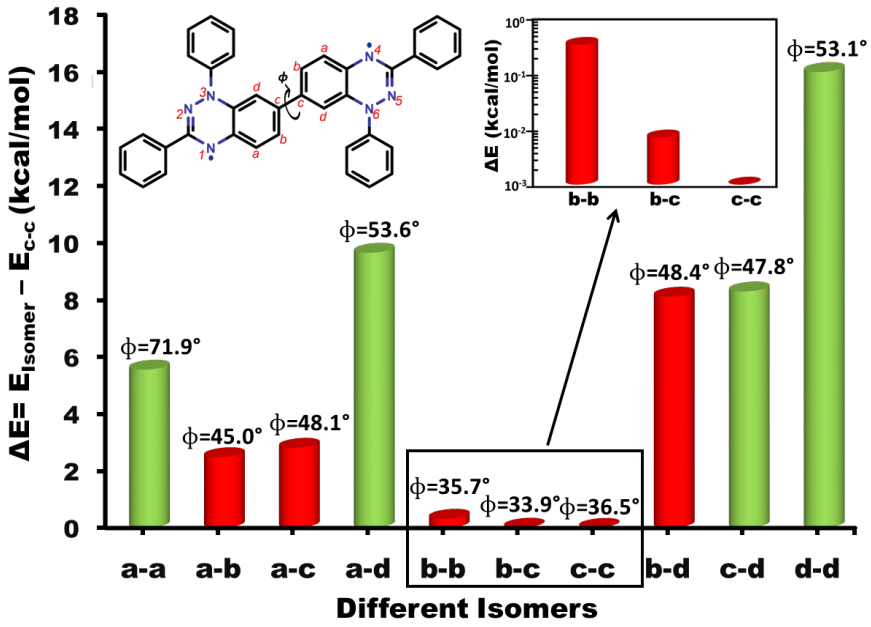

Figure 5.2: Relative energies (ΔE) of all the possible isomers of di-Blatter diradical, where ϕ is the dihedral angle between two monomeric units. The inset of the graph shows the zoomed view of the energy difference between the isomers **b-b**, **b-c** and **c-c** at logarithmic scale. The red and green colored bars corresponds to anti-ferro and ferromagnetic exchange interactions respectively.

Table 5.1: Calculated magnetic exchange coupling constant $2J(\text{cm}^{-1})$ for all the 10 possible isomers of di-Blatter diradical.

Possible	$2J(cm^{-1})$			
Isomers	BS-DFT	CBS-DFT	CASSCF[a]	NEVPT2[a]
a-a	4.94	4.38	8.77	17.99
a-b	-162.70	-127.28	-32.48	-103.15
a-c	-168.10	-168.01	-25.02	-92.39
a-d	31.44	32.42	15.80	30.50
b-b	-196.36	-165.48	-79.42	-158.02
b-c	-262.38	-219.46	-100.73	-240.54
c-c[b]	-599.92	-544.28	-164.16	-511.60
b-d	-59.56	-49.16	-16.02	-12.57
c-d	29.30	33.78	11.85	38.84
d-d	10.20	9.48	2.41	7.46

[a] The calculations are performed using CAS(2,2) active space.

[b] Synthesized and reported $2J$ value is -444.19 cm^{-1}.[235,236]

In the following subsections, we will discuss the proposed *zonal spin alternation* rule. Followed by a comprehensive discussion, the origin of dominant anti-ferromagnetic exchange in the stable conjugated isomers is provided. The weak ferromagnetic nature of the distorted diradicals originating from large torsional angles is addressed in the subsequent subsection.

5.3.1 Zonal spin alternation rule

The nature of magnetic exchange interactions and consequently the ground spin state can be visually predicted from the empirical *spin alternation* rule. This rule works perfectly well for the conjugated diradicals wherein the exchange takes place through bond.[247] However, the deviation from the *spin alternation* rule has been reported for sterically hindered cases where the large dihedral angle between the radical moieties breaks the electronic conjugation between π-orbitals and facilitates the direct exchange between the radical centres.[89,248] Such cases usually favors the parallel orientation of electrons residing in the p_z-orbitals of radical centres following the Hund's Rule.[90] Thereby, apparently breaking the *spin alternation* rule and yielding ferromagnetic interactions.

Out of 10 possibilities of di-Blatter diradicals, the nature of magnetic exchange is in agreement with the *spin alternation* rule for six of the isomers. However, the ground spin state of the remaining four isomers, i.e., **a-a, a-b, b-c** and **d-d** is not supported by the *spin alternation* rule. The deviation from *spin alternation* rule is quite obvious for the rotated isomers **a-a** and **d-d** exhibiting large dihedral angles of 71.9° and 53.1° respectively. The observed ferromagnetic exchange in these rotated isomers is in accord to the Hund's rule. But, along with this, the dominant anti-ferromagnetic exchange interactions prevailing in the stable conjugated isomers is also found to be in contrast to the prediction of *spin alternation* rule for **a-b** and **b-c** isomers exhibiting small dihedral angles of 45.0° and 33.9° respectively. Thus, clearly indicating that the di-Blatter diradicals do not strictly follow the emperical *spin alternation* rule. The inadequacy of *spin alternation* rule for the di-Blatter diradicals could be foreseen from the spin density distribution of Blatter's monoradical, shown in Fig. 5.1b, which reveals an α spin density over the two consecutive N2 and N3 atoms. This is in complete contrast to the assumption of *spin alternation* rule where alternate signs of spin density are expected at the consecutive atoms. Thus, clearly revealing that the di-Blatter diradical exhibiting multiple spin centres forbids the simplest *spin alternation* rule.

As an alternative solution, we propose a modified version of *spin alternation* rule, called here as *zonal spin alternation* rule to correctly predict the nature of exchange interactions in such diradicals. The proposal of *zonal spin alternation* rule is based on the

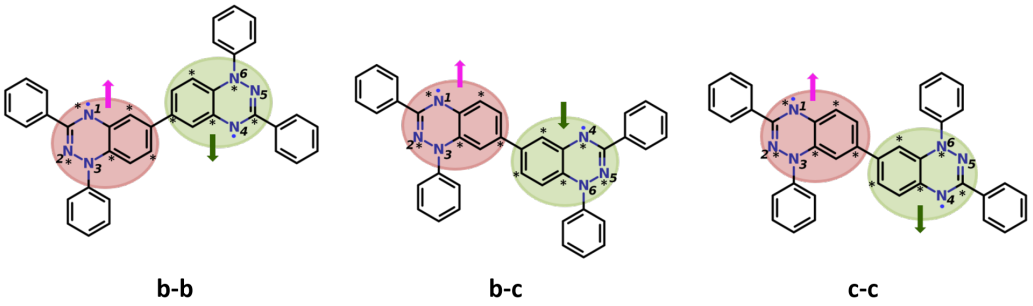

Figure 5.3: Three most stable and conjugated isomers of di-Blatter diradical, **b-b, b-c** and **c-c**.

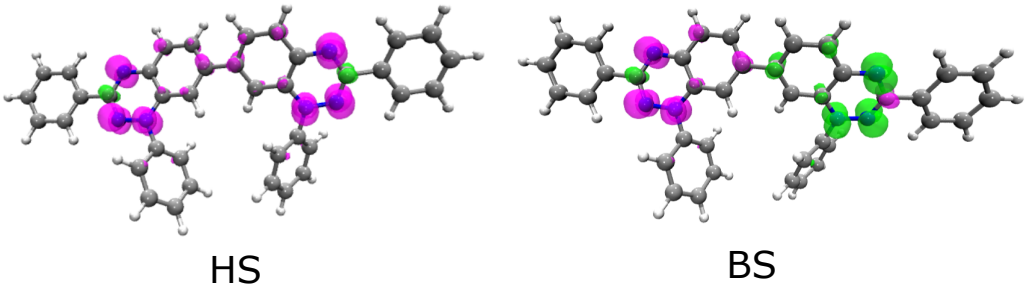

Figure 5.4: Spin-density distribution for diradical **c – c** in high-spin (HS) and broken-symmetry (BS) state. The α and β spins are shown in pink and yellow colours respectively with isovalue of 1×10^{-3} $\mu_B/\text{Å}^3$. All the six N-atoms exhibits approximate 0.23 μ_B spin moment in both HS and BS state with the sign reversal in BS state.

consideration of spatial zones exhibiting similar spin density on the constituent atoms. The contribution of individual atomic centres bearing alternate spin density in accord to *spin alternation* rule has been replaced by zones in *zonal spin alternation* rule. In Blatter's radical, all the atoms of the triazinyl and fused benzene ring exhibits α-spin density, thus triazinyl and fused benzene ring is taken as one complete entity (zone) bearing α-spin density and afterwards standard spin alternation rule is applied on individual atomic centres. The demonstration of *zonal spin alternation* is illustrated in Fig. 5.3 for the three most stable and conjugated isomers, **b-b, b-c** and **c-c**, wherein the triazinyl and fused benzene ring of Blatter's radical is considered as one complete entity with positive/negative spin-density denoted by pink/green circles. The star-nonstar convention over the atomic centres depicts the notation of the *spin alternation* and the similar *Ovchinnikov's* rules. This *zonal spin alternation* rule works perfectly well for the conjugated isomers of di-Blatter diradical as well as for reported Blatter's based diradicals.[233,234,244]

5.3.2 Multiple Pair-wise Exchange Interactions

To elucidate the origin of dominant anti-ferromagnetic exchange in stable isomers of di-Blatter diradical, we calculated the individual pair-wise exchange interactions between

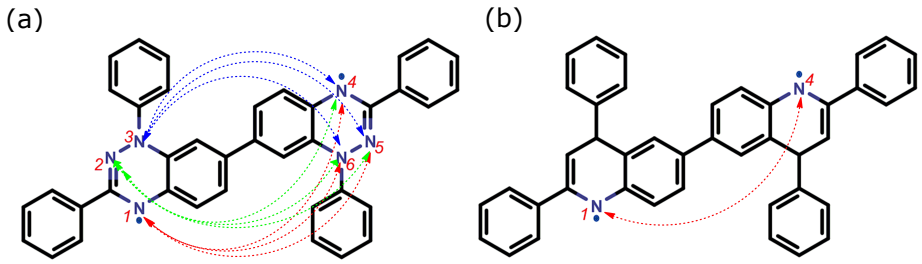

Figure 5.5: **(a)**Different possible interactions in isomer **c-c** ($2J_{Nx-Ny}$ (x= 1,2,3 and y=4,5,6)). The interaction of N1, N2, N3 with N4-N6 is denoted by *red, green* and *blue* color respectively, **(b)** Diradical $\mathbf{cc_1}$ to compute the individual exchange interaction between N1 and N4 ($2J'_{N1-N4}$).

specific N-atoms. The spin density distribution of **c-c** isomer, illustrated in Fig. 5.4, reveals the existence of multiple spin centres in both singlet and triplet state. This scenario is in complete contrast with the much cultivated systems with only two magnetic centres and with only one magnetic exchange pathway. However, in di-Blatter diradical, due to strongly localized fractional magnetic moments that behave as independent micro-magnetic centres, there are total nine different possible pair-wise exchange interactions (i.e. $2J_{N1-N4}$, $2J_{N1-N5}$, $2J_{N1-N6}$, $2J_{N2-N4}$, $2J_{N2-N5}$, $2J_{N2-N6}$, $2J_{N3-N4}$, $2J_{N3-N5}$, $2J_{N3-N6}$ as shown in Fig. 5.5a).

In order to have a proper description of exchange coupling in di-Blatter diradical with multiple magnetic centres, the exchange coupling constants between specific N-pairs are estimated while keeping all other paramagnetic N-atoms magnetically inactive by replacing N-atoms with isoelectronic CH-units in the triazinyl rings. For example, to determine exchange interactions between N1 and N4 i.e. $\mathbf{2}J_{\mathbf{N1-N4}}$ in **c-c** isomer, all the other N-atoms except N1 and N4 are replaced by CH-units as shown in Fig. 5.5b (denoted as $\mathbf{cc_1}$) and the obtained coupling constant is denoted by $\mathbf{2}J'_{\mathbf{N1-N4}}$. As expected, the replacement of N-atoms by CH-units increases the spin density on more electronegative N1 and N4 atoms of diradical $\mathbf{cc_1}$ which results in overestimated exchange, i.e. $\mathbf{2}J'_{\mathbf{N1-N4}}$. Thus, in a refined treatment, the exact exchange between N1 and N4, $\mathbf{2}J_{\mathbf{N1-N4}}$, is obtained by augmentation of the obtained $\mathbf{2}J'_{\mathbf{N1-N4}}$ with the ratio of spin densities deduced from diradical **c-c** and $\mathbf{cc_1}$ respectively. The values of $\mathbf{2}J_{\mathbf{N1-N4}}$ and $\mathbf{2}J'_{\mathbf{N1-N4}}$ are approximated with BS-DFT calculations.

Similarly, the exchange coupling for all the possible 9 magnetic interactions i.e. $2J_{Nx-Ny}$ (x= 1,2,3 and y=4,5,6) shown in Fig. 5.5a are evaluated (Appendix, Sec. C.3). The total $2J$ is obtained as the weighted summation of all the calculated $2J$'s between different magnetic sites. This methodology of calculating individual pairwise magnetic exchange interactions again provides anti-ferromagnetic exchange which is concordant with the predicted nature of exchange interactions using all the DFT and wave

function-based methods. Although among all 9 possibilities, both ferromagnetic and anti-ferromagnetic individual pairwise interactions strictly following the spin alternation rule prevailed between two N-atoms, the magnitude of anti-ferromagnetic interactions was found to be dominating over the ferromagnetic. Thus giving resultant anti-ferromagnetic exchange for isomer **c-c**. Similarly, all the 9 possible exchange interactions resulted in an anti-ferromagnetic exchange in both the other isomers.

5.3.3 Switching of Magnetic Exchange Interactions

The detailed analysis of individual pairwise interactions provides clear signatures of a strong anti-ferromagnetic exchange in planar isomers with connecting sites "b" and "c". However, the small ferromagnetic exchange is observed for non-planar sterically hindered isomers with connecting sites "a" and "d" i.e., **a-a, a-d, c-d** and **d-d**. The effect of dihedral angle in controlling the magnetic exchange interactions is well documented in the literature.[249–251]

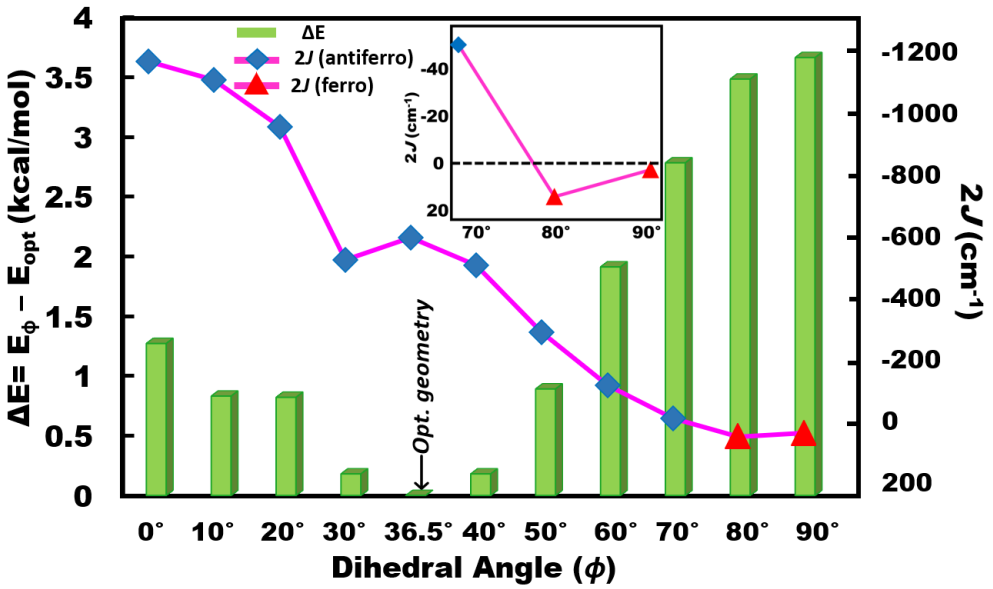

Figure 5.6: Relative energies (ΔE) and variation of exchange coupling constant ($2J$) with dihedral angle between two radical monomers for **c-c** isomer. The green bars represents relative energies calculated at B3LYP/def2-TZVP level. The ferro and anti-ferro exchange is denoted by red triangles and blue diamonds respectively over pink curve.

To validate whether the weak ferromagnetic exchange interaction in the sterically hindered isomers is indeed a direct effect of dihedral angle, we computed the exchange interactions for **c-c** isomer by constraining the dihedral angle (ϕ) between two monomeric units and further varying ϕ from 0 to 90°. The variation of $2J$ with dihe-

dral angle, illustrated in Fig. 5.6 by a pink curve, clearly reveals that the planar geometry with small dihedral angles (including the optimized one at 36.5°) favors anti-ferromagnetic exchange. However, on approaching the orthogonal orientation at ~80°, the nature of the exchange between two radical monomers switches to ferromagnetic (also illustrated in the inset of Fig. 5.6). Along with this, the relative energies, represented by green bars in Fig. 5.6, reveals that sterically hindered geometries with large dihedral angles are least stable. Similar behavior is observed for sterically hindered isomer **a-a** yielding ferromagnetic exchange at optimized dihedral 71.89° while switching to anti-ferromagnetic exchange on constraining the dihedral to 50° (data is provided in Appendix, Sec. C.4).

Thus, as revealed from multiple pair-wise exchange interactions, due to co-existing multiple micro-magnetic centres, anti-ferromagnetic interactions are much dominating in di-Blatter diradicals. However, switching to weak ferromagnetic exchange in strained isomers as well as in rotated configurations indicates that one can obtain ferromagnetic exchange in the super-stable diradicals by tuning the dihedral angle.

5.4 Conclusions

The magnetic exchange interactions are investigated for all the possible isomers of di-Blatter diradical adopting various density as well as wave function-based multi-configurational methods. It reveals coupling the two Blatter's radicals via fused benzene ring yield an anti-ferromagnetic exchange in their stable conjugated configurations. A close agreement with the experimental observations are obtained using traditional DFT based broken symmetry methods, which further improves by employing CBS-DFT. It has been realized that the minimal CAS space accounting two unpaired electrons in two magnetic orbitals, when considered along with dynamical correlations, i.e., CASSCF(2,2)-NEVPT2, provides a reasonable choice to compute exchange interaction in di-Blatter diradicals.

Further, due to α-spin density on all the three N-atoms of Blatter's radical, it forbids the simplest *spin alternation* rule. However, the nature of magnetic exchange interactions in all the Blatter's based conjugated diradicals can be explained accurately by the proposed *zonal spin alternation* rule. Due to the existence of multiple spin centres, di-Blatter diradicals exhibits numerous exchange pathways. In the conjugated stable isomers, the dominating micro-magnetic exchange interactions dictate the magnetic properties of the diradical i.e. anti-ferromagnetic interactions. However, in certain strained isomers as well as in rotated configurations the exchange interactions switch from anti-ferro to weak ferromagnetic interactions. Thus, in-principle switching occurs in a trade-off with molecular stability, hence, synthesizing a ferromagnetically coupled di-Blatter diradical remains as a possibility but a challenging task.

CHAPTER 6

Tuning the magnetic properties of diamagnetic di-Blatter's zwitterion to antiferro- and ferromagnetically coupled diradicals

6.1 Introduction

The singlet diradicaloids, that is, the molecules with partial singlet diradical nature in their ground state are expected to have unique structure with interesting electronic, optical and magnetic properties. But the major challenging part is their structural instability and synthetic difficulties. However, after the pioneering reports of carbon-centered diradicaloids, namely Thiele's hydrocarbons in 1904[111] and Tschitschibabin's hydrocarbon in 1907,[112] the research on this class of compounds has been unrolled widely.[113–119] Following this, a number of diradicals based on stable known radicals like nitronyl nitroxide, imino nitroxide, verdazyl, oxoverdazyl, Blatter's, etc. have been synthesized enormously.[83,92,99–103,252–255]

Tetraphenylhexaazaanthracene (TPHA), the earliest compound containing Blatter's radical moiety, was synthesized by Hutchison et al. with the possibility of obtaining stable heteroatomic ferromagnetic diradical with m-phenylene as coupler.[256] However, contrary to the expectations, it was found to exist as exceptionally stable zwitterionic system with a closed shell ground-state possessing diamagnetic behaviour that undergoes photo-induced intramolecular electron transfer to form a radical pair (Figure 6.1). This molecule is known to exhibit large singlet-triplet energy difference (ΔE_{CSS-T}) of

-20.1 kcal/mol and overcome its 16π potential antiaromaticity by sacrificing the aromaticity of the central fused benzene ring and partitioning itself into 10π-anionic and 6π-cationic sub-units which are structurally bridged by σ-bonds but are not conjugated electronically. Further, efforts have been made to reduce this veritable energy barrier (ΔE_{CSS-T}) but the triplet ground state has not been achieved so far.[257] The two analogous isomers of TPHA possessing closed-shell ground state have been isolated and identified as minor side products by Constantinides et al.[258] Haas et al. rationalised the existence of these zwitterions due to electron transfer from donor to acceptor sub-units. The transfer is possible only if the donor has low ionization potential and the acceptor has high electron affinity.[259] Further, another molecule, tetraphenylhexaazaacridine (TPH-acridine) was synthesized by Langer et al. which was observed to be weakly antiaromatic and highly zwitterionic similar to TPHA.[260] Braunstein et al. also observed the partitioning of 12π electrons into two 6π sub-units which are not electronically conjugated to form zwitterionic benzoquinonemonoimine.[261]

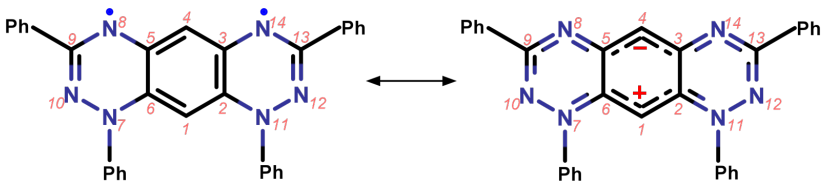

Figure 6.1: Resonating structures of TPHA indicating resonance between the photoexcited diradical and the zwitterionic ground state forms.

Since, polyacenes are known to show inherent property of increase in the diradical character with the increase in the number of fused benzene rings i.e. their length, which can facilitate the enhanced spin-spin coupling between the radical centers.[262,263] Taking advantage of this peculiar property, the quest arises, can we manipulate the well known zwitterionic ground state of TPHA by utilizing polyacene as a coupler to accomplish strong ferromagnetic exchange interactions? Here, we demonstrated an exclusive transition from the zwitterionic closed shell ground state of TPHA to ferromagnetically coupled Blatter's diradicals by modifying the length of the coupler. Several factors including diradical character, extent of spin contamination, alignment of frontier orbitals etc, have been used as guiding principles to mark this spin-state transition with the increasing length of coupler. Apart from this, many experimental and theoretical studies have reported the molecules with zwitterionic ground state where the introduction of EDG and EWG can influence the diradical character and hence, their ground state.[264–266] However, the effect of simultaneous substitution of EDG and EWG i.e. *push-pull* substitution has not been studied so far. Therefore, in this work, we have also explored the effect of *push-pull* substitution with the replacement of hydrogen atoms of

fused benzene ring of TPHA skeleton. Thus, approaching towards the development of molecules with diradicaloid ground state.

6.2 Computational Methods

For all the molecules under study, the geometries were optimized employing the Becke's three-parameter hybrid functional (B3LYP)[162,163] and atom centred polarized triple-zeta (def2-TZVP) basis set in three distinct electronic states, i.e., broken-symmetry open-shell singlet (OSS) state, open-shell triplet (T) state and closed-shell singlet (CSS) state. OSS and T states are optimized within spin-unrestricted formalism, whereas spin-restricted wavefunction is used for CSS state. Resolution of the identity (RI) approximation in conjunction with auxiliary basis set def2/J and chain of spheres (COSX) numerical integration was used to speed up the calculations.[165] The exchange interactions were computed applying BS-DFT method employing Eq. 2.31.[267–269] Another alternative approach to obtain the broken-symmetry solution is the flip-spin method by swapping the alpha and beta orbitals acronymed as BS(SF)-DFT is also used to compute the exchange interactions. In the studied diradicals, the spin contamination is larger for the systems with large number of benzene rings, therefore, the magnetic exchange interactions are calculated by employing spin decontamination procedure proposed by Malrieu and co-workers using Eq. 2.34.[135,136] The exchange interactions are also computed employing collinear version of spin-flip within TD-DFT known as SF-TDDFT method. Since, the BHHLYP functional with 50% HF exchange is known to provide more accurate results within SF-TDDFT approach,[270] therefore, these calculations are performed at BHHLYP/def2-TZVP level. Apart from DFT-based methods, the magnetic exchange interactions were also calculated employing wave-function based complete active space self-consistent field (CASSCF) wherein the $2J$ values are obtained using Eq. 2.23. The active space of 10 electrons in 10 orbitals i.e., CAS(10,10) is selected due to resource limitation for the higher active spaces. This active space is sufficient to provide a qualitative comparison of the magnetic exchange interactions. The dynamical correlations were included using N-electron valence state perturbation theory (NEVPT2) method. Further, to study the density of local aromaticity in polyacene molecules, the HOMA is calculated using Eq. 2.47. We have used different tools for the evaluation of diradical character including the UHF/UNO anlaysis, CASSCF occupation number and Head-Gordon index. The diradical character (y) has been quantified by making use of the unrestricted Hartree-Fock method (UHF) with unrestricted natural orbitals (UNOs) analysis using index proposed by Yamaguchi as[271]

$$y = 1 - \frac{2T}{1 + T^2} \tag{6.1}$$

where T is the overlap integral of orbital pairs given by

$$T = \frac{n_{HONO} - n_{LUNO}}{2}$$

In another method, to quantify the diradical character, the CASSCF(10,10)/def2-TZVP was used to calculate the orbital occupation number of the molecules. The CASSCF orbital occupation numbers are also used to calculate index used to compute effective number of unpaired electrons as proposed by Head-Gordon given by[272]

$$n_{u,nl} = \sum_i (\overline{n}_i^2)(2 - \overline{n}_i)^2 \tag{6.2}$$

where $\overline{n}_i$ is the occupation number of orbitals.

All the calculations are performed in ORCA (version 4.0.1.2) quantum chemical code and the spin-decontaminated calculations of magnetic exchange coupling are performed using LSCF method[273] as implemented in ORCA version 4.2.1. The collinear spin-flip TD-DFT calculations are performed in ORCA version 5.0.1.[138]

6.3 Results and Discussion

6.3.1 Increasing the length of coupler

The two Blatter's radical are coupled to each other through its fused benzene ring, wherein n=1 corresponds to TPHA. Afterwards, one benzene unit is consecutively added in the spacer between the two radical centers upto hexacene (n = 6) as shown in Figure 6.2. All the molecules are optimized in the three electronic states, i.e., closed-

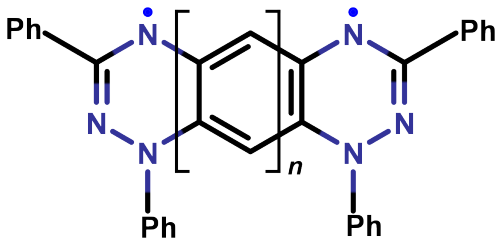

Figure 6.2: Two Blatter radicals coupled through benzene ring. Here, n = 1 to 6, corresponds to number of benzene rings used to couple two radical moieties. The corresponding molecules are aliased as **6.1** to **6.6** depending on the number of benzene rings i.e. **1** corresponds to molecule containing 1 benzene ring.

shell singlet (CSS), broken-symmetry open-shell singlet (OSS) and open-shell triplet (T) states. The DFT optimized energies in all the states are given in Table D.1. The relative energies i.e. ΔE_{X-CSS} (where X = CSS, OSS, T) estimated from the relative energy difference between the DFT optimized energies are shown in Figure 6.3 and are collected in Table D.2. It is observed that the molecule **6.1** preferred the closed-shell singlet as ground state as reported earlier.[256] It is also observed that although the calculation was performed in spin-unrestricted (UKS) case, it was found to reduce to spin-restricted (RKS) solution and almost identical energies with a minute difference of 0.8 meV between the OSS and CSS states were obtained. The different charge distribution schemes, namely Löwdin, Mulliken and Hirshfeld charge distribution also provide the separation of positive and negative parts in the TPHA moiety implying the formation of zwitterion.(Figure D.1) Moreover, the orientation of dipole moment and the electrostatic potential mapped on the electron density surface also envision the molecule to be in the CSS state (Figure D.1). Molecule **6.2** also exhibits a closed shell ground-state with OSS state lying 11.8 meV above the CSS state. However, for molecule **6.3** and **6.4**, larger $\Delta E_{OSS-CSS}$ is observed indicating the instability of the CSS structure i.e. these molecules favour the OSS as the ground state. Further, with larger number of benzene rings i.e. for molecule **6.5** and **6.6**, there is substantial increase in ΔE_{T-CSS} representing the preference of triplet as the ground state.

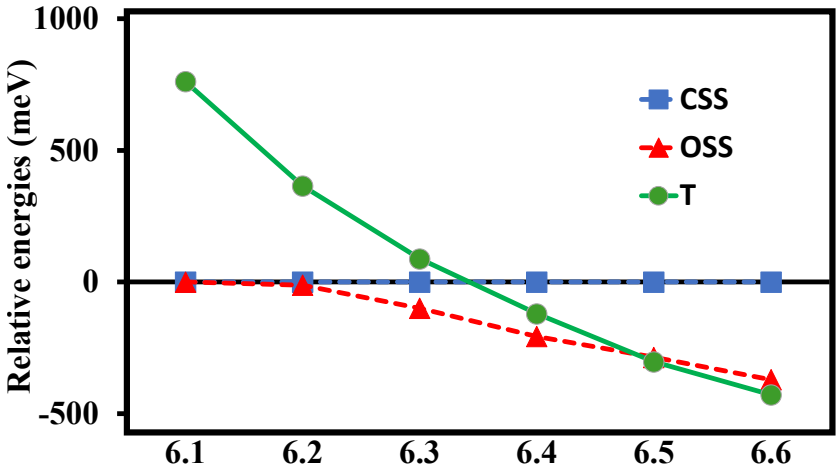

Figure 6.3: Relative energies (meV) of the CSS, OSS and T states (referred to the CSS) of molecule **6.1** to **6.6**.

The spin-squared value i.e. $<S^2>$ has been used to estimate the extent of diradical character in a molecule. The spin contaminations can be determined from the calculated values of $<S^2>$. The $<S^2>$ value is 2.0 for the triplet-state diradical and 0.0 for the pure closed-shell singlet state. However, when the $<S^2>$ value is greater than 0.0, it indicates the contribution from the open-shell configuration, and value of 1.0 indicates the open-

shell singlet state of the molecule.

From the $<S^2>$ values in HS state (Figure 6.4 and Table 6.1), it is observed that the spin contamination for molecules **6.1** to **6.4** are low and the deviations from the expected value of 2.0 is atmost 0.08. However, for molecules **6.5** and **6.6**, the spin contamination is observed to be upto 0.36. However, as illustrated in Figure 6.4 and Table 6.1, the computed $<S^2>$ values in BS state for molecules **6.1-6.4** are found to be significantly less than 1.0. Thus, indicating the pronounced contribution of closed-shell singlet electronic configuration in the singlet diradicals. A value of 0.23 for molecule **6.1** clearly indicates the existence of the molecule in the CSS ground state which agrees well with the predicted state of this molecule. However, as the number of benzene rings i.e. n increases between the two spin-centered Blatter's radicals, the value starts approaching 1.0 indicating the preferential existence of molecule in the diradical configurations. For molecules **6.3** and **6.4**, the $<S^2>$ value is 0.77 and 0.89 which means that they are indeed diradicalized and their ground state is open-shell singlet, however, their degree of diradical character is not as ideal as for pure singlet-state (BS). However, for molecules **6.5** and **6.6**, $<S^2>$ is ~1.0, indicating the attainment of ideal diradical state in these molecules. The reason for the increased spin contamination for larger polyacene couplers is the enhanced degenerate nature of occupied and unoccupied molecular orbitals as n increases (Figure D.2) leading to a smaller HOMO-LUMO energy gap which is observed previously also.[274]

Table 6.1: Computed spin-squared value ($<S^2>$) in HS and BS state for all the molecules and calculated magnetic exchange coupling constants for the diradicals **6.3-6.6**.

Mol.	$<S^2>$		$2J$ **(cm^{-1})**				
	BS-DFT		**BS-DFT**[b]	**BS-DFT**	**SF**[c]	**CAS(10,10)**	**NEVPT2**
	HS	**BS**		**(SD)**	**-TDDFT**		
6.1[a]	2.03	0.23	-	-	-	-	-
6.2[a]	2.03	0.56	-	-	-	-	-
6.3	2.04	0.77	-2774.64	-2231.64	-1637.30	-333.08	-1551.44
6.4	2.08	0.89	-1240.04	-1092.38	-510.40	-58.30	-447.03
6.5	2.21	0.97	328.84	288.80	71.41	22.38	37.10
6.6	2.36	1.03	1797.40	1697.18	361.50	823.03	950.10

[a]These molecules possess zwitterionic GS that behave as diamagnetic species with CSS GS with large ΔE_{CSS-T} (>5000 cm^{-1}).
[b]The results from BS(SF)-DFT are collected in Table D.8.
[c]BHHLYP functional is employed to compute magnetic exchange interactions.

Further, the diradical character of these molecules given in terms of y value is quantified from the occupation numbers of unrestricted natural orbitals obtained from un-

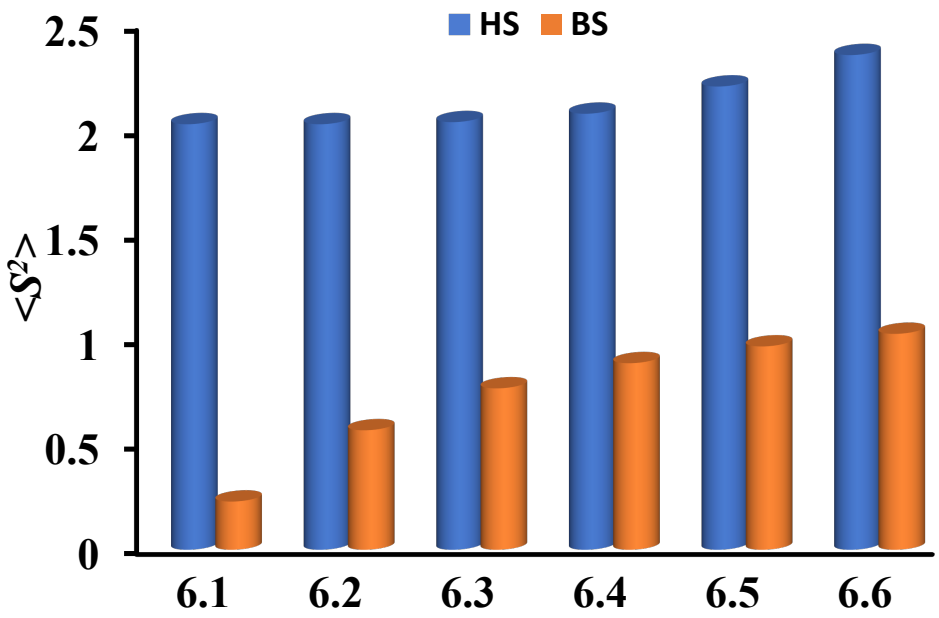

Figure 6.4: Computed $<S^2>$ values in HS and BS state for the molecules **6.1** to **6.6** obtained at UB3LYP/def2-TZVP level.

restricted hartree-fock calculations utilizing Eq. 6.1 (Details are provided in Appendix Sec. D.2.3). The y value for molecule **6.1** is observed to be 0.28 (Table D.3) indicating only 28% diradical character in the molecule. As the number of benzene rings between the radical centers increase, a substantial increase in y value from 0.53 for **6.2** to 0.80 for **6.6** is observed. The increase in the y value clearly indicates the increase in diradical character of the molecules with larger coupler.

Another index for the evaluation of diradical character in a molecule is the occupation number of lowest unoccupied natural orbital (n_{LUNO}) obtained from the CASSCF calculations. The percentage of diradical character can be directly estimated from n_{LUNO} by simply multiplying it with 100. Therefore, we calculated the occupation number of the highest occupied natural orbital (HONO) and lowest unoccupied natural orbital (LUNO) and the percentage of diradical character using the CASSCF(10,10)/def2-TZVP method. For molecule **6.1**, the LUNO occupation number, n_{LUNO}, is observed to be 0.30 indicating that it has only 30% diradical character which further confirms the zwitterionic character of the molecule. As we proceed towards molecule with increasing number of benzene rings, the occupation number of LUNO shows a sequential increase from 0.58 for **6.2** to 0.95 for **6.6** which infers an increase in diradical character from 58% to 95% on going from **6.2** to **6.6** (Table D.4). The significant increase in diradical character from 30% for **6.1** to more than 80% for diradicals **6.3-6.6** unambiguously confirms the evolution of a diradical state with the increasing length of coupler.

The Head-Gordon index ($n_{u,nl}$) value provides a clear picture of the effective number of unpaired electrons in the larger molecules as observed by Orms et al.[275] Therefore, we computed the Head-Gordon index employing Eq. 6.2. The orbitals with partial occupation numbers obtained from CASSCF(10,10) contribute to the $n_{u,nl}$ value and the doubly occupied and unoccupied orbitals have zero contribution. The computed $n_{u,nl}$ value for molecule **6.1** is 0.62 (Table D.5) which reveals that the molecule has no unpaired electrons and hence possess zwitterionic ground state. The molecule **6.2** has an intermediate value of 1.50 indicating partial diradical state for this molecule. For molecules **6.3-6.6**, the value is ~2.0 indicating presence of two unpaired electrons and hence, diradical ground state for these molecules. The diradical indices derived employing different calculation methods are found to be in agreement with each other confirming the extent of diradical character in these molecules.

Further to find out the relationship between the ground-state and the magnetic spin couplings, correlation diagram is plotted between the magnetic exchange coupling constant, $2J$ (cm^{-1}) and the energy gap between the closed-shell singlet and triplet i.e. ΔE_{CSS-T} (kcal/mol) as shown in Figure 6.5a. The degree of correlation is quantified on the basis of correlation coefficient i.e. R^2 which describes the strength of relationship between the two variables. A value of 1.0 and -1.0 indicates strong positive and negative correlations and a value of 0 means there is no correlation between the two variables. A highly linear correlation with correlation coefficient (R^2) of 0.99 is found between $2J$ and ΔE_{CSS-T}. The large negative energy gap and high negative magnetic exchange cou-

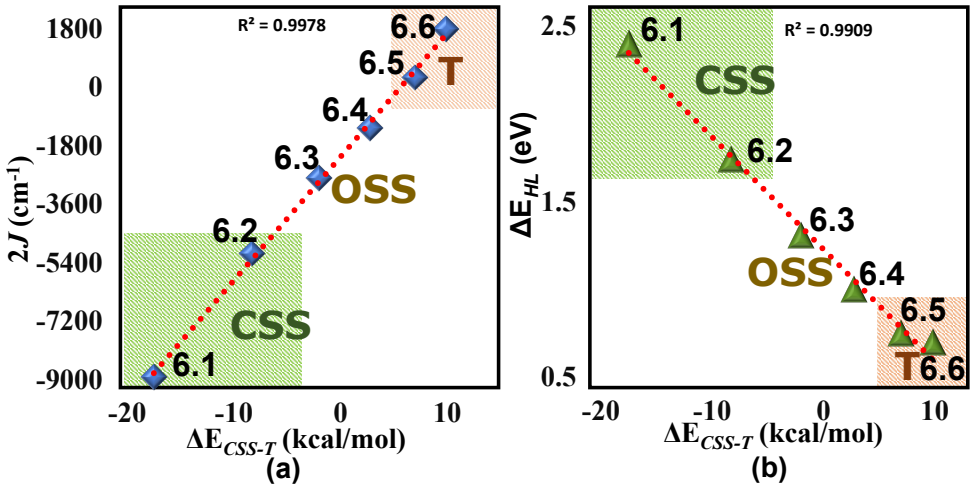

Figure 6.5: Linear correlation diagram (a) between the magnetic exchange coupling constant, $2J$ (cm^{-1}) and the energy gap between the closed-shell singlet and triplet states i.e. ΔE_{CSS-T} (kcal/mol) (b) between HOMO-LUMO gap i.e. ΔE_{HL} (eV) in the closed-shell state and ΔE_{CSS-T} (kcal/mol) for molecules **6.1** to **6.6** with correlation coefficient i.e. R^2 of 0.99.

pling constant ($2J$) are in line with the zwitterionic character of molecules **6.1** and **6.2**. As the energy gap decreases and comes in the range of -5 to 5 kcal/mol i.e. for **6.3** and **6.4**, open shell singlet emerges as the ground state with antiferromagnetic exchange interactions between the two radical centers. However, with energy gap >5 kcal/mol i.e. for molecule **6.5** and **6.6**, ferromagnetic interactions are favoured. The diradical character emerges from the interaction between the singlet and the triplet states.[276] It is observed that if the energy gap between the closed-shell singlet and triplet is high, the configuration interaction between them is negligible and the molecule has preferential closed-shell ground state. However, if the singlet-triplet energy gap is small, they have strong interactions between them and hence, the molecule prefers the open-shell singlet or triplet as ground state.

To realize relationship between closed shell singlet-triplet energy gap i.e. ΔE_{CSS-T} and HOMO-LUMO energy gap i.e. ΔE_{HL}, we plotted the correlation diagram between the two. The closed shell singlet-triplet energy gap is observed to be in close alliance with the HOMO-LUMO gap that is observed from the linear correlation diagram with high correlation coefficient (R^2) of 0.99 as shown in Figure 6.5b. Thus, to realize the extent of diradical character in these systems and hence, their ground spin state, it becomes essential to further investigate the HOMO-LUMO gap. The computed HOMO-LUMO gap i.e. ΔE_{HL} (in eV) is observed to decrease smoothly from 1.25 to 0.39 eV on going from **6.3** to **6.6**. It is found to be much smaller in the diradicals **6.3-6.6** i.e., in the range 0.39-1.25 eV as compared to the zwitterions **6.1**(2.40) and **6.2**(1.74) (Figure 6.6 and Table D.6). The large energy difference between the two orbitals makes the molecule to prefer the closed-shell configuration. However, small energy gap between the two orbitals makes them energetically degenerate and hence, open shell configuration can be easily achieved by promoting an electron from HOMO into the LUMO, leading to the preference of open-shell configuration in the molecule. SOMOs play a significant role in the magnetic interaction owing to itinerant exchange. It is already reported that low SOMO-SOMO gap or nearly degenerate SOMOs foster strong magnetic exchange interactions.[265,277,278] From Figure 6.6b, it has been observed that the energy difference between the two SOMOs i.e. ΔE_{SS} is smaller for diradicals **6.3-6.6** in comparison with the larger value for the zwitterion **6.1** and **6.2**. Consequently, the nearly degenerate SOMOs prefer open shell configurations in comparison to the closed-shell state for non-degenerate SOMOs.

The computed magnetic exchange interactions for the diradicals **6.3-6.6** from different methods i.e. BS-DFT, spin-decontaminated (S.D.) BS-DFT, SF-TDDFT and wavefunction based CASSCF and CASSCF-NEVPT2 are collected in Figure 6.7 and Table 6.1, D.7, D.9, D.11, D.12. The BS(SF)-DFT results are also tabulated in Table D.8. The traditional BS-DFT employing the hybrid B3LYP functional results in intramolecular

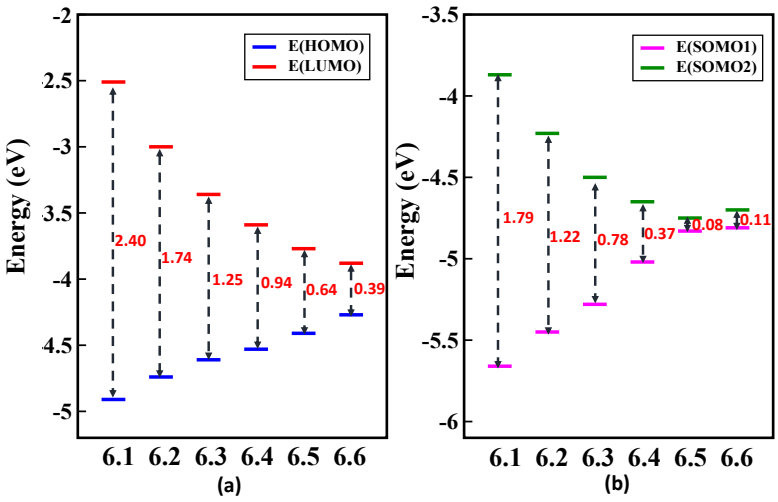

Figure 6.6: Energy difference (eV) between (a) HOMO and LUMO in the closed shell singlet state. (b) SOMO1 and SOMO2 in the triplet state. The blue and red lines represent HOMO and LUMO respectively and pink and green lines represent SOMO1 and SOMO2 respectively.

antiferromagnetic exchange interactions for diradicals **6.3** and **6.4** whereas diradicals **6.5** and **6.6** are characterized by ferromagnetic spin-spin coupling characteristics. A switching from open-shell singlet to triplet configuration is observed while moving from molecule **6.4** to **6.5**. Additionally, SF-TDDFT yields results which agrees well with that obtained from BS-DFT. However, due to large spin-contamination in these molecules, the exchange interactions are also calculated employing the spin-decontamination procedure.[135] The different contributions, as well as the total magnetic exchange coupling, are tabulated in Table D.11 and 6.1. The values obtained from the spin-decontaminated procedure also result in antiferromagnetic exchange interactions for molecules **6.3** and **6.4** and ferromagnetic coupling for molecules **6.5** and **6.6**, however, with a small decrease in the magnitude of exchange interactions.

Since, DFT functionals tend to produce overestimated magnitude of couplings due to exceeding spin-delocalization in the highly conjugated systems,[279,280] it becomes mandatory to employ symmetry-adapted wave function theory based multiconfigurational methods i.e. CASSCF and CASSCF-NEVPT2 to compute the exchange interactions in these diradicals. We have selected CASSCF(10,10) active space, incorporating 10 active electrons in 10 active orbitals, for the estimation of the exchange interactions and the dynamical correlations are incorporated employing NEVPT2. It is observed that for all the diradicals CASSCF(10,10) and CASSCF(10,10)-NEVPT2 results in similar characteristics of exchange interactions i.e. antiferromagnetic for diradicals **6.3** and **6.4** and ferromagnetic coupling for **6.5** and **6.6**. Although the sign of exchange interactions is consistently reproduced by the wave-function based methods, the expected lowering

in the magnitude of antiferromagnetic and ferromagnetic exchange coupling is observed from WFT based methods than that obtained from BS-DFT for all the diradicals. Thus, all the methods provide the qualitative information regarding the existence of antiferromagnetic coupling in diradicals **6.3** and **6.4** and transition to ferromagnetic exchange interactions for diradicals **6.5** and **6.6**. However, it is difficult to rely on the quantitative prediction of numerical values of $2J$ owing to the well-known spin-contamination errors in DFT which further intensify with increasing length of coupler. On the other hand, WF based multi-reference methods demand for the resource extensive larger active space which manifolds with increasing length.

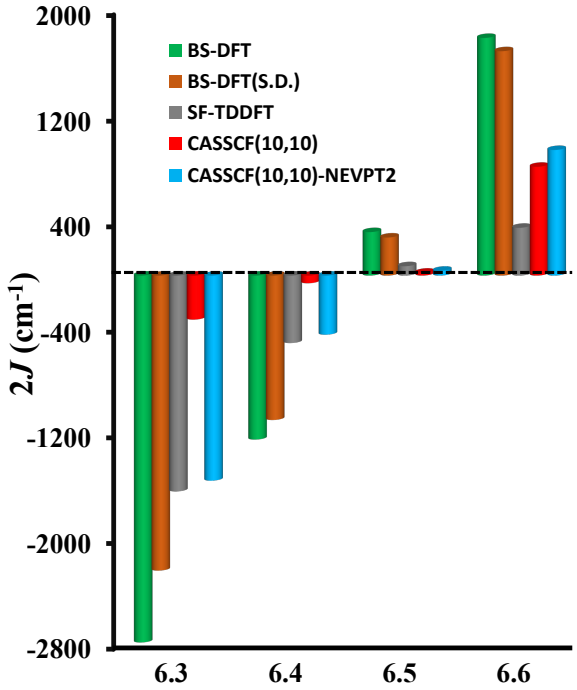

Figure 6.7: Computed magnetic exchange interactions obtained with DFT based BS-DFT, spin-decontaminated procedure in BS-DFT (S.D.) and SF-TDDFT and wave-function based CASSCF and CASSCF-NEVPT2 methods for the molecules **6.3-6.6**. Molecules **6.3** and **6.4** are stabilized in open-shell singlet ground state with antiferromagnetic interactions and **6.5** and **6.6** exhibits ferromagnetic exchange with triplet ground state.

Tetraphenylhexaazaanthracene (TPHA), i.e. molecule **6.1** contains the m-phenylene coupler and is expected to be a ferromagnetic diradical. However, to overcome its potential antiaromaticity, it exists in the zwitterionic configuration with two electrons occupying the same orbital and is observed to be diamagnetic in nature with large HOMO-LUMO gap. However, as the number of benzene rings between the two radical centers i.e. the distance between the two radical centers increases, energy gap between HOMO and LUMO decreases. With the decrease in the energy gap between HOMO

and LUMO, the electron from HOMO will transfer to the LUMO in the spin-conserved (without flipping) environment. It leads to two electrons in two different orbitals embarking open-shell singlet configuration for the molecules **6.3** and **6.4**. With further increase in the number of rings, the HOMO-LUMO gap decreases more, orienting the two electrons parallel to each other instigating the intrinsic behavior of m-phenylene coupler to give ferromagnetic interactions between the two radical centers. Hence, for **6.5** and **6.6**, ferromagnetic coupling is observed with very small energy gap between HOMO and LUMO. This transformation from closed shell for molecules **6.1** and **6.2** to open shell configuration **6.3-6.6** is well correlated to the dissociation of bond in a simple homodinuclear molecule by Nakano.[281] The strategy of enhancing the diradical character by increasing the spacing between the radical centers has been successfully applied by Rottschafer et al. They have observed a decrease in the singlet-triplet energy gap with increasing the length of spacer between the radical centers.[282]

6.3.2 Substituent effect

In order to investigate the simultaneous effect of different electron-withdrawing (EWG) and electron-donating groups (EDG) i.e. *push-pull* substitution on the the ground-spin state of TPHA, we investigated a series of model systems (shown in Figure 6.8) sharing a common skeleton of TPHA with the substitution of hydrogens of the central benzene ring with different EWG and EDG. With the aim of designing molecules with larger diradical character and hence diradicaloid or triplet ground state, a variety of substituents with wide range of inductive and resonating effects are employed. The designing strategy is to simultaneously push the electrons by substituting EDG (in place of H) in the already electron rich negative part and to pull the electrons by substituting EWG from the already electron deficient positive part of the molecule (Figure 6.8).

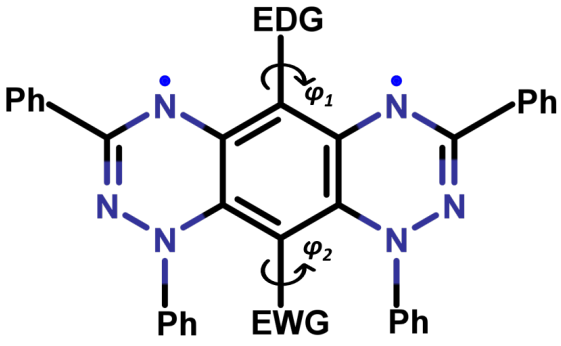

Molecule	EDG	EWG
6.1	H	H
6.1a	NMe_2	CF_3
6.1b	NMe_2	CN
6.1c	NMe_2	NO_2
6.1d	NH_2	CF_3
6.1e	NH_2	CN
6.1f	NH_2	NO_2
6.1g	OH	CF_3
6.1h	OH	CN
6.1i	OH	NO_2

Figure 6.8: Modeled diradicals designed with the simultaneous substitution of electron donating group (EDG) and electron withdrawing group (EWG) on the parent TPHA i.e. molecule **6.1** and are aliased as **6.1a** to **6.1i**.

The electron-donating substituents employed are NMe_2, NH_2 and OH and electron-withdrawing substituents are CF_3, CN and NO_2. The substituents NMe_2, NH_2 and OH have positive resonating effect (+R) implying electron-donating nature whereas CN and NO_2 possess negative resonating effect (-R) leading to electron-withdrawing nature and CF_3 owing to negative inductive effect (-I) also shows electron-withdrawing character. Further, the strength of donation or removal of electron density of different substituents is provided by Hammett constant (σ_{para})[283] which signifies the net influence of resonating and inductive effects. The negative and positive sign of σ_{para} signifies electron-donating and electron-withdrawing nature of substituent respectively and its magnitude represents the strength of donation or removal of electron density. From the Hammett constants provided in Table D.13, it is observed that NMe_2, NH_2 and OH have negative σ_{para} implying electron-donating character with the strength in the order NMe_2 (-0.83) > NH_2 (-0.66) > OH (-0.37) whereas NO_2, CN and CF_3 possess positive value indicating electron-withdrawing nature of substituents with NO_2 (0.78) being strongest followed by CN (0.66) and CF_3 (0.54).

Further, based on attached EDG, the 9 modeled molecules (shown in Figure 6.8) are classified into three distinct series A, B and C containing NMe_2, NH_2 and OH respectively as EDG. EWGs are varied from CF_3, CN and NO_2 in each series respectively. Accordingly, molecules **6.1a**, **6.1b** and **6.1c** belongs to series A, series B contains **6.1d**, **6.1e** and **6.1f**, and series C comprises of **6.1g**, **6.1h** and **6.1i**.

The investigation of $<S^2>$ values in HS state (Table 6.2) reveals that the spin-contaminations of the triplet states are low and are atmost 0.04. However, the $<S^2>$ values in BS state show a wide range of spin-contamination with value of $<S^2>$ ranging from 0.23 to 0.62. Since, the $<S^2>_{BS}$ values render the extent of diradical character wherein the large $<S^2>_{BS}$ values approaching towards 1.0 (<1.0) signifies the diradicaloid ground state of the molecules. Appreciably, all the substituted systems are found to possess larger $<S^2>_{BS}$ values than the parent molecule **6.1**. To rationalize the observed increase in diradical character upon substitution, we propose that the EDG pushes its electrons to the central fused benzene ring and simultaneously the EWG pulls the electrons from the benzene ring resulting in a *push-pull* mechanism leading to a resonating structure **Y** (Figure 6.9). We believe that with this resonating structure, the molecule will no longer be able to partition its 16π electrons into 10π-negative and 6π-positive parts and thus displays a transition from zwitterionic TPHA to a diradicaloid state. Apart from this, the calculated HOMA value of the central benzene ring (Table 6.2) is in the range of 0.47-0.61, indicating lesser π-orbital overlap within the ring. Although the aromaticity of the central ring is still sacrificed which can be quantified from the smaller HOMA values, but the loss of aromaticity of the ring is not due to partitioning into negative and positive components but it is because of existence of resonance in

Table 6.2: The $<S^2>$ values in HS and BS state for the molecules **6.1a-6.1i** obtained with different substituents and the HOMA values of the central benzene ring of all the molecules.

Molecule	EDG	EWG	$<S^2>_{HS}$	$<S^2>_{BS}$	HOMA
6.1	H	H	2.03	0.23	0.58
6.1a	NMe_2	CF_3	2.04	0.49	0.48
6.1b	NMe_2	CN	2.04	0.48	0.49
6.1c	NMe_2	NO_2	2.04	0.62	0.47
6.1d	NH_2	CF_3	2.04	0.57	0.61
6.1e	NH_2	CN	2.04	0.58	0.57
6.1f	NH_2	NO_2	2.04	0.58	0.62
6.1g	OH	CF_3	2.04	0.46	0.56
6.1h	OH	CN	2.04	0.39	0.64
6.1i	OH	NO_2	2.04	0.47	0.57

these molecules as structures **X** and **Y** (Figure 6.9). Due to these resonating structures, the two unpaired electrons will be localized on the radical centers (triazinyl rings) instead of taking part in the partitioning into two components. Eventually, the increase in the molecular diradical character and the diradicaloid ground state will be encountered.

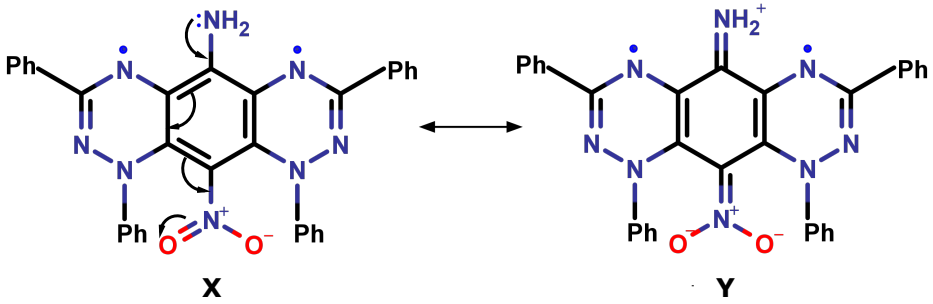

Figure 6.9: The resonance in the substituted molecules with the resonating structures **X** and **Y**. Here, resonating structures of molecule **6.1c** is shown.

Further, in all the three series, the molecule containing NO_2 as EWG i.e. **6.1c**, **6.1f** and **6.1i** displays larger $<S^2>_{BS}$ among their respective series and thus possess larger diradical character. This is due to the strongest electron-removing tendency of the NO_2 substituent among the three EWGs considered as quantified by its Hammett constant. Among these molecules, **6.1c** comes as an optimum combination that provides the largest value which is due to strongest electron-donating ability of NMe_2 followed by NH_2 and OH which is in line to their electron-donation strength. However, molecules **6.1b**, **6.1e** and **6.1h** containing CN as EWG yields larger value with NH_2 followed by NMe_2 as EDG which is in contrast to the electron donating strength of the substituent. The source of this ambiguity is found in the interplanar angles (ϕ_1 and ϕ_2 shown in

Figure 6.8) which the EDG and EWG make with the benzene ring (Table D.14). It has been observed that in **6.1e**, the EDG is perfectly planar to the benzene ring yielding interplanar angle ~ 120° whereas **6.1b** shows a minute deviation of 1.5° from the plane leading to slightly less overlap of 2p orbitals of N atom of EDG and C atom of benzene ring as compared to **6.1e** where the perfect planarity yields appropriate overlapping of the orbitals. It leads to the facile donation of lone pair of nitrogen of EDG to the benzene ring through resonance and hence, makes **Y** the dominant resonating structure. Thus, the source of the mismatch of the electron-donating nature of substituent can be attributed to the electronic and atomic structure of the molecules. The same argument also applies to explain the result observed with CF_3 as EDG where NH_2(**6.1d**) shows larger value than NMe_2(**6.1a**) due to ideally planar angle in **6.1d** than **6.1a** with slight distortion of ~ 1.5°.

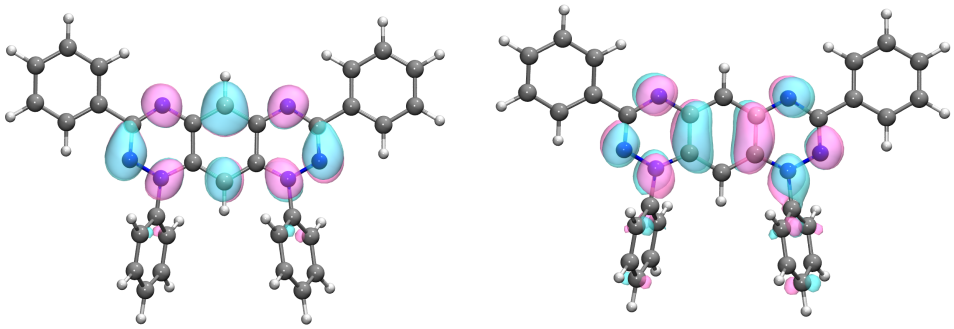

Figure 6.10: Molecular orbitals (HOMO and LUMO) of molecule **6.1** i.e. TPHA in the closed-shell singlet state at B3LYP/def2-TZVP level at an isovalue of 0.03.

Further, the inspection of the frontier molecular orbitals of TPHA reveals that HOMO of TPHA exhibits large atomic coefficient at the centre of 10π-anionic part and LUMO shows a node at the centre of 6π-cationic part (Figure 6.10). Similar spatial features of frontier orbitals were also observed previously for bis(1,2,3-dithiazoles).[264] From this peculiar distribution of frontier orbitals, one can infer that the introduction of EDG will donate electrons to the electron rich position and will raise the energy level of HOMO. Similarly, introduction of EWG at positive position will remove electrons from the electron deficient position and will lower the energy level of LUMO. Therefore, the simultaneous substitution of EDG and EWG results in the raising of HOMO level and lowering of LUMO level and consequently, brings down the gap between HOMO and LUMO (ΔE_{HL}) leading to preferential diradicaloid ground state of the molecules. Figure 6.11 depicts the ΔE_{HL} of the molecules with different EDG and EWG and the parent molecule **6.1**. It has been identified that for **6.1**, the ΔE_{HL} is highest with least diradical character and for all other molecules, ΔE_{HL} is smaller than that for **6.1**. This proposes an inverse relation between the ΔE_{HL} and the diradical character. Among the three se-

ries, ΔE_{HL} is least for the molecules containing NO_2 as EWG i.e. **6.1c, 6.1f** and **6.1i** providing the reason for the large diradical character in these molecules. The smallest ΔE_{HL} for molecule **6.1c** also unveils the observation of largest diradical character in this molecule. In series A, molecules **6.1a** and **6.1b** bear similar ΔE_{HL} supporting comparable diradical character. In series B, molecules **6.1d** and **6.1e** possess equivalent ΔE_{HL} matching the corresonding diradical character. Among series C, molecule **6.1h** with smallest diradical character bears largest ΔE_{HL}.

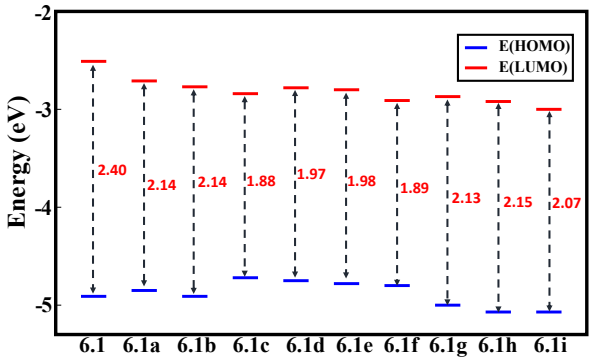

Figure 6.11: Energy difference (eV) between HOMO and LUMO in the structures optimized in open-shell singlet state for the molecules with different EDG and EWG.

Furthermore, while exploring the effect of different *push-pull* substitutions on the diradical character, we encountered three molecules (Figure D.3) that exhibit pure diradical ground state. These are designed by positioning O^- as EDG and CF_3, CN and NO_2 as EWG and acronymed as O-CF_3, O-CN and O-NO_2 respectively. For all the three diradicals, the $<S^2>_{BS}$ values are ~1.0 (Table D.15) manifesting ideal diradical character in these molecules. Moreover, the LUNO occupation number from CASSCF (10,10) i.e. n_{LUNO} is ~0.87 (Table D.17) signifying 87% diradical character in all the molecules. The HOMA values calculated for the central benzene ring of these diradicals is ~0.20 (Table D.18) which is much smaller than those of molecules **6.1a-6.1i** revealing the loss of aromaticity of the ring is much more pronounced in these diradicals. This imparts that the resonating structure **Y** (Figure 6.9) is more significant than **X** which is also observed from the C-O bond length in the three radicals which acquires double bond character with bond length of 1.23 Å. The magnetic exchange interactions are calculated from DFT-based methods i.e., BS-DFT and SF-TDDFT as well as WFT based methods i.e., CASSCF (10,10) and CASSCF (10,10)-NEVPT2 (Table D.15, D.16, D.19). From all the aforementioned methods, strong ferromagnetic exchange interactions are calculated for all the three diradicals owing to triplet ground state as illustrated in Figure 6.12.

Thus, the increase of diradical character and in consequence, attainment of diradicaloid or triplet ground state, upon simultaneous substitution of EDG and EWG comes

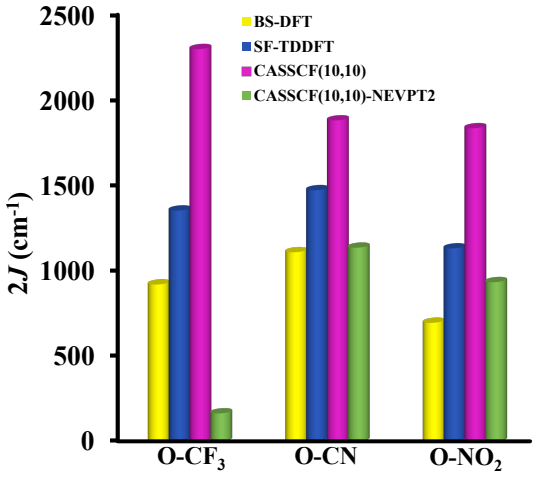

Figure 6.12: Computed magnetic exchange interactions in three diradicals i.e. O-CF_3, O-CN and O-NO_2.

up as a beneficial implementation for the designing of molecules with diradicalized ground state advancing a step closer towards superior magnetic materials.

6.4 Conclusions

With the aim of instigating diradical character in the well known zwitterionic ground-state of tetraphenylhexaazaanthracene i.e. TPHA (here, molecule **6.1**), the molecule encompassing two Blatter's radical moieties, two distinct strategies have been employed. In the first approach, the length of the coupler between the two radical centers is increased upto hexaacene. It has been identified that with increasing the length of the coupler, the diradical character in a molecule is increased. A transition from closed-shell singlet (molecule **6.1** and **6.2**) to open-shell singlet (**6.3** and **6.4**) and subsequently to triplet state for **6.5** and **6.6** is observed with the enlargement of length of the coupler. For assessment of diradical character, different indexes, DFT based spin squared-value ($<S^2>_{BS}$), diradical character, *y* value proposed by Yamaguchi and WFT based LUNO occupation number (n_{LUNO}) and index proposed by Head-Gordon for calculation of effective number of unpaired electrons, are implemented which complements well with each other. All of them reveal increase in diradical character with increase in the number of benzene rings. The computed exchange interactions provide a qualitative picture of transition from open-shell singlet for diradicals **6.3** and **6.4** to triplet state for diradicals **6.5** and **6.6**. A good correlation is observed between magnetic exchange coupling constants and the energy gap between the closed-shell singlet and triplet state.

Another alternative approach is the substitution of electron donating group (EDG) and electron withdrawing group (EWG) simultaneously (*push-pull* substitution) at the

anionic and cationic fragments of the zwitterionic molecule **6.1**. It has been discovered that this strategic substitution on molecules with zwitterionic ground-state proposes a plausible way to alter the diradical character of the molecule leading to the diradicaloid ground-state. Furthermore, three molecules are observed which exhibits strong intramolecular ferromagnetic exchange interactions owing to triplet ground state. This work provides a new perspective of designing molecules based on Blatter's radical with ferromagnetic ground state.

CHAPTER 7

Conclusions and Future Perspectives

The fundamental understanding of the evolution of magnetic properties in magnetic molecules is essential for obtaining these exotic molecules with retention of magnetization at room temperature. First-principle quantum chemical calculations stand uniquely poised in designing these exotic molecules and presents an essential source of rationalization for the observed properties. This thesis seeks to understand the magnetic anisotropy of transition metal based organometallic complexes and the isotropic ferromagnetic exchange interactions in metal-free organic molecular magnets from a computational perspective. To accomplish these objectives, the entire work is presented in four chapters where the first two chapters focus on the investigation of magnetic anisotropy of organometallic single-molecule magnets. The latter two chapters deal with the understanding of isotropic ferromagnetic exchange interactions in metal-free organic molecular magnets.

Transition metal complexes with high axial symmetry warrant unquenched first-order orbital angular momentum and large spin-orbit coupling with potential in quantum computing and high-density data storage devices. In this framework, we have studied axially symmetric complexes in the presence and absence of equatorial ligands to study the effect of geometry on magnetic anisotropy.

- In *Chapter 3*, we have modeled fourteen trigonal bipyramidal Fe(III) complexes by varying the axial ligands with Group XV elements and equatorial ligands with the halides. The DFT and multi-reference *ab initio* electronic structure methods are employed to probe the ground-spin state, spin-crossover properties, and zero-field splitting parameters of the complexes. The zero-field splitting is observed to increase with the softness of the ligand at the axial position i.e., from N to As.

However, for equatorial ligands, the largest value is observed with Br followed by I and Cl. As a generalization, it has been observed that complexes with hard ligands i.e., N at axial and F at equatorial positions are stabilized in the high-spin state with minimal zero-field splitting and are not a good choice as ligands for Fe (III) based SMMs. Moreover, a few of the complexes are identified with small Gibbs free energy difference between the intermediate and high-spin ground state indicating plausible candidates for spin-crossover complexes.

- In *Chapter 4*, five complexes containing only axial ligands i.e., quasi-linear Fe (I) complexes are studied. The different zero-field splittings are observed for the complexes due to the different d orbital splitting patterns. The complex **4.1** is characterized with a large spin-reversal barrier of 218.26 cm^{-1} and weak spin-phonon coupling in the complex manifesting no under-barrier relaxation. Additionally, the existence of multiple relaxation pathways with partial relaxation within ground-state KDs for complex **4.2** and barrierless potential well triggering faster relaxation within the ground-state KDs in complex **4.3** provides signatures for the absence of SIM behavior in these complexes highlighting large D is not the sole criterion to show SMM properties. Complex **4** possessing Ising-type anisotropy and blocking of ground-state QTM is predicted as the possible candidate for SIM with a large D value of -79.06 cm^{-1} which is the second highest among all other Fe(I) linear complexes reported so far.

Organic diradicals with strong isotropic ferromagnetic exchange interactions and high-spin ground-states are the potential contenders for organic-molecular magnets. In this context, we have modeled several diradicals based on exceptionally stable Blatter's radical to study the nature of exchange interactions in the diradicals.

- In *Chapter 5*, firstly, we studied the electronic structure of Blatter's radical. The unique delocalization of the spin density equally among the three nitrogen atoms makes the radical highly stable. Based on this radical, the different possible isomers of di-Blatter diradicals are modeled to understand the magnetic exchange interactions. Due to the delocalization of spin density on the three nitrogen atoms, three micromagnetic centers are created at each radical center leading to multiple magnetic exchange pathways and the resultant of these multiple pathways decide the fate of exchange coupling resulting in antiferromagnetic coupling for the stable configurations. In a few of the constrained isomers, ferromagnetic exchange interactions are observed but in a trade-off with molecular stability.

- In *Chapter 6*, with the aim to obtain ferromagnetic diradicals, we provide two distinct strategies to fine-tune the intrinsic zwitterionic ground-state of tetraphenyl-

hexaazaanthrace (TPHA), the molecule encompassing two Blatter's radical moieties. In one approach, we increased the length of the coupler between the radical centers and observed a transition from closed-shell singlet to open-shell singlet and subsequently triplet state. In another strategy, the simultaneous substitution of EDG and EWG groups at the cationic and anionic fragment of TPHA is done so as to obtain molecules with strong ferromagnetic exchange interactions.

In summary, the results presented in the thesis provide molecular engineering to enhance magnetic anisotropy in the transition-metal based complexes and isotropic ferromagnetic exchange interactions in the Blatter's based diradicals. However, still there are challenges in the study of the monometallic transition-metal based single-molecule magnets which can be targeted in future studies. The study of spin-phonon coupling with deliberate consideration of anharmonic phonons and the ways to quench it remains elusive and needs a much more dedicated study. Moreover, apart from modulating the magnetic anisotropy by the ligands, external perturbations like the electric field, pressure, and temperature also provide alternative strategies to modulate the magnetic anisotropy. Moreover, the key field of molecular magnetism is the deposition of these exotic molecules on the surface and to investigate their robustness of the magnetic properties while grafted on the surface which can be explored in future studies.

APPENDIX A

Appendix-1

A.1 Analysis with different number of roots

The rationalization for the choice of roots of a particular multiplicity is made by doing a number of test calculations with the different nroots of a particular multiplicity. The results are tabulated in Table A.1.

Table A.1: Zero field splitting (D) values (cm^{-1}) and single point energy (SPE) (Eh) obtained with different nroots of particular multiplicity for complex **3**.**2**.

nroots	**D value (cm^{-1})**		**SPE (Eh)**	
(multiplicity)	**SA-CASSCF**	**SA-NEVPT2**	**SA-CASSCF**	**SA-NEVPT2**
21,224,490(6,4,2)	-18.25	-	-3559.978771	-
4 (4)	-39.72	-29.12	-3560.417876	-3562.610221
10,4,16 (6,4,2)	-37.27	-44.77	-3560.349320	-3562.552111
11,4,16 (6,4,2)	-39.19	-45.82	-3560.344314	-3562.547112
2,4,16 (6,4,2)	-13.89	-29.57	-3560.371900	-3562.574716
1,4,10 (6,4,2)	-04.88	-35.88	-3560.397632	-3562.589917
1,4 (6,4)	-03.19	-41.96	-3560.427875	-3562.620168
1,10 (6,4)	-00.77	-45.72	-3560.403851	-3562.596121
10,4 (6,4)	-41.65	-52.37	-3560.362515	-3562.565276
11,4 (6,4)	-43.21	-54.14	-3560.354855	-3562.557627
4,16 (4,2)	-34.85	-20.32	-3560.373262	-3562.565582
4,10 (4,2)	-35.34	-19.79	-3560.380479	-3562.572793

A.2 Energetics comparison of HS, IS, and LS state

For the realization of the ground spin state of modeled complexes, a comparison of DFT optimized energies of HS, IS and LS state at B3LYP/def2-TZVPP level with D3(BJ) correction is tabulated in Table A.2.

Table A.2: DFT Optimized Energies(Eh) of HS, IS and LS state at B3LYP-D3/def2-TZVPP level.

	Energies (Eh)		
Complex	**HS**	**IS**	**LS**
3.1	-2485.504679	-2485.490454	-2485.464940
3.2	-3566.487275	-3566.495054	-3566.468020
3.3	-9908.143862	-9908.154199	-9908.126070
3.4	-3079.134919	-3079.147561	-3079.119596
3.5	-1912.305570	-1912.281083	-1912.253376
3.6	-2993.267854	-2993.246464	-2993.210633
3.7	-9334.914701	-9334.892468	-9334.866011
3.8	-2505.894444	-2505.870490	-2505.844722
3.9	-6274.402379	-6274.381714	-6274.360009
3.10	-7355.385247	-7355.385014	-7355.357939
3.11	-13697.039249	-13697.043914	-13697.015885
3.12	-6868.032555	-6868.040892	-6868.012370
3.13	-9621.532043	-9621.532300	-9621.504954
3.14	-11802.592252	-11802.599900	-11802.571672
3.15	-11515.980887	-11515.979036	-11515.950867

A.3 Bond lengths of different complexes

Table A.3: Average metal-ligand axial (M-L_{axial}) and equatorial (M-$L_{equatorial}$) bond lengths (Å) in IS and HS state geometry at B3LYP-D3/def2-TZVPP level.

	Bond Lengths (Å)			
Complex	**Average M-L_{axial}**		**Average M-$L_{equatorial}$**	
	IS	**HS**	**IS**	**HS**
3.1	2.32	2.57	1.86	1.84
3.2*	2.33	2.55	2.26	2.25
3.3	2.33	2.53	2.42	2.42
3.4	2.34	2.54	2.63	2.62
3.5	2.03	2.22	1.85	1.83
3.6	2.12	2.32	2.26	2.24
3.7	2.15	2.35	2.42	2.39
3.8	2.19	2.41	2.66	2.61
3.9	2.42	2.71	1.86	1.83
3.10	2.41	2.64	2.26	2.24
3.11	2.41	2.61	2.63	2.62
3.12	2.42	2.60	2.63	2.62
3.13	2.15(N)/22.33(P)	2.32/2.55	2.42	2.41
3.14	2.33(P)/2.42(As)	2.53/2.62	2.42	2.42
3.15	2.14(N)/2.42(As)	2.29/2.64	2.42	2.40

*Experimental M-L_{axial} and M-$L_{equatorial}$ are 2.33 and 2.26 respectively.[160]

A.4 Bond angles

Table A.4: Bond angles (°) in IS state geometry at B3LYP-D3/def2-TZVPP level. L_{a1} and L_{a2} denotes the two axial ligands and L_{e1}, L_{e2} and L_{e3} denotes the three equatorial ligands. For complex **3.13**, **3.14** and **3.15**, L_{a1} and L_{a2} are N and P, P and As and N and As respectively. In all other complexes, $L_{a1} = L_{a2}$ and $L_{e1} = L_{e2} = L_{e3}$

	Bond angles (°)			
Complex	**L_{a1}-M-L_{a2}**	**L_{e1}-M-L_{e2}**	**L_{e2}-M-L_{e3}**	**L_{e3}-M-L_{e1}**
3.1	175.5	108.0	128.5	123.4
3.2*	180.0	124.3	110.5	124.8
3.3	178.4	119.1	120.2	120.6
3.4	178.7	119.4	118.8	121.7
3.5	177.6	122.4	117.8	119.7
3.6	178.4	121.9	119.9	118.1
3.7	178.9	121.9	117.8	120.1
3.8	179.1	122.0	118.9	118.9
3.9	158.4	107.6	106.6	107.6
3.10	179.4	110.0	121.6	128.0
3.11	177.9	118.6	120.3	120.9
3.12	178.1	119.4	117.3	123.3
3.13	178.5	118.9	120.9	118.5
3.14	177.6	118.0	119.0	120.0
3.15	178.6	119.2	121.8	118.9

*Experimental L_{a1}-M-L_{a2} = 176.6°, L_{e1}-M-L_{e2} = 122.4°, L_{e2}-M-L_{e3} = 115.0° and L_{e3}-M-L_{e1} = 124.8°.[160]

A.5 Ground-spin state from different functionals

For the complexes with small adiabatic energy difference between HS and IS state obtained from B3LYP functional i.e. complex **3.10**, **3.13** and **3.15**, $\Delta E^{adia.}_{HS-IS}$ is calculated from different functionals and is tabulated in Table A.5 to predict the correct ground state. It is observed that hybrid functionals i.e. OPBE and PBE0 are biased towards HS state and gradient corrected functional PBE predicted the IS as ground state. BLYP predicted IS ground state for complex **3.10** whereas HS state for complex **3.13** and **3.15**.

Table A.5: $\Delta E^{adia.}_{HS-IS}$ obtained from different functionals for the complexes with smaller energy difference between HS and IS state.

	Complex		
Functional	**3.10**	**3.13**	**3.15**
OPBE	-17.3	-21.1	-28.1
PBE0	-17.5	-10.5	-13.7
PBE	18.8	18.4	8.8
BLYP	3.9	-7.8	-4.9

A.6 Individual contribution of different components of entropy change

Table A.6: Individual contribution of different components of entropy change i.e. ΔS_{el}, ΔS_{vib}, ΔS_{rot} and ΔS_{trans} (kcal/mol) to the total entropy change calculated at 300 K.

Complex	ΔS_{el}	ΔS_{vib}	ΔS_{rot}	ΔS_{trans}
3.1	0.24	0.81	0.09	0.00
3.2	0.24	1.15	0.08	0.00
3.3	0.24	0.85	0.05	0.00
3.4	0.24	1.98	0.03	0.00
3.5	0.24	1.02	0.07	0.00
3.6	0.24	1.11	0.04	0.00
3.7	0.24	0.98	0.03	0.00
3.8	0.24	0.93	0.00	0.00
3.9	0.24	0.04	0.12	0.00
3.10	0.24	1.14	0.08	0.00
3.11	0.24	1.14	0.06	0.00
3.12	0.24	0.97	0.06	0.00
3.13	0.24	1.76	0.04	0.00
3.14	0.24	1.70	0.05	0.00
3.15	0.24	0.80	0.05	0.00

A.7 SA-CASSCF(9,7)/NEVPT2 calculated ZFS parameters

ZFS parameters for complexes stabilized in IS state are tabulated in Table A.7 and A.8. For all the complexes, the SA-NEVPT2 results in large magnitude of D, in IS state which lowers to relatively smaller values in HS state.

For all the complexes, |E/D| values are negligibly small, leading to high axiality of magnetic anisotropy.

A.7.1 D parameter

In IS state, S =3/2, Fe(III) ion has effective unquenched angular momentum and hence leads to high ZFS values. For all the complexes with low ΔE_{HS-IS}, large ZFS values are calculated with both SA-CASSCF and NEVPT2 calculations in IS geometry. We calculated the large values for the HS optimized geometries from SA-CASSCF. The sizeable D value in HS Fe(III) complexes stems from closely lying quartet S=3/2 excited state. Although the values from NEVPT2 calculation are relatively very small, ($<$ |2| cm^{-1}), which agrees with quenched orbital momentum in HS state. It can be pointed out that the dynamic correlations become very important in such cases with closely lying sextet and quartet ground state in Fe(III) complexes. Therefore, the results from the SA-CASSCF should then be verified from NEVPT2 calculation.

Table A.7: D value (cm $^{-1}$) of complexes from SA-CASSCF(9,7) and NEVPT2 in HS and IS state on their respective geometries.

Complex	D value (cm $^{-1}$)			
	SA-CASSCF		SA-NEVPT2	
	HS	IS	HS	IS
3.1	-1.56	-4.63	-1.29	-3.66
3.2	-67.46	-37.27	-1.56	-44.78
3.3	-65.21	-58.24	-2.43	-58.09
3.4	-59.70	-56.71	-9.78	-42.06
3.5	-1.40	-2.21	-1.82	-2.94
3.6	-1.94	-3.28	-0.84	-2.21
3.7	-1.86	-2.72	-1.45	-2.13
3.8	-3.32	-25.61	-0.45	-2.29
3.9	-1.22	-5.19	-0.31	-1.72
3.10	-38.26	-32.79	-1.30	-51.66
3.11	-64.69	-55.18	-1.80	-54.89
3.12	-62.02	-56.37	-18.02	-54.94
3.13	-60.83	-52.84	-2.06	-57.42
3.14	-64.98	-56.12	-2.10	-54.86
3.15	-59.42	-51.61	-1.67	-51.87

A.7.2 E parameter

Table A.8: |E/D| value of complexes from SA-CASSCF(9,7) and NEVPT2 in HS and IS state on their respective geometries.

Complex	|E/D| value			
	SA-CASSCF		SA-NEVPT2	
	HS	IS	HS	IS
3.1	0.011	0.028	0.012	0.019
3.2	0.011	0.006	0.054	0.020
3.3	0.003	0.001	0.005	0.002
3.4	0.006	0.020	0.044	0.002
3.5	0.010	0.019	0.010	0.008
3.6	0.024	0.018	0.018	0.018
3.7	0.027	0.010	0.024	0.009
3.8	0.253	0.121	0.023	0.044
3.9	0.131	0.018	0.329	0.194
3.10	0.056	0.018	0.021	0.024
3.11	0.002	0.001	0.016	0.001
3.12	0.005	0.003	0.021	0.003
3.13	0.001	0.001	0.009	0.001
3.14	0.002	0.001	0.014	0.003
3.15	0.002	0.001	0.017	0.001

APPENDIX **B**

Appendix-2

B.1 Comparison of *D* values with different roots

Table B.1: Comparison of *D* values obtained from SA-CASSCF/NEVPT2 calculations by considering all the roots i.e., quartet and doublet vs only quartet roots.

Complex	**Quartet and Doublet roots**		**Only Quartet roots**	
	$D(\text{cm}^{-1})$	$\lvert E/D \rvert$	$D(\text{cm}^{-1})$	$\lvert E/D \rvert$
4.1	-107.24	0.0004	-109.13	0.0004

B.2 Löwdin *d*-orbital composition analysis

Table B.2: Löwdin *d*-orbital composition analysis of all the complexes.

Complex	d_{z^2}	d_{xy}	$d_{x^2-y^2}$	d_{xz}	d_{yz}
4.1	82.4+8.0s	99.2	99.2	96.2	96.2
4.2	80.2+11.1s	99.6	99.6	95.0	96.2
4.3	79.8+10.8s	99.5	99.4	94.9	95.5
4.4	87.4+3.1s	91.5	91.8	92.0	91.5
4.5	81.1+9.9s	99.3	99.3	94.7	94.6

B.3 *d*-orbital energy ordering of all complexes

The reason for the different non-Aufbau behavior of systems **4.2** and **4.5** with respect to **4.3** is the energy difference between the 3^{rd} and 4^{th} orbitals which is smaller for complexes **4.2** and **4.5** i.e., 0.16 and 0.13 eV respectively. However, for complex **4.3**, the energy gap between 3^{rd} and 4^{th} orbital is large i.e., 0.24 eV. Therefore, the electron

occupies the 4^{th} orbital in complex **4.2** and **4.5**. However, due to larger energy difference between 3^{rd} and 4^{th} orbital in the case of complex **4.3**, the electron goes to the 3^{rd} orbital.

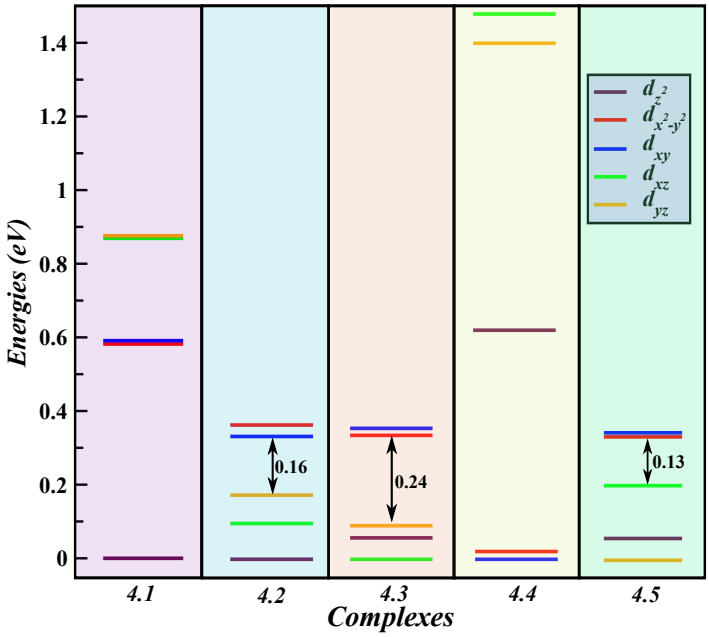

Figure B.1: The energetic splitting of d-orbitals obtained from AILFT analysis of SA-CASSCF/NEVPT2 calculations.

B.4 Molecular orbitals

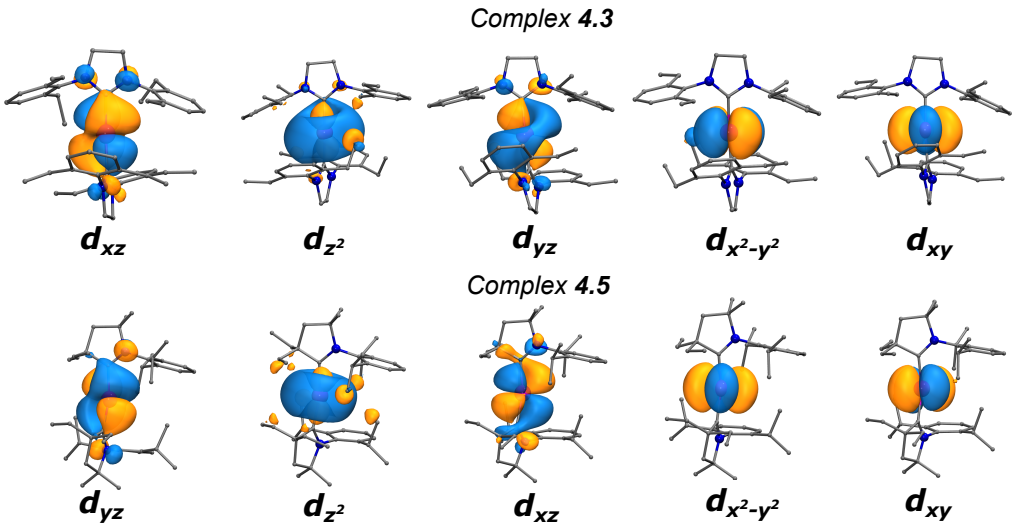

Figure B.2: Molecular orbitals of complex **4.3** and **4.5** obtained from SA-CASSCF/NEVPT2 calculations.

B.5 Structural parameters

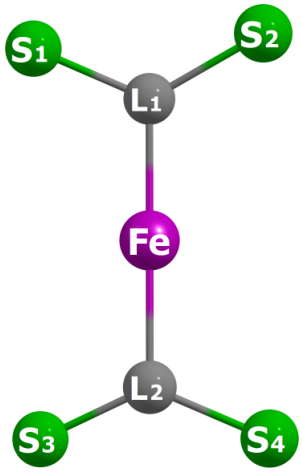

Figure B.3: Model to show structural parameters.

Table B.3: Bond distance of Fe with the atom of ligand directly attached to Fe and bond angles.

Complexes	Bond Lengths (Å)		Bond Angles (°)
	Fe-L1	Fe-L2	L1-Fe-L2
4.1	2.06	2.06	179.19
4.2	1.99	2.00	178.68
4.3	1.98	1.97	175.82
4.4	2.02	1.64	180.00
4.5	1.98	1.98	165.35

Table B.4: Dihedral angles (°)

Complexes	Dihedral angles (°)			
	cis		trans	
	S1-L1-L2-S3	S2-L1-L2-S4	S1-L1-L2-S4	S2-L1-L2-S3
4.1	21.79	22.19	-141.38	-97.39
4.2	14.14	14.19	-165.69	-165.96
4.3	70.21	69.78	-108.00	-111.99
4.4	-	-	-	-
4.5	71.44	52.83	-117.83	-117.88

B.6 Spin-Phonon coupling coefficient calculations for complex 4.1

Firstly, the geometry is optimized followed by determining the vibrational spectrum of the optimized geometry at B3LYP/def2-TZVP level. These calculations are performed

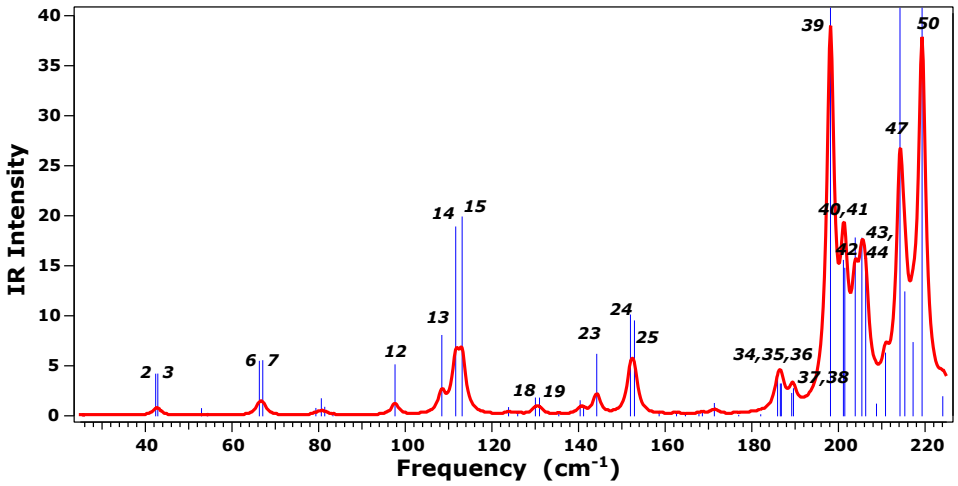

Figure B.4: Low energy vibrational spectra of complex 4.1.

with the Gaussian (g16) software. The vibrational spectra with the energies less than 220 cm^{-1} is shown in Figure B.4. In the next step, for the vibrational frequencies with energy lower than the spin-reversal barrier calculated for the complex i.e., < 220 cm^{-1}, we then computed the spin-phonon coupling coefficients, C_k in all the three directions i.e., x, y, and z, wherein C_k is calculated using Eq. 4.1 as the second derivative of the g component in x, y or z direction with respect to the distortion in the structure, Q_k corresponding to the vibrational mode *k*.

Since, C_k involves the second derivative of g component, the g tensor for each particular vibrations are determined at different distorted structures by making shifts until ± 0.75 Å in steps of 0.25. The determination of g components is done within the CASSCF approach in Orca. As for each particular vibration, we considered 6 different distorted structures, therefore, 6 CASSCF calculations are run for each vibrational mode. C_k quantifies the coupling strength of the k^{th} mode and the sign of C_k is related to the sign of the second derivative of g with respect to Q_k. Thus, the positive sign implies that g increase from the reference value at T = 0 while the negative sign means that g decrease as the temperature is raised.

The energies and the reduced masses and the computed spin-phonon coupling coefficients of all the low frequency vibrational modes are tabulated in Table B.5.

Table B.5: The double derivative of g tensors i.e., g_x'', g_y'' and g_z'', reduced mass, vibrational frequencies and the spin phonon-coupling coefficients C_k using Eq. 4.1 in the main text of the low energy vibrational modes.

Mode	$\mathbf{g}_x''$ (Å^{-2})	$\mathbf{g}_y''$ (Å^{-2})	$\mathbf{g}_z''$ (Å^{-2})	$\mathbf{m}_k$	ν_k	$\mathbf{C}_k$ ($\mathbf{g}_x''$)	**Ck**($\mathbf{g}_y''$)	**Ck** ($\mathbf{g}_z''$)
1	0.00006	0.00006	-0.0044	3.90	25.68	1.0×10^{-5}	1.0×10^{-5}	-7.4×10^{-4}
2	0.00006	0.00008	-0.005	3.39	42.37	7.0×10^{-6}	9.4×10^{-6}	-5.9×10^{-4}
3	0.0002	0.0002	-0.009	3.40	42.87	2.3×10^{-5}	2.3×10^{-5}	-1.0×10^{-3}
4	0.0018	0.002	-0.0272	3.87	52.96	1.5×10^{-4}	1.6×10^{-4}	-2.2×10^{-3}
5	0.0012	0.0014	-0.0262	3.9	54.40	9.4×10^{-5}	1.1×10^{-4}	-2.1×10^{-3}
6	0.0002	0.0004	-0.0046	3.12	66.31	1.6×10^{-5}	3.3×10^{-5}	-3.7×10^{-4}

7	0.0002	0.0002	-0.006	3.17	67.10	1.6×10^{-5}	1.6×10^{-5}	-4.7×10^{-4}
8	0.0006	0.0008	-0.0226	3.00	79.36	4.2×10^{-5}	5.7×10^{-5}	-1.6×10^{-3}
9	0.00018	0.0004	-0.0504	2.86	80.62	1.3×10^{-5}	2.9×10^{-5}	-3.7×10^{-3}
10	-0.0002	-0.0001	-0.0272	3.56	81.40	-1.2×10^{-5}	-5.8×10^{-6}	-1.6×10^{-3}
11	0.0004	0.0004	-0.0058	3.27	83.30	2.5×10^{-5}	2.5×10^{-5}	-3.6×10^{-4}
12	0.001	0.001	-0.0028	2.90	97.63	5.9×10^{-5}	5.9×10^{-5}	-1.7×10^{-4}
13	0.0014	0.0014	-0.006	2.03	108.43	1.1×10^{-4}	1.1×10^{-4}	-4.6×10^{-4}
14	0.007	0.0072	-0.0286	4.86	111.64	2.2×10^{-4}	2.2×10^{-4}	-8.9×10^{-4}
15	0.0086	0.0088	-0.0242	6.04	113.12	2.1×10^{-4}	2.2×10^{-4}	-6.0×10^{-4}
16	-0.0004	-0.0004	-0.0098	1.18	123.84	-4.6×10^{-5}	-4.6×10^{-5}	-1.1×10^{-3}
17	-0.0004	-0.0004	-0.012	1.22	125.95	-4.4×10^{-5}	-4.4×10^{-5}	-1.3×10^{-3}
18	0.000014	0.00002	-0.0024	1.08	130.04	1.7×10^{-6}	2.4×10^{-6}	-2.9×10^{-4}
19	-0.0004	-0.0002	-0.0036	1.12	130.98	-4.6×10^{-5}	-2.3×10^{-5}	-4.1×10^{-4}
20	0.0022	0.0024	-0.0048	1.25	135.44	2.2×10^{-4}	2.4×10^{-4}	-4.8×10^{-4}
21	-0.0018	-0.0018	-0.0042	2.45	140.37	-8.8×10^{-5}	-8.8×10^{-5}	-2.1×10^{-4}
22	-0.0022	-0.002	-0.0046	2.67	141.16	-9.8×10^{-5}	-8.9×10^{-5}	-2.1×10^{-4}
23	0.0036	0.0038	-0.0274	1.46	144.20	2.9×10^{-4}	3.0×10^{-4}	-2.2×10^{-3}
24	0.0038	0.0038	-0.028	3.44	151.97	1.2×10^{-4}	1.2×10^{-4}	-9.0×10^{-4}
25	0.0036	0.0038	-0.0274	3.80	152.90	1.0×10^{-4}	1.1×10^{-4}	-7.9×10^{-4}
26	0.0018	0.0018	-0.0046	2.15	158.60	8.9×10^{-5}	8.9×10^{-5}	-2.3×10^{-4}
27	-0.00001	-0.00006	-0.0056	1.16	162.62	-8.9×10^{-7}	-5.3×10^{-6}	-5.0×10^{-4}
28	-0.0002	-0.0002	-0.004	1.15	164.68	-1.8×10^{-5}	-1.8×10^{-5}	-3.5×10^{-4}
29	-0.00008	-0.00006	-0.0056	1.14	167.79	-7.0×10^{-6}	-5.3×10^{-6}	-4.9×10^{-4}
30	0.000004	0.00004	-0.0054	1.15	168.58	3.5×10^{-7}	3.5×10^{-6}	-4.7×10^{-4}
31	0.0002	0.0002	-0.0016	1.91	171.35	1.0×10^{-5}	1.0×10^{-5}	-8.2×10^{-5}
32	0.00014	0.00014	-0.0006	1.45	176.98	9.2×10^{-6}	9.2×10^{-6}	-3.9×10^{-5}
33	0.00012	0.00012	-0.0006	1.26	182.05	8.8×10^{-6}	8.8×10^{-6}	-4.4×10^{-5}
34	0.0004	0.0004	-0.002	1.78	185.95	2.0×10^{-5}	2.0×10^{-5}	-1.0×10^{-4}
35	0.000008	0.00002	-0.0022	1.90	186.58	3.8×10^{-7}	9.5×10^{-7}	-1.0×10^{-4}
36	0.0008	0.0008	-0.0028	1.72	186.81	4.2×10^{-5}	4.2×10^{-5}	-1.5×10^{-4}
37	-0.00006	-0.00002	-0.006	2.22	189.20	-2.4×10^{-6}	-8.0×10^{-7}	-2.4×10^{-4}
38	-0.00004	-0.000004	-0.0062	1.94	189.61	-1.8×10^{-6}	-1.8×10^{-7}	-2.8×10^{-4}
39	0.0002	0.0002	-0.0014	1.34	198.16	1.3×10^{-5}	1.3×10^{-5}	-8.8×10^{-5}
40	0.0022	0.0024	-0.0102	2.22	201.14	8.3×10^{-5}	9.0×10^{-5}	-3.8×10^{-4}
41	0.002	0.002	-0.0084	2.23	201.47	7.5×10^{-5}	7.5×10^{-5}	-3.1×10^{-4}
42	0.0004	0.0004	-0.004	1.5	203.87	2.2×10^{-5}	2.2×10^{-5}	-2.2×10^{-4}
43	0.0002	0.0004	-0.0112	1.96	205.41	8.4×10^{-6}	1.7×10^{-5}	-4.7×10^{-4}
44	0.0002	0.0002	-0.009	1.94	206.29	8.4×10^{-6}	8.4×10^{-6}	-3.8×10^{-4}
45	0.00004	0.00006	-0.00008	1.26	208.78	2.6×10^{-6}	3.8×10^{-6}	-5.1×10^{-6}
46	0.0002	0.0002	-0.00014	1.19	210.87	1.3×10^{-5}	1.3×10^{-5}	-9.3×10^{-6}
47	-0.0002	-0.00018	0.0004	1.51	214.21	-1.0×10^{-5}	-9.3×10^{-6}	2.1×10^{-5}
48	-0.00018	-0.00016	0.0004	1.45	215.32	-9.7×10^{-6}	-8.6×10^{-6}	2.1×10^{-5}
49	0.0001	0.00012	-0.0002	1.15	217.23	6.7×10^{-6}	8.0×10^{-6}	-1.3×10^{-5}
50	0.0004	0.0004	-0.0012	2.53	219.30	1.2×10^{-5}	1.2×10^{-5}	-3.6×10^{-5}

Since, the spin-phonon interactions are weak, therefore, in the weak coupling regime,

it is the linear derivative of the g components that is considered[221,222] and the spin-phonon coupling coefficient reads as

$$C_k = \frac{\hbar}{4\pi}\left(\frac{\delta g}{\delta Q_k}\right)\frac{1}{m_k \nu_k} \tag{B.1}$$

The spin-phonon coupling coefficients calculated with the linear derivative of the g components employing Eq. B.1 are collected in Table B.6. For all the low energy vibrational modes, these are also computed to be very small and the corresponding thermal populations of the different modes is also very small. Thus, indicating the feeble spin-phonon coupling for the lower vibrations highlighting the relaxation to take place via the first excited state with the spin-reversal barrier of 218.26 cm^{-1}, in well agreement with the experiments.

Table B.6: The linear derivative of g tensors i.e., g'_x, g'_y and g'_z and the calculated spin phonon-coupling coefficients C_k using Eq. B.1 of the low energy vibrational modes.

Modes	$\mathbf{g}'_x$ ($Å^{-2}$)	$\mathbf{g}'_y$ ($Å^{-2}$)	$\mathbf{g}'_z$ ($Å^{-2}$)	$\mathbf{C}_k$ ($\mathbf{g}'_x$)	**Ck**($\mathbf{g}'_y$)	**Ck** ($\mathbf{g}'_z$)
1	0.001	0.001	-0.0023	1.7×10^{-4}	1.7×10^{-4}	-3.9×10^{-4}
2	0.0001	0.0001	0.0002	1.2×10^{-5}	1.2×10^{-5}	2.3×10^{-5}
3	0.000001	-0.0000007	-0.0001	1.2×10^{-7}	-8.1×10^{-8}	-1.2×10^{-5}
4	-0.00004	-0.00004	-0.00007	-3.3×10^{-6}	-3.3×10^{-6}	-5.8×10^{-6}
5	-0.0001	-0.0001	0.0004	-7.8×10^{-6}	-7.8×10^{-6}	3.1×10^{-5}
6	0.000004	-0.0000007	-0.0001	3.3×10^{-7}	-5.7×10^{-8}	-8.1×10^{-6}
7	-0.00001	-0.00001	0.0001	-7.9×10^{-7}	-7.9×10^{-7}	7.9×10^{-6}
8	0.0012	0.0012	-0.0012	8.5×10^{-5}	8.5×10^{-5}	-8.5×10^{-5}
9	-0.0002	-0.0002	0.0003	-1.5×10^{-5}	-1.5×10^{-5}	2.2×10^{-5}
10	-0.0008	-0.0008	0.0011	-4.6×10^{-5}	-4.6×10^{-5}	6.4×10^{-5}
11	-0.0015	-0.0015	0.0033	-9.3×10^{-5}	-9.3×10^{-5}	2.0×10^{-4}
12	-0.0001	-0.0001	0.0002	-5.9×10^{-6}	-5.9×10^{-6}	1.2×10^{-5}
13	-0.00002	-0.00002	0.00002	-1.5×10^{-6}	-1.5×10^{-6}	1.5×10^{-6}
14	-0.0001	-0.0001	0.0005	-3.1×10^{-6}	-3.1×10^{-6}	1.6×10^{-5}
15	-0.0001	-0.0001	0.0024	-2.5×10^{-6}	-2.5×10^{-6}	5.9×10^{-5}
16	-0.0001	-0.0001	0.0003	-1.1×10^{-5}	-1.1×10^{-5}	3.4×10^{-5}
17	0.0005	0.0005	-0.0018	5.5×10^{-5}	5.5×10^{-5}	-2.0×10^{-4}
18	-0.0001	-0.0001	0.0004	-1.2×10^{-5}	-1.2×10^{-5}	4.8×10^{-5}
19	0.0003	0.0003	-0.0012	3.4×10^{-5}	3.4×10^{-5}	-1.4×10^{-4}
20	-0.0029	-0.0029	0.008	-2.9×10^{-4}	-2.9×10^{-4}	8.0×10^{-4}
21	-0.0005	-0.0005	0.0017	-2.4×10^{-5}	-2.4×10^{-5}	8.3×10^{-5}
22	0.0002	0.0002	-0.001	8.9×10^{-6}	8.9×10^{-6}	-4.5×10^{-5}
23	0.0004	0.0004	-0.001	3.2×10^{-5}	3.2×10^{-5}	-8.0×10^{-5}
24	0.0005	0.0005	-0.0016	1.6×10^{-5}	1.6×10^{-5}	-5.1×10^{-5}
25	0.0004	0.0004	-0.001	1.2×10^{-5}	1.2×10^{-5}	-2.9×10^{-5}
26	-0.0021	-0.0021	0.007	-1.0×10^{-4}	-1.0×10^{-4}	3.5×10^{-4}
27	0.0001	0.0001	-0.0005	8.9×10^{-6}	8.9×10^{-6}	-4.4×10^{-5}
28	0.0001	-0.0001	0.0003	8.8×10^{-6}	-8.8×10^{-6}	2.7×10^{-5}

29	-0.000007	-0.00001	0.0001	-6.1×10^{-7}	-8.8×10^{-7}	8.8×10^{-6}
30	-0.0002	-0.0002	0.0007	-1.7×10^{-5}	-1.7×10^{-5}	6.1×10^{-5}
31	-0.0002	-0.0002	0.0008	-1.0×10^{-5}	-1.0×10^{-5}	4.1×10^{-5}
32	-0.0001	-0.0001	0.0007	-6.6×10^{-6}	-6.6×10^{-6}	4.6×10^{-5}
33	-0.0002	-0.0002	0.0007	-1.5×10^{-5}	-1.5×10^{-5}	5.1×10^{-5}
34	0.0007	0.0007	-0.0022	3.6×10^{-5}	3.6×10^{-5}	-1.1×10^{-4}
35	0.0004	0.0004	-0.0012	1.9×10^{-5}	1.9×10^{-5}	-5.7×10^{-5}
36	0.0012	0.0012	-0.0034	6.3×10^{-5}	6.3×10^{-5}	-1.8×10^{-4}
37	0.0002	0.0002	-0.0007	8.0×10^{-6}	8.0×10^{-6}	-2.8×10^{-5}
38	0.0005	0.0005	-0.0017	2.3×10^{-5}	2.3×10^{-5}	-7.8×10^{-5}
39	-0.0003	-0.0003	0.001	-1.9×10^{-5}	-1.9×10^{-5}	6.3×10^{-5}
40	0.00008	0.00008	-0.0003	3.0×10^{-6}	3.0×10^{-6}	-1.1×10^{-5}
41	0.0002	0.0002	-0.0006	7.5×10^{-6}	7.5×10^{-6}	-2.2×10^{-5}
42	-0.0005	-0.0005	0.0015	-2.7×10^{-5}	-2.7×10^{-5}	8.2×10^{-5}
43	0.0003	0.0003	-0.0013	1.3×10^{-5}	1.3×10^{-5}	-5.4×10^{-5}
44	0.0004	0.0004	-0.0013	1.7×10^{-5}	1.7×10^{-5}	-5.5×10^{-5}
45	0.00005	0.00005	-0.00009	3.2×10^{-6}	3.2×10^{-6}	-5.8×10^{-6}
46	0.000006	0.000005	-0.00001	4.0×10^{-7}	3.3×10^{-7}	-6.7×10^{-7}
47	-0.0002	-0.0002	0.0007	-1.0×10^{-5}	-1.0×10^{-5}	3.6×10^{-5}
48	0.0003	0.0003	-0.001	1.6×10^{-5}	1.6×10^{-5}	-5.4×10^{-5}
49	0.0001	0.0001	-0.0002	6.7×10^{-6}	6.7×10^{-6}	-1.3×10^{-5}
50	0.0005	0.0005	-0.0018	1.5×10^{-5}	1.5×10^{-5}	-5.5×10^{-5}

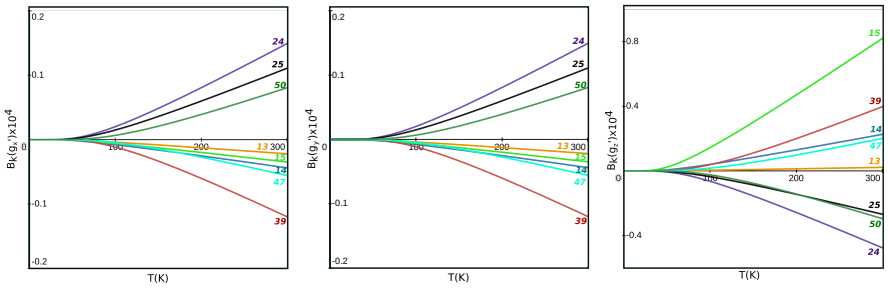

Figure B.5: Calculated B_k values considering linear derivative of g tensor, in x, y, and z directions, for the low energy vibrational modes calculated at CASSCF level.

APPENDIX C

Appendix-3

C.1 DFT based methods

C.1.1 Spin-constraint DFT: Selection of the constrained zones

Often DFT based broken symmetry approach overestimates the exchange couplings due to spurious delocalization of magnetic orbitals, especially in the case of highly conjugated and symmetric molecules. For di-Blatter diradicals, owing to highly conjugated and nearly planar geometries of **b-b, b-c** and **c-c** isomers, the overestimation of $2J$'s is even more prominent in stable configurations. Thus, appropriately confining the magnetic moment on the selected zones is necessary to obtain more accurate exchange couplings using constrained DFT calculations.

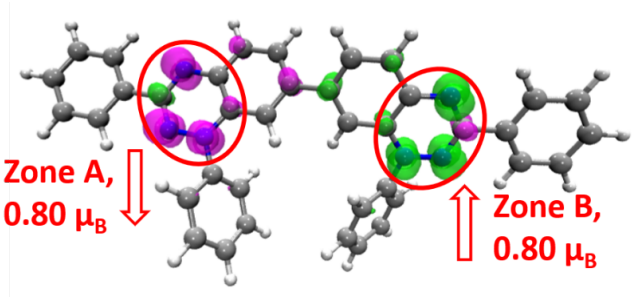

Figure C.1: CBS-DFT; spatially constrained zones for 'c-c' isomer with the constrained magnetic moment of 0.80 μ_B on the respective zones. The pink and green color represents α and β spin with isovalue of $5\text{x}10^{-3}$ $\mu_B/\text{Å}^3$.

Fig. C.1 illustrates the selected zones and the respective magnetic moments for **c-c** isomer. Both the zones, i.e., Zone A and Zone B are localized on the triazinyl rings of the individual Blatter's moieties. The natural delocalization of spin density from the triazinyl ring to the fused benzene ring of Blatter's radical is one of the reasons behind its super-stability. Thus, only 0.80 μ_B amount of magnetic moment is constrained on

the triazinyl ring, allowing rest of the 0.20 μ_B spin moment to delocalize on the fused benzene ring for both the radical monomers. This methodology is followed for all the 10 possible isomers under study.

Table C.1: Total energies and calculated magnetic exchange coupling constant ($2J$) for the 10 possible isomers of di-Blatter diradical using CBS-DFT; B3LYP/6-311G* method.

Possible Isomers	**Energies(Eh)**		**$2J$ (cm^{-1})**
	HS	**BS**	
	$< S^2 >_{HS}$	$< S^2 >_{BS}$	
a-a	-1792.542798	-1792.542788	4.38
	2.03	1.03	
a-b	-1792.547626	-1792.547971	-127.28
	2.03	1.01	
a-c	-1792.547128	-1792.547511	-168.01
	2.03	1.01	
a-d	-1792.537223	-1792.537148	32.92
	2.03	1.03	
b-b	-1792.550359	-1792.550736	-165.48
	2.03	1.01	
b-c	-1792.550754	-1792.551258	-219.46
	2.03	1.00	
c-c	-1792.550553	-1792.551795	-544.28
	2.03	0.99	
b-d	-1792.539032	-1792.539144	-49.16
	2.03	1.02	
c-d	-1792.539063	-1792.538986	33.78
	2.03	1.02	
d-d	-1792.528119	-1792.528098	9.2
	2.03	1.03	

The comparison of computed $2J$'s using CBS-DFT and BS-DFT (tabulated in Table C.1 and C.2) reveals that for **c-c** isomer, exchange coupling produced by CBS-DFT, i.e., -544.28 cm^{-1}, is in close agreement to experimentally reported $2J$, i.e., -444.19 cm^{-1}, as compared to BS-DFT which results in $2J$ value of -599.92 cm^{-1}. The similar trend is observed for **b-b** and **b-c** isomers. However, no significant difference is observed in BS-DFT and CBS-DFT for the sterically hindered isomers, with connecting sites "a" and "d". This is due to orthogonal orientation of radical centres with respect to each other in these isomers, which results in broken conjugation of π-orbitals, thereby preventing the over-delocalization of magnetic orbitals by itself.

C.1.2 BS-DFT

Table C.2: Total energies and calculated magnetic exchange coupling constant (2J) for the 10 possible isomers of di-Blatter diradical using BS-DFT; B3LYP/def2-TZVP method.

Possible Isomers	**Energies(Eh)**		**2J (cm^{-1})**
	HS	**BS**	
	$< S^2 >_{HS}$	$< S^2 >_{BS}$	
a-a	-1791.694112	-1791.694101	4.94
	2.03	1.03	
a-b	-1791.698629	-1791.699000	-162.7
	2.03	1.01	
a-c	-1791.698087	-1791.69847	-168.1
	2.03	1.01	
a-d	-1791.68757	-1791.687504	31.44
	2.03	1.03	
b-b	-1791.701992	-1791.702443	-196.36
	2.03	1.00	
b-c	-1791.702347	-1791.702945	-262.38
	2.03	1.00	
c-c	-1791.701589	-1791.702956	-599.92
	2.03	0.98	
b-d	-1791.689896	-1791.690032	-59.56
	2.03	1.01	
c-d	-1791.689806	-1791.689739	29.3
	2.03	1.02	
d-d	-1791.677492	-1791.67747	10.2
	2.03	1.03	

C.2 Wave-function based multi-configurational methods

C.2.1 Selection of active space for CASSCF/NEVPT2 calculations

Various combinations of active space are explored for '**c-c**' isomer to find an optimum and appropriate space that can correctly predict the singlet-triplet energy gap in good agreement with experimental data. Starting from the minimal CAS space, i.e., CAS(2,2) which takes into account two electrons in two magnetic orbitals, the space is extended up to CAS(6,6). Table C.3 illustrates the computed exchange couplings using different active space for **'c-c'** isomer. For CAS(2,2), two SOMO's containing two unpaired electrons in the radical centres are involved. As illustrated in Fig C.2, both the SOMO's are localized on the triazinyl and fused benzene ring of both the radical monomers. With this, CAS(2,2) provides with exchange coupling of -164.16 cm^{-1} which improves to 511.60 cm^{-1} upon inclusion of dynamical correlation by NEVPT2 method, which is in close agreement to the experimental 2J value of -444.19 cm^{-1}.

Further, to obtain a complete understanding of the computed exchange couplings, the CAS space is extended to CAS(4,4). For CASSCF (4,4), as shown in Fig. C.2,

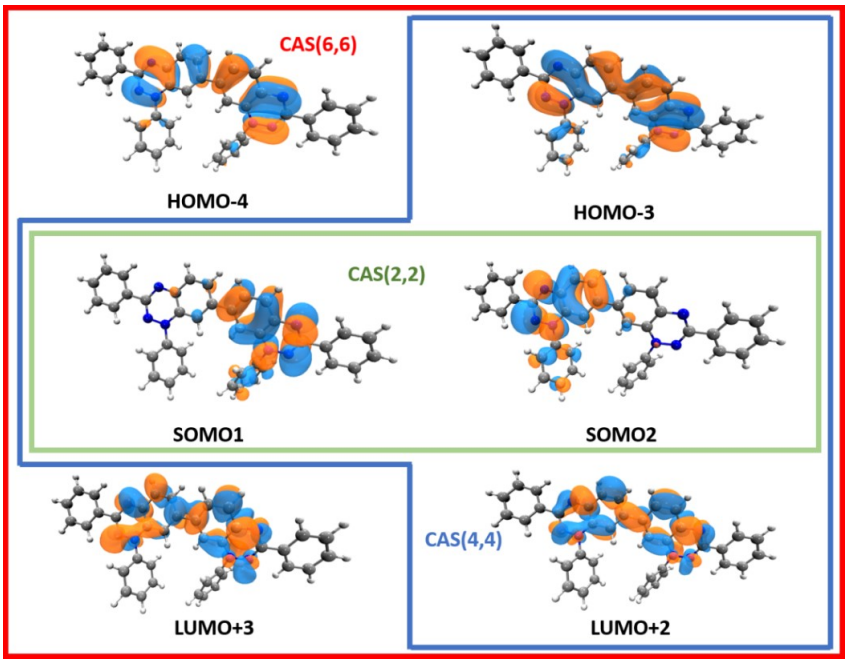

Figure C.2: Selected Orbitals for CASSCF active space. The orbitals in the CAS(2,2) are enclosed in the green box and that of CAS(4,4) and CAS(6,6) are enclosed in the blue and red box respectively. The orbitals are plotted at the isovalue of 0.02 a.u.

along with the two SOMOs, the additional π-orbitals, i.e., HOMO-3 and LUMO+2, delocalized on both the radical sites as well as the single bond connecting both the radical monomers are taken into account. Although the total energy is decreasing with the increasing size of CAS space, but CAS(4,4) yields an underestimated value of -156.48 cm^{-1}. The inclusion of dynamical correlation even worsened the situation providing strongly overestimated exchange coupling of -859.68 cm^{-1}. CAS(4,4) is further enlarged to CAS(6,6) by adding the two additional π- orbitals, i.e., HOMO-4 and LUMO+3, along with all the orbitals of CAS(4,4) space. Although CAS(6,6) also produces a better $2J$ value of -533.76 cm^{-1}, but with an overestimated exchange on incorporating dynamical correlation. A similar scenario was also observed in one of our recent works where quite promising results were obtained with CASSCF(2,2)+NEVPT2 and CASSCF(6,6).[244] The similar overestimation of exchange couplings on the inclusion of dynamical correlation for larger active spaces was also observed therein.

Table C.3: Calculated magnetic exchange using CASSCF and CASSCF-NEVPT2 with different active space for the experimentally synthesized isomer 'c-c'.

Active Space	**E(HS)**	**E(LS)**	**$2J$(cm^{-1})**
CAS(2,2)	-1781.35023	-1781.35069	-164.16
CAS(4,4)	-1781.35186	-1781.35258	-156.48
CAS(6,6)	-1781.36886	-1781.37129	-533.76
CAS(2,2)-NEVPT2	-1789.14170	-1789.14403	-511.6
CAS(4,4)-NEVPT2	-1789.12964	-1789.13356	-859.68
CAS(6,6)-NEVPT2	-1789.13559	-1789.13931	-817.1

C.2.2 Computed exchange interactions and spin-states energies

Table C.4: Computed energies (Eh) and calculated magnetic exchange coupling constant for the possible isomers of di-Blatter diradical using CASSCF(2,2) and CASSCF(2,2)-NEVPT2.

Possible	CASSCF			CASSCF-NEVPT2		
Isomers	E(HS)	E(LS)	$2J(cm^{-1})$	E(HS)	E(LS)	$2J(cm^{-1})$
a-a	-1781.34287	-1781.34283	8.77	-1789.14007	-1789.13999	17.99
a-b	-1781.34677	-1781.34692	-32.48	-1789.13874	-1789.13921	-103.15
a-c	-1781.34617	-1781.34628	-25.02	-1789.13997	-1789.14039	-92.39
a-d	-1781.33295	-1781.33288	15.8	-1789.14694	-1789.14681	30.5
b-b	-1781.35011	-1781.35047	-79.42	-1789.13722	-1789.13794	-158.02
b-c	-1781.35023	-1781.35069	-100.73	-1789.13850	-1789.13959	-240.54
c-c	-1781.34952	-1781.35027	-164.16	-1789.14170	-1789.14403	-511.6
b-d	-1781.33500	-1781.33507	-16.02	-1789.13819	-1789.13825	-12.57
c-d	-1781.33429	-1781.33424	11.85	-1789.14090	-1789.14072	38.84
d-d	-1781.31895	-1781.31894	2.41	-1789.15184	-1789.15181	7.46

C.3 Calculation of individual pairwise exchange interactions

For isomer 'b-c'

There are 9 possible pairwise magnetic exchange interactions prevailing between N1-N4, N1- N5, N1-N6, N2-N4, N2-N5, N2-N6, N3-N4, N3-N5 and N3-N6 (denoted by $2J_{N1-N4}$, $2J_{N1-N5}$, $2J_{N1-N6}$, $2J_{N2-N4}$, $2J_{N2-N5}$, $2J_{N2-N6}$, $2J_{N3-N4}$, $2J_{N3-N5}$, $2J_{N3-N6}$) as shown in Fig. C.3.

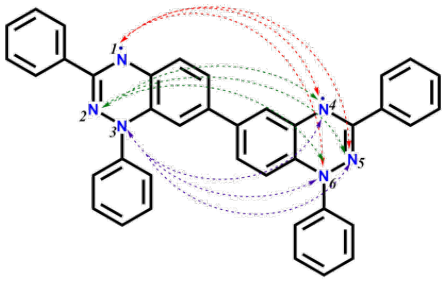

Figure C.3: Different possible interactions in isomer 'b-c'.

The individual interactions are considered by replacing all the N-atoms with the isoelectronic CH units except the considered pair of N-atoms. For example, to determine the exchange for N1-N4, all N-atoms except N1 and N4 are replaced by isoelectronic CH units as illustrated by bc_1 unit of Fig C.4.

As tabulated in Table C.6, due to difference in spin densities obtained for CH-substituted diradicals (bc_1-bc_9) and isomer **'b-c'**, the calculated coupling constants ($2J'_{Nx-Ny}$) are overestimated for bc_1–bc_9. Thus, the true magnitude of exchange interaction ($2J_{N1-N4}$) is calculated as below:

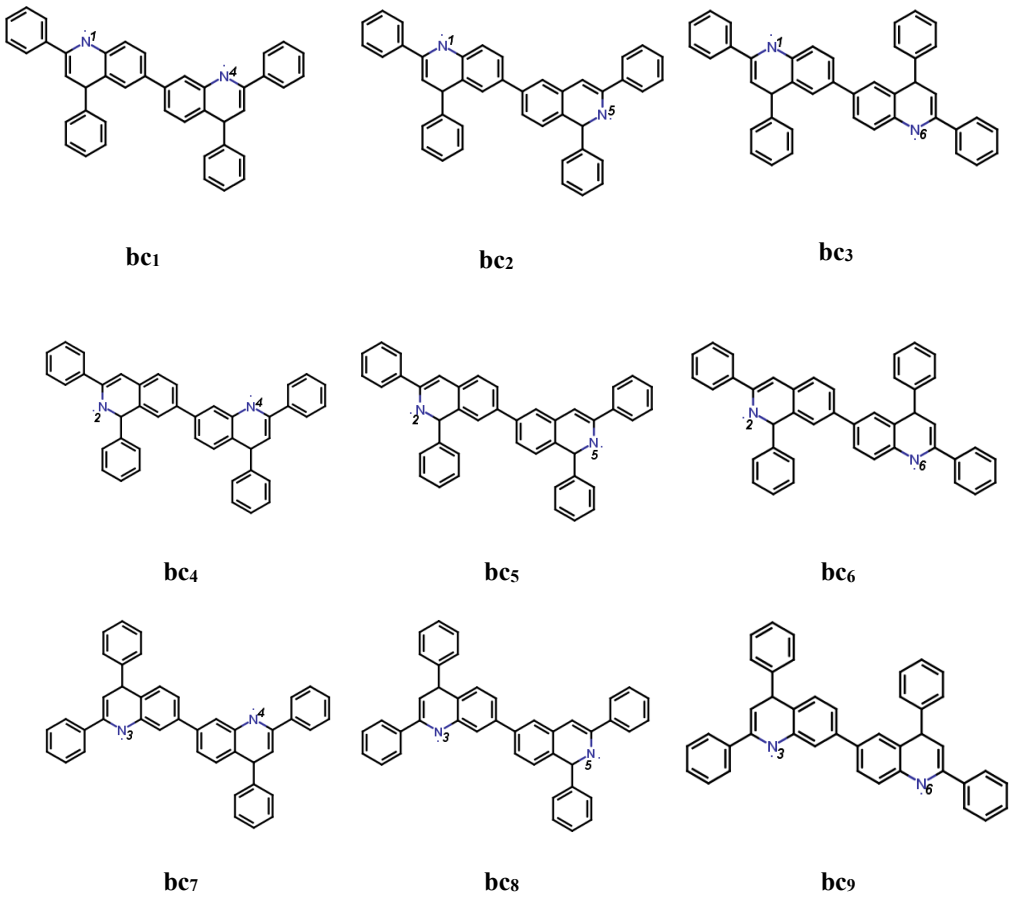

Figure C.4: Diradicals bc_1 – bc_9 to compute individual pairwise interactions taking place in isomer 'b-c'.

For **N1-N4**:
When the average spin density is 0.339 (in diradical bc_1) (Table C.5), $2J'_{N1-N4} = 299.1$ cm^{-1}
However, the true spin density (in isomer **'b-c'**) is 0.227,
so

$$2J_{N1-N4} = \frac{0.227}{0.399} \times 299.1 = 200.28\ cm^{-1}$$

It can be written as $2J_{N1-N4} = c_{14} \times 2J'_{N1-N4}$
where c_{14} is the ratio of Average lowdin spin population on N1 and N4 in isomer b-c (0.227) to the Average lowdin spin population on N1 and N4 in diradical bc_1 (0.339)

Similarly, for **N1-N5**:
When the average spin density is 0.305 (in diradical bc_2) (Table C.6), $2J'_{N1-N5} = 288.52$ cm^{-1}
Now, the true spin density (in isomer 'b-c') is 0.232, so

$$2J_{N1-N5} = \frac{0.232}{0.305} \times 288.52 = 219.46\ cm^{-1}$$

All the calculations are performed in a similar way and the obtained $2J_{Nx-Ny}$ values

(cm^{-1}) are summarised in Table C.7.

Table C.5: Calculated exchange coupling for different possible exchange interactions ($2J'_{Nx-Ny}$) of diradicals bc_1–bc_9.

Diradicals (Interaction)	$\mathbf{2}J'_{Nx-Ny}$
bc_1 (N1-N4)	299.10
bc_2 (N1-N5)	288.52
bc_3 (N1-N6)	-1046.44
bc_4 (N2-N4)	350.72
bc_5 (N2-N5)	356.50
bc_6 (N2-N6)	-1175.44
bc_7 (N3-N4)	-73.20
bc_8 (N3-N5)	-79.86
bc_9 (N3-N6)	296.28

Table C.6: Comparison of average spin density on N-atoms for diradicals bc_1–bc_9 with 'b-c' (average spin density is the average of spin density on the two nitrogen atoms).

Diradicals	Average spin density on nitrogen atoms	
	Diradicals bc_1 - bc_9	**Isomer 'b-c'**
bc_1 (N1-N4)	0.339	0.227
bc_2 (N1-N5)	0.305	0.232
bc_3 (N1-N6)	0.337	0.222
bc_4 (N2-N4)	0.303	0.233
bc_5 (N2-N5)	0.268	0.238
bc_6 (N2-N6)	0.306	0.228
bc_7 (N3-N4)	0.344	0.224
bc_8 (N3-N5)	0.310	0.228
bc_9 (N3-N6)	0.340	0.219

Table C.7: Corrected $2J$ values for different possible individual pairwise exchange interactions in isomer 'b-c'.

Different possible exchange interactions	$\mathbf{2}J_{Nx-Ny}$ ($\mathbf{c}_{xy}$ **x** $\mathbf{2}J'_{Nx-Ny}$)
N1-N4	200.28
N1-N5	219.46
N1-N6	-689.34
N2-N4	269.69
N2-N5	316.59
N2-N6	-875.82
N3-N4	-47.66
N3-N5	-58.73
N3-N6	190.84
Total $2J = \sum 2J_{Nx-Ny}$ = -474.68 cm^{-1}	

C.4 Variation of 2*J* with dihedral angle in isomer 'a-a'

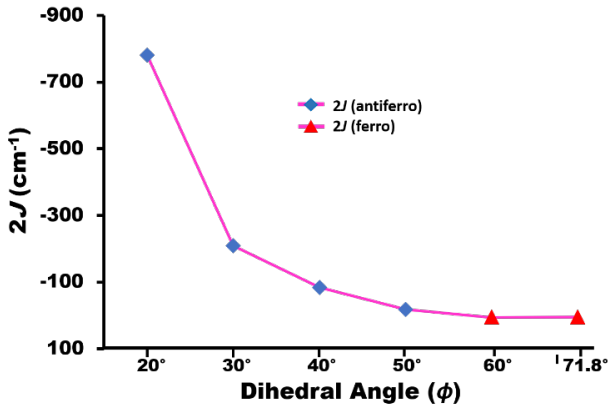

Figure C.5: Variation of 2J with dihedral angle between two radical monomers for 'a-a' isomer.

To verify whether the ferromagnetic exchange in isomer 'a-a' is due to the large dihedral angle, exchange interactions are computed by constraining the dihedral angles for 'a-a'. Ferromagnetic exchange interactions are obtained for the optimized geometry, exhibiting a large dihedral angle of 71.8°. However, constraining the dihedral to smaller angles and thereby making the geometry planar yields antiferromagnetic exchange. Constraint calculations are performed only up to a minimum angle of 20°, as decreasing the angle beyond 20° leads to overlap of two radical monomer units.

APPENDIX D

Appendix-4

D.1 Zwitterionic form of TPHA

The TPHA molecule adopts the zwitterionic configuration in its CSS state with the separation into 10π-anionic and 6π-cationic units. To elucidate this, different charge distribution schemes, including Löwdin, Mulliken and Hirshfeld charge distribution are used and are illustrated in Figure D.1a, D.1b and D.1c.

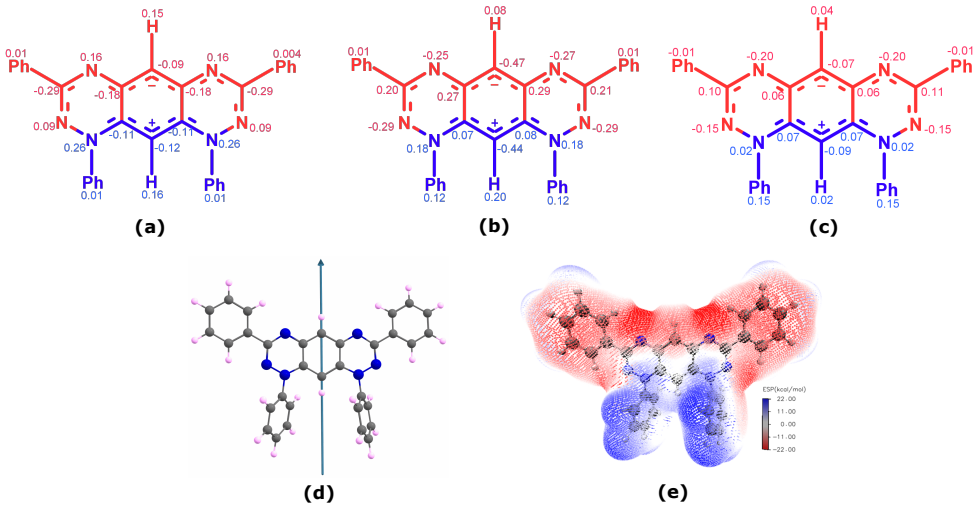

Figure D.1: (a) The Löwdin charge density distribution (b) the Mulliken charge density distribution on different atoms of TPHA obtained at B3LYP/def2-TZVP level (c) Calculated dipole moment of TPHA with the direction of arrow from positive to negative part of the molecule (d) Electrostatic potential mapped on the electron density surface where red indicates negative charge and blue indicates positive charge.

Noteworthy, in this case, the positive and negative charges are not localized on the C1 and C4 only, but are delocalized over the 6π (blue part in Fig D.1a) and 10π parts

(red part in Fig D.1a), therefore, we have taken the summation of the charges on all atoms in the two parts. The summed Löwdin charges on the negative part over all the atoms yield -0.36 a.u. charge. In contrast to this, the summed Löwdin charges on the positive part yield +0.36 a.u. Similarly, the summed Mulliken charges on the positive part is +0.51 a.u. and that on the negative part is -0.50 a.u. The corresponding Hirshfeld charges on the positive and negative parts are -0.42 and +0.41 respectively. Thus, all the considered charge distributions imply the formation of zwitterionic form in the CSS state. Moreover, in Figure D.1d, the dipole moment of the molecule is plotted. Since, the dipole moment orients from positive to negative direction, it highlights the existence of positive and negative parts in the TPHA marking the zwitterionic state in the molecule. The electrostatic potential mapped on the electron density surface is also in favor of the zwitterionic ground state with separation of positive and negative parts (Figure D.1e). Thus, TPHA adopts the zwitterionic ground state in its CSS state.

D.2 Effect of length of coupler

D.2.1 Energetics comparison of different molecules

The molecules **6.1** to **6.6** are optimized in closed-shell singlet (CSS), open-shell singlet (OSS) and triplet (T) state. The optimized energies are collected in Table D.1.

Table D.1: DFT optimized energies (Eh) of molecules **6.1-6.6** in CSS, OSS and T states.

Molecules	**Energies(Eh)**		
	CSS	**OSS**	**T**
6.1	-1560.731910	-1560.731940	-1560.703722
6.2	-1714.320011	-1714.320450	-1714.306505
6.3	-1867.905945	-1867.909631	-1867.902685
6.4	-2021.491373	-2021.499045	-2021.495837
6.5	-2175.076950	-2175.085557	-2175.086306
6.6	-2328.664387	-2328.678135	-2328.680267

The relative energies of all the molecules referred to closed-shell states are given in Table D.2. From the relative energies, it is inferred that molecule **6.1** and **6.2** are stabilized in CSS state whereas molecule **6.3** and **6.4** are in OSS state. Molecules **6.5** and **6.6** possess triplet as ground state.

Table D.2: Relative energies referred to the CSS state for OSS and T states (in meV).

Molecules	**CSS**	**OSS**	**T**
	[E(CSS)-E(CSS)]	**[E(OSS)-E(CSS)]**	**[E(T)-E(CSS)]**
6.1	0.00	0.8	761.07
6.2	0.00	11.85	364.66
6.3	0.00	-99.52	88.1
6.4	0.00	-207.14	-120.52
6.5	0.00	-234.21	-254.59
6.6	0.00	-374.10	-432.12

D.2.2 Energies of molecular orbitals of diradicals 6.5 and 6.6

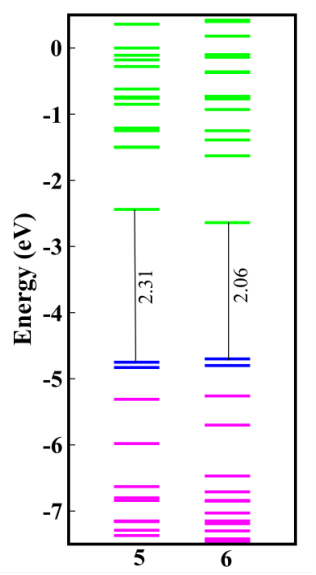

Figure D.2: Molecular orbitals of α-spin electrons of molecules **6.5** and **6.6**. The pink, blue and green colors represent the doubly occupied, singly occupied, and unoccupied orbitals respectively.

The spin-contamination for the diradicals **6.5** and **6.6** in the triplet state is up to 0.36. It is due to increased degeneracy of the molecular orbitals for these diradicals which can be observed from the Figure D.2.

D.2.3 Diradical character index (y) values

To compute the diradical character as proposed by Yamaguchi et al.[271], the occupation numbers of frontier natural orbitals have been taken. Since, there are large number of orbitals with partial occupation number, so instead of considering only the HOMO and LUMO, we have considered the occupation of larger number of orbitals. For molecule **6.1**, we have considered the occupation number of three occupied i.e. HOMO, HOMO-1 and HOMO-2 and three unoccupied i.e., LUMO, LUMO+1, LUMO+2, orbitals since, molecule **6.1** has benzene as coupler with 3π bonds. Further, proceeding towards molecule **2**, since there is addition of one benzene ring, which means addition of 2 π bonds, therefore, we have added two more occupied and unoccupied orbitals respectively. In a similar way, we have increased the two occupied and two unoccupied orbitals with addition of each benzene ring in moving from molecules from **6.3** to **6.6**. Taking the occupation numbers of these orbitals, T i.e., overlap integral is calculated and subsequently put in the equation for y to compute the diradical character index. The y values are collected in Table D.3.

Table D.3: Computed diradical character (y) for molecules **6.1-6.6**.

Molecules	**6.1**	**6.2**	**6.3**	**6.4**	**6.5**	**6.6**
y **value**	0.28	0.53	0.65	0.75	0.78	0.80

D.2.4 Occupation number of HONO and LUNO from CASSCF

The orbital occupation number of HONO and LUNO obtained from CASSCF(10,10) are collected in Table D.4.

Table D.4: Occupation numbers of HONO (n_{HONO}) and LUNO (n_{LUNO}) obtained from CASSCF(10,10).

Molecules	**6.1**	**6.2**	**6.3**	**6.4**	**6.5**	**6.6**
n_{HONO}	1.70	1.42	1.20	1.11	1.06	1.05
n_{LUNO}	0.30	0.58	0.80	0.89	0.94	0.95

The occupation number of LUNO is subsequently increasing from 0.30 for molecule **6.1** to 0.95 for molecule **6.6** indicating an increase in diradical character with larger number of benzene ring in the coupler.

D.2.5 Computation of Head-Gordon Index

To compute the Head-Gordon Index for the molecules **6.1** to **6.6**, the occupation number of orbitals with partial occupancy are taken from CASSCF(10,10). The calculated values are tabulated in Table D.5.

Table D.5: Computed Head-Gordon index ($n_{u,nl}$) for the molecules **6.1-6.6**.

Molecules	**6.1**	**6.2**	**6.3**	**6.4**	**6.5**	**6.6**
$n_{u,nl}$	0.62	1.50	2.05	2.20	2.17	2.21

D.2.6 Energies of frontier molecular orbitals

Table D.6: Energy difference between HOMO and LUMO (in eV) in closed shell singlet (CSS) and SOMO1 and SOMO2 (in eV) in triplet (T) states.

Molecules	**CSS**			**T**		
	E(H)	**E(L)**	Δ**E**$_{HL}$	**E(SOMO1)**	**E(SOMO2)**	Δ**E**$_{SS}$
6.1	-4.91	-2.51	2.40	-5.66	-3.87	1.79
6.2	-4.74	-3.00	1.74	-5.45	-4.23	1.22
6.3	-4.61	-3.36	1.25	-5.28	-4.50	0.78
6.4	-4.53	-3.59	0.94	-5.02	-4.65	0.37
6.5	-4.41	-3.77	0.64	-4.83	-4.75	0.08
6.6	-4.27	-3.88	0.39	-4.81	-4.70	0.11

D.2.7 Computed exchange couplings using BS-DFT

Table D.7: Total energies and calculated exchange coupling constants for the diradicals using **BS-DFT; B3LYP/def2-TZVP** method.

Molecules	**Energy (Eh)**		$2J$**(cm^{-1})**
	$<S^2>_{HS}$	$<S^2>_{BS}$	
6.3	-1867.902685	-1867.909005	-2774.64
	2.04	0.77	
6.4	-2021.495837	-2021.498662	-1240.04
	2.08	0.89	
6.5	-2175.086306	-2175.085557	328.84
	2.21	0.97	
6.6	-2328.680267	-2328.676170	1797.40
	2.36	1.03	

D.2.8 Computed exchange couplings using BS(SF)-DFT

Table D.8: Total energies and calculated exchange coupling constants for the diradicals using **BS(SF)-DFT; B3LYP/def2-TZVP** method.

Molecules	**Energy (Eh)**		$2J$**(cm^{-1})**
	$<S^2>_{HS}$	$<S^2>_{BS}$	
6.3	-1867.902826	-1867.909145	-2773.82
	2.04	0.77	
6.4	-2021.496014	-2021.498838	-1239.46
	2.09	0.89	
6.5	-2021.498838	-2175.087628	306.32
	2.21	0.97	
6.6	-2328.680469	-2328.676379	1795.24
	2.36	1.04	

D.2.9 Computed exchange couplings using SF-TDDFT

Table D.9: Total energies and calculated exchange coupling constants for the diradicals using **SF-TDDFT; BHHLYP/def2-TZVP** method.

Molecules	**Energy (eV)**		$2J(\mathbf{cm}^{-1})$
	$<S^2>_{GS}$	$<S^2>_{ES}$	
6.3	0.544	0.747	-1632.05
	0.43	2.44	
6.4	0.725	0.789	-516.19
	0.79	2.58	
6.5	0.816	0.825	72.59
	2.76	1.23	
6.6	0.304	0.349	362.95
	2.03	1.42	

D.2.10 Spin-decontaminated procedure in BS-DFT

Table D.10: Computed Energies and $<S^2>$ values of diradicals **6.3-6.6** obtained using LSCF method.

Molecules	**6.3**	**6.4**	**6.5**	**6.6**
E(HS,RO)	-1867.898256	-2021.490809	-2175.081286	-2328.659958
	2.00	2.00	2.00	2.00
E(HS,UFM)	-1867.902626	-2021.495750	-2175.087951	-2328.673931
	2.03	2.07	2.19	2.07
E(HS,U)	-1867.902683	-2021.495838	-2175.088171	-2328.680266
	2.04	2.09	2.21	2.36
E(BS,RO)	-1867.897860	-2021.490433	-2175.080655	-2328.652847
	1.00	1.00	1.00	1.00
E(BS,UFC)	-1867.904935	-2021.494454	-2175.082972	-2328.658858
	0.74	0.85	0.91	0.85
E(BS,UFM)	-1867.908868	-2021.498570	-2175.087423	-2328.670617
	0.77	0.88	0.95	1.03
E(BS,U)	-1867.909001	-2021.498655	-2175.087471	-2328.676178
	0.77	0.89	0.97	1.03

Table D.11: Computed different contributions and total magnetic exchange coupling for molecules **6.3-6.6**.

Molecule	**6.3**	**6.4**	**6.5**	**6.6**
J_o	86.99	82.43	138.47	1560.71
$\Delta\ J_{KE}$	-1253.55	-778.63	-479.27	-1350.85
$\Delta\ J_{CP}$	73.16	156.34	447.64	430.07
J_{Other}	-22.43	-6.34	37.55	208.67
J_{Tot}	-1115.82	-546.19	144.40	848.59

D.2.11 Computed exchange couplings using CASSCF and NEVPT2

Table D.12: Total energies and calculated exchange coupling constants for the diradicals using **CASSCF(10,10)** and **CAS(10,10)-NEVPT2** method.

Molecule	E(HS)	E(LS)	$2J(\mathbf{cm}^{-1})$
	CASSCF(10,10)		
6.3	-1857.220625	-1857.222139	-333.08
6.4	-2009.910567	-2009.910832	-58.30
6.5	-2162.595917	-2162.595816	22.38
6.6	-2315.248468	-2315.244718	823.03
	CASSCF(10,10)-NEVPT2		
6.3	-1865.173269	-1865.180321	-1551.44
6.4	-2018.540443	-2018.542475	-447.03
6.5	-2171.908049	-2171.907880	37.10
6.6	-2325.305596	-2325.301267	950.10

D.3 Substituent Effect

D.3.1 Hammett constants of different substituents

Table D.13: Hammett constants $(\sigma_{para})^a$ of different substituents.

Substituents	NMe_2	NH_2	OH	NO_2	CN	CF_3
σ_{para}	-0.83	-0.66	-0.37	0.78	0.66	0.54

[a] Taken from reference[283]

D.3.2 Interplanar angles

Table D.14: Interplanar angles (ϕ_1 and ϕ_2) that EDG and EWG made with the benzene ring respectively in molecules **6.1a-6.1i**.

Molecules	ϕ_1	ϕ_2
6.1a	121.46/121.59	121.18/120.58
6.1b	121.12/120.27	121.49/119.82
6.1c	120.50/120.95	120.06/120.09
6.1d	120.10/120.12	120.64/120.65
6.1e	120.04/120.06	121.15/120.90
6.1f	120.10/120.10	120.07/120.08
6.1g	120.77/118.78	120.66/120.68
6.1h	120.57/118.56	120.54/120.62
6.1i	120.67/118.70	120.11/119.81

D.4 Diradicals with ferromagnetic coupling

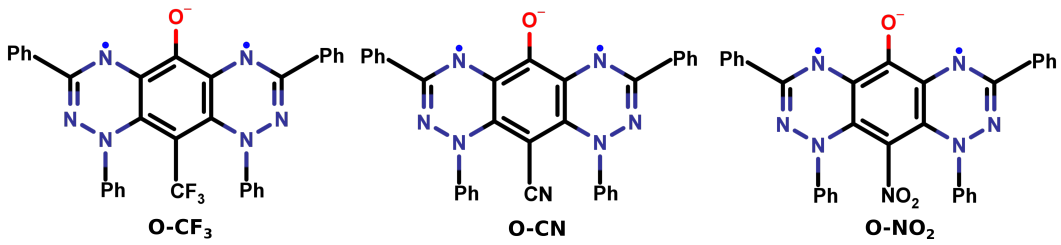

Figure D.3: Diradicals obtained by substituting O^- as EDG and CF_3, CN and NO_2 as EWG.

D.4.1 BS-DFT computed exchange coupling

Table D.15: Total energies and calculated exchange coupling constants for the three diradicals using **BS-DFT; B3LYP/def2-TZVP** method.

Diradical	**Energy (Eh)**		$2J$**(cm^{-1})**
	$<S^2>_{HS}$	$<S^2>_{BS}$	
O-CF_3	-1972.449082	-1972.449082	918.15
	2.03	0.97	
O-CN	-1727.627962	-1727.625439	1107.20
	2.03	0.99	
O-NO_2	-1839.892490	-1839.890909	693.58
	2.03	0.97	

D.4.2 SF-TDDFT computed exchange coupling

Table D.16: Calculated exchange coupling constants for the three diradicals using **SF-TDDFT; BHHLYP/def2-TZVP** method.

Diradical	**Energy (eV)**		$2J$**(cm^{-1})**
	$<S^2>_{GS}$	$<S^2>_{ES}$	
O-CF_3	0.586	0.753	1352.50
	2.25	0.19	
O-CN	0.586	0.769	1471.35
	2.26	0.18	
O-NO_2	0.588	0.728	1130.20
	2.26	0.19	

D.4.3 Occupation number of HONO and LUNO from CASSCF

Table D.17: Occupation number of HONO and LUNO from CASSCF(10,10) for the three diradicals.

Diradical	n_{HONO}	n_{LUNO}
O-CF_3	1.12	0.88
O-CN	1.13	0.87
O-NO_2	1.14	0.86

D.4.4 HOMA values

Table D.18: Calculated HOMA values of the central benzene ring of the three diradicals.

Diradical	**HOMA**
O-CF_3	0.23
O-CN	0.20
O-NO_2	0.21

D.4.5 CASSCF and CASSCF-NEVPT2 computed exchange coupling

Table D.19: Total energies and calculated exchange coupling constants for the three diradicals using **CASSCF(10,10) and CASSCF(10,10)-NEVPT2** method.

Dirad.	**E(HS)**	**E(LS)**	$2J$**(cm^{-1})**
	CASSCF(10,10)		
O-CF_3	-1961.893180	-1961.882709	2298.11
O-CN	-1717.919742	-1717.911172	1880.89
O-NO_2	-1829.695133	-1829.686775	1834.05
	CAS(10,10)-NEVPT2		
O-CF_3	-1969.779120	-1969.778378	162.85
O-CN	-1725.183538	-1725.178368	1134.68
O-NO_2	-1837.331006	-1837.326759	932.10

References

[1] Gatteschi, D.; Sessoli, R.; Villain, J. *Molecular nanomagnets*; Oxford University Press on Demand, 2006; Vol. 5.

[2] Lis, T. Preparation, structure, and magnetic properties of a dodecanuclear mixed-valence manganese carboxylate. *Acta. Crystallogr. B. Struct. Sci. Cryst. Eng. Mater.* **1980**, *36*, 2042–2046.

[3] Sessoli, R.; Gatteschi, D.; Caneschi, A.; Novak, M. Magnetic bistability in a metal-ion cluster. *Nature* **1993**, *365*, 141–143.

[4] Affronte, M.; Troiani, F.; Ghirri, A.; Candini, A.; Evangelisti, M.; Corradini, V.; Carretta, S.; Santini, P.; Amoretti, G.; Tuna, F., et al. Single molecule magnets for quantum computation. *J. Phys. D: Appl. Phys.* **2007**, *40*, 2999–3004.

[5] Gaita-Ariño, A.; Luis, F.; Hill, S.; Coronado, E. Molecular spins for quantum computation. *Nat. Chem.* **2019**, *11*, 301–309.

[6] Hymas, K.; Soncini, A. Molecular spintronics using single-molecule magnets under irradiation. *Phys. Rev. B* **2019**, *99*, 245404.

[7] Dreiser, J.; Wackerlin, C.; Ali, M. E.; Piamonteze, C.; Donati, F.; Singha, A.; Pedersen, K. S.; Rusponi, S.; Bendix, J.; Oppeneer, P. M., et al. Exchange interaction of strongly anisotropic tripodal erbium single-ion magnets with metallic surfaces. *ACS Nano* **2014**, *8*, 4662–4671.

[8] Cavallini, M.; Gomez-Segura, J.; Ruiz-Molina, D.; Massi, M.; Albonetti, C.; Rovira, C.; Veciana, J.; Biscarini, F. Magnetic information storage on polymers by using patterned single-molecule magnets. *Angew. Chem. Int. Ed.* **2005**, *44*, 888–892.

[9] de Camargo, L. C.; Briganti, M.; Santana, F. S.; Stinghen, D.; Ribeiro, R. R.; Nunes, G. G.; Soares, J. F.; Salvadori, E.; Chiesa, M.; Benci, S., et al. Exploring the Organometallic Route to Molecular Spin Qubits: The [CpTi(cot)] Case. *Angew. Chem.* **2021**, *133*, 2620–2625.

[10] Ariciu, A.-M.; Woen, D. H.; Huh, D. N.; Nodaraki, L. E.; Kostopoulos, A. K.; Goodwin, C. A.; Chilton, N. F.; McInnes, E. J.; Winpenny, R. E.; Evans, W. J., et al. Engineering electronic structure to prolong relaxation times in molecular qubits by minimising orbital angular momentum. *Nat. Commun.* **2019**, *10*, 1–8.

[11] Mier, C.; Verlhac, B.; Garnier, L.; Robles, R.; Limot, L.; Lorente, N.; Choi, D.-J. Superconducting scanning tunneling microscope tip to reveal sub-millielectronvolt magnetic energy variations on surfaces. *J. Phys. Chem. Lett.* **2021**, *12*, 2983–2989.

[12] Czap, G.; Wagner, P. J.; Xue, F.; Gu, L.; Li, J.; Yao, J.; Wu, R.; Ho, W. Probing and imaging spin interactions with a magnetic single-molecule sensor. *Science* **2019**, *364*, 670–673.

[13] Verlhac, B.; Bachellier, N.; Garnier, L.; Ormaza, M.; Abufager, P.; Robles, R.; Bocquet, M.-L.; Ternes, M.; Lorente, N.; Limot, L. Atomic-scale spin sensing with a single molecule at the apex of a scanning tunneling microscope. *Science* **2019**, *366*, 623–627.

[14] Milios, C. J.; Winpenny, R. E. Cluster-based single-molecule magnets. *Molecular Nanomagnets and Related Phenomena* **2014**, 1–109.

[15] Feltham, H. L.; Brooker, S. Review of purely 4f and mixed-metal nd-4f single-molecule magnets containing only one lanthanide ion. *Coord. Chem. Rev.* **2014**, *276*, 1–33.

[16] Zadrozny, J. M.; Liu, J.; Piro, N. A.; Chang, C. J.; Hill, S.; Long, J. R. Slow magnetic relaxation in a pseudotetrahedral cobalt(ii) complex with easy-plane anisotropy. *Chem. Commun.* **2012**, *48*, 3927–3929.

[17] Vallejo, J.; Castro, I.; Ruiz-García, R.; Cano, J.; Julve, M.; Lloret, F.; De Munno, G.; Wernsdorfer, W.; Pardo, E. Field-Induced Slow Magnetic Relaxation in a Six-Coordinate Mononuclear Cobalt(II) Complex with a Positive Anisotropy. *J. Am. Chem. Soc.* **2012**, *134*, 15704–15707, PMID: 22963111.

[18] Zabala-Lekuona, A.; Seco, J. M.; Colacio, E. Single-Molecule Magnets: From Mn12-ac to dysprosium metallocenes, a travel in time. *Coord. Chem. Rev.* **2021**, *441*, 213984.

[19] Frost, J. M.; Harriman, K. L.; Murugesu, M. The rise of 3-d single-ion magnets in molecular magnetism: towards materials from molecules? *Chem. Sci.* **2016**, *7*, 2470–2491.

[20] Van Vleck, J. Paramagnetic relaxation times for titanium and chrome alum. *Phys. Rev.* **1940**, *57*, 426.

[21] Orbach, R. Spin-lattice relaxation in rare-earth salts. *Proc. Math. Phys. Eng. Sci. A* **1961**, *264*, 458–484.

[22] Scott, P.; Jeffries, C. Spin-lattice relaxation in some rare-earth salts at helium temperatures; observation of the phonon bottleneck. *Phys. Rev.* **1962**, *127*, 32.

[23] Goodwin, J. C.; Sessoli, R.; Gatteschi, D.; Wernsdorfer, W.; Powell, A. K.; Heath, S. L. Towards nanostructured arrays of single molecule magnets: New Fe_{19} oxyhydroxide clusters displaying high ground state spins and hysteresis. *J. Chem. Soc., Dalton Trans.* **2000**, 1835–1840.

[24] Murugesu, M.; Habrych, M.; Wernsdorfer, W.; Abboud, K. A.; Christou, G. Single-molecule magnets: A Mn_{25} complex with a record S= 51/2 spin for a molecular species. *J. Am. Chem. Soc.* **2004**, *126*, 4766–4767.

[25] Ako, A. M.; Hewitt, I. J.; Mereacre, V.; Clérac, R.; Wernsdorfer, W.; Anson, C. E.; Powell, A. K. A ferromagnetically coupled Mn_{19} aggregate with a record S= 83/2 ground spin state. *Angew. Chem.* **2006**, *118*, 5048–5051.

[26] Kang, S.; Zheng, H.; Liu, T.; Hamachi, K.; Kanegawa, S.; Sugimoto, K.; Shiota, Y.; Hayami, S.; Mito, M.; Nakamura, T., et al. A ferromagnetically coupled Fe_{42} cyanide-bridged nanocage. *Nat. Commun.* **2015**, *6*, 1–6.

[27] Woodruff, D. N.; Winpenny, R. E.; Layfield, R. A. Lanthanide single-molecule magnets. *Chem. Rev.* **2013**, *113*, 5110–5148.

[28] Rinehart, J. D.; Fang, M.; Evans, W. J.; Long, J. R. A N_2^{3-}-radical-bridged terbium complex exhibiting magnetic hysteresis at 14 K. *J. Am. Chem. Soc.* **2011**, *133*, 14236–14239.

[29] Gould, C. A.; Mu, E.; Vieru, V.; Darago, L. E.; Chakarawet, K.; Gonzalez, M. I.; Demir, S.; Long, J. R. Substituent effects on exchange coupling and magnetic relaxation in 2, 2'-bipyrimidine radical-bridged dilanthanide complexes. *J. Am. Chem. Soc.* **2020**, *142*, 21197–21209.
[30] Benner, F.; Demir, S. Isolation of the elusive bisbenzimidazole Bbim 3-˙ radical anion and its employment in a metal complex. *Chem. Sci.* **2022**, 5818–5829.
[31] Blagg, R. J.; Ungur, L.; Tuna, F.; Speak, J.; Comar, P.; Collison, D.; Wernsdorfer, W.; McInnes, E. J.; Chibotaru, L. F.; Winpenny, R. E. Magnetic relaxation pathways in lanthanide single-molecule magnets. *Nat. Chem.* **2013**, *5*, 673–678.
[32] Blagg, R. J.; Tuna, F.; McInnes, E. J.; Winpenny, R. E. Pentametallic lanthanide-alkoxide square-based pyramids: high energy barrier for thermal relaxation in a holmium single molecule magnet. *Chem. Commun.* **2011**, *47*, 10587–10589.
[33] Blagg, R. J.; Muryn, C. A.; McInnes, E. J.; Tuna, F.; Winpenny, R. E. Single pyramid magnets: Dy_5 pyramids with slow magnetic relaxation to 40 K. *Angew. Chem.* **2011**, *123*, 6660–6663.
[34] Cirera, J.; Ruiz, E.; Alvarez, S.; Neese, F.; Kortus, J. How to build molecules with large magnetic anisotropy. *Chem. Eur. J.* **2009**, *15*, 4078–4087.
[35] Milios, C. J.; Inglis, R.; Vinslava, A.; Bagai, R.; Wernsdorfer, W.; Parsons, S.; Perlepes, S. P.; Christou, G.; Brechin, E. K. Toward a magnetostructural correlation for a family of Mn_6 SMMs. *J. Am. Chem. Soc.* **2007**, *129*, 12505–12511.
[36] Neese, F.; Pantazis, D. A. What is not required to make a single molecule magnet. *Faraday discussions* **2011**, *148*, 229–238.
[37] Ishikawa, N.; Sugita, M.; Ishikawa, T.; Koshihara, S.-y.; Kaizu, Y. Lanthanide double-decker complexes functioning as magnets at the single-molecular level. *J. Am. Chem. Soc.* **2003**, *125*, 8694–8695.
[38] Briganti, M.; Lucaccini, E.; Chelazzi, L.; Ciattini, S.; Sorace, L.; Sessoli, R.; Totti, F.; Perfetti, M. Magnetic anisotropy trends along a full 4f-series: The f^{n+7} effect. *J. Am. Chem. Soc.* **2021**, *143*, 8108–8115.
[39] Pedersen, K. S.; Sigrist, M.; Sørensen, M. A.; Barra, A.-L.; Weyhermüller, T.; Piligkos, S.; Thuesen, C. A.; Vinum, M. G.; Mutka, H.; Weihe, H., et al. $[ReF_6]^{2-}$: A Robust module for the design of molecule-based magnetic materials. *Angew. Chem.* **2014**, *126*, 1375–1378.
[40] McClain, K. R.; Gould, C. A.; Chakarawet, K.; Teat, S. J.; Groshens, T. J.; Long, J. R.; Harvey, B. G. High-temperature magnetic blocking and magnetostructural correlations in a series of dysprosium (III) metallocenium single-molecule magnets. *Chem. Sci.* **2018**, *9*, 8492–8503.
[41] Tang, J.; Zhang, P. *Lanthanide single molecule magnets*; Springer, 2015.
[42] Marin, R.; Brunet, G.; Murugesu, M. Shining new light on multifunctional lanthanide single-molecule magnets. *Angew. Chem. Int. Ed.* **2021**, *60*, 1728–1746.
[43] Goodwin, C. A.; Ortu, F.; Reta, D.; Chilton, N. F.; Mills, D. P. Molecular magnetic hysteresis at 60 kelvin in dysprosocenium. *Nature* **2017**, *548*, 439–442.
[44] Guo, F.-S.; Day, B. M.; Chen, Y.-C.; Tong, M.-L.; Mansikkamäki, A.; Layfield, R. A. Magnetic hysteresis up to 80 kelvin in a dysprosium metallocene single-molecule magnet. *Science* **2018**, *362*, 1400–1403.
[45] Rinehart, J. D.; Long, J. R. Exploiting single-ion anisotropy in the design of f-element single-molecule magnets. *Chem. Sci.* **2011**, *2*, 2078–2085.

[46] Craig, G. A.; Murrie, M. 3d single-ion magnets. *Chem. Soc. Rev.* **2015**, *44*, 2135–2147.

[47] Perlepe, P. S.; Maniaki, D.; Pilichos, E.; Katsoulakou, E.; Perlepes, S. P. Smart ligands for efficient 3d-, 4d-and 5d-metal single-molecule magnets and single-ion magnets. *Inorganics* **2020**, *8*, 39.

[48] Gómez-Coca, S.; Aravena, D.; Morales, R.; Ruiz, E. Large magnetic anisotropy in mononuclear metal complexes. *Coord. Chem. Rev.* **2015**, *289*, 379–392.

[49] Reiff, W. M.; LaPointe, A. M.; Witten, E. H. Virtual free ion magnetism and the absence of Jahn- Teller distortion in a linear two-coordinate complex of high-spin iron (II). *J. Am. Chem. Soc.* **2004**, *126*, 10206–10207.

[50] Power, P. P. Stable two-coordinate, open-shell (d^1–d^9) transition metal complexes. *Chem. Rev.* **2012**, *112*, 3482–3507.

[51] Atanasov, M.; Aravena, D.; Suturina, E.; Bill, E.; Maganas, D.; Neese, F. First principles approach to the electronic structure, magnetic anisotropy and spin relaxation in mononuclear 3d-transition metal single molecule magnets. *Coord. Chem. Rev.* **2015**, *289*, 177–214.

[52] Poggini, L.; Tancini, E.; Danieli, C.; Sorrentino, A. L.; Serrano, G.; Lunghi, A.; Malavolti, L.; Cucinotta, G.; Barra, A.-l.; Juhin, A., et al. Engineering chemisorption of Fe_4 single-molecule magnets on gold. *Adv. Mater. Interfaces* **2021**, *8*, 2101182.

[53] Mossin, S.; Tran, B. L.; Adhikari, D.; Pink, M.; Heinemann, F. W.; Sutter, J.; Szilagyi, R. K.; Meyer, K.; Mindiola, D. J. A mononuclear Fe (III) single molecule magnet with a 3/2 - 5/2 spin crossover. *J. Am. Chem. Soc.* **2012**, *134*, 13651–13661.

[54] Yao, B.; Singh, M. K.; Deng, Y.-F.; Wang, Y.-N.; Dunbar, K. R.; Zhang, Y.-Z. Trigonal prismatic cobalt (II) single-ion magnets: Manipulating the magnetic relaxation through symmetry control. *Inorg. Chem.* **2020**, *59*, 8505–8513.

[55] Tripathi, S.; Vaidya, S.; Ahmed, N.; Klahn, E. A.; Cao, H.; Spillecke, L.; Koo, C.; Spachmann, S.; Klingeler, R.; Rajaraman, G., et al. Structure-property correlation in stabilizing axial magnetic anisotropy in octahedral Co (II) complexes. *Cell Rep. Phys. Sci.* **2021**, *2*, 100404.

[56] Feng, X.; Hwang, S. J.; Liu, J.-L.; Chen, Y.-C.; Tong, M.-L.; Nocera, D. G. Slow magnetic relaxation in intermediate spin S= 3/2 mononuclear Fe(III) complexes. *J. Am. Chem. Soc.* **2017**, *139*, 16474–16477.

[57] Chowdhury, S. R.; Mishra, S. Large magnetic anisotropy in linear Co^{II} complexes - Ab initio investigation of the roles of ligand field, structural distortion, and conformational dynamics. *Eur. J. Inorg. Chem.* **2017**, *659*, 668.

[58] Yao, X.-N.; Du, J.-Z.; Zhang, Y.-Q.; Leng, X.-B.; Yang, M.-W.; Jiang, S.-D.; Wang, Z.-X.; Ouyang, Z.-W.; Deng, L.; Wang, B.-W., et al. Two-coordinate Co(II) imido complexes as outstanding single-molecule magnets. *J. Am. Chem. Soc.* **2017**, *139*, 373–380.

[59] Nain, S.; Khurana, R.; Ali, M. E. Harnessing colossal magnetic anisotropy in sandwiched $3d^2$-metallocenes. *J. Phys. Chem. A* **2022**, *126*, 2811–2817.

[60] Errulat, D.; Harriman, K. L.; Gálico, D. A.; Ovens, J. S.; Mansikkamäki, A.; Murugesu, M. Aufbau vs. non-Aufbau ground states in two-coordinate d^7 single-molecule magnets. *Inorg. Chem. Front.* **2021**, *8*, 5076–5085.

[61] Sarkar, A.; Dey, S.; Rajaraman, G. Role of coordination number and geometry in controlling the magnetic anisotropy in Fe(II), Co(II), and Ni(II) single-ion magnets. *Chem. Eur. J.* **2020**, *26*, 14036–14058.

[62] Zadrozny, J. M.; Atanasov, M.; Bryan, A. M.; Lin, C.-Y.; Rekken, B. D.; Power, P. P.; Neese, F.; Long, J. R. Slow magnetization dynamics in a series of two-coordinate iron (II) complexes. *Chem. Sci.* **2013**, *4*, 125–138.

[63] Atanasov, M.; Zadrozny, J. M.; Long, J. R.; Neese, F. A theoretical analysis of chemical bonding, vibronic coupling, and magnetic anisotropy in linear iron (II) complexes with single-molecule magnet behavior. *Chem. Sci.* **2013**, *4*, 139–156.

[64] Bunting, P. C.; Atanasov, M.; Damgaard-Møller, E.; Perfetti, M.; Crassee, I.; Orlita, M.; Overgaard, J.; van Slageren, J.; Neese, F.; Long, J. R. A linear cobalt (II) complex with maximal orbital angular momentum from a non-Aufbau ground state. *Science* **2018**, *362*, eaat7319.

[65] Gütlich, P.; Goodwin, H. A.; Garcia, Y. *Spin crossover in transition metal compounds I*; Springer Science & Business Media, 2004; Vol. 1.

[66] Gütlich, P.; Garcia, Y.; Goodwin, H. A. Spin crossover phenomena in Fe(II) complexes. *Chem. Soc. Rev.* **2000**, *29*, 419–427.

[67] Marchivie, M.; Guionneau, P.; Howard, J. A. K.; Chastanet, G.; Létard, J.-F.; Goeta, A. E.; Chasseau, D. Structural characterization of a photoinduced molecular switch. *J. Am. Chem. Soc.* **2002**, *124*, 194–195.

[68] Bousseksou, A.; Molnár, G.; Tuchagues, J.-P.; Menéndez, N.; Épiphane Codjovi,; Varret, F. Triggering the spin-crossover of $Fe(phen)_2(NCS)_2$ by a pressure pulse. Pressure and magnetic field induce mirror effects. *C R Chim* **2003**, *6*, 329–335.

[69] Ali, M. E.; Staemmler, V.; Illas, F.; Oppeneer, P. M. Designing the redox-driven switching of ferro- to antiferromagnetic couplings in organic diradicals. *J. Chem. Theory Comput.* **2013**, *9*, 5216–5220.

[70] Rudavskyi, A.; Sousa, C.; de Graaf, C.; Havenith, R. W. A.; Broer, R. Computational approach to the study of thermal spin crossover phenomena. *J. Chem. Phys.* **2014**, *140*, 184318.

[71] Raymo, F. M. Digital processing and communication with molecular switches. *Adv. Mater.* **2002**, *14*, 401–414.

[72] Aravena, D.; Ruiz, E. Spin dynamics in single-molecule magnets and molecular qubits. *Dalton Trans.* **2020**, *49*, 9916–9928.

[73] Viciano Chumillas, M.; Blondin, G.; Krzystek, J.; Ozerov, M.; Armentano, D.; Schnegg, A.; Lohmiller, T.; Telser, J.; Lloret, F.; Cano, J. Single-ion magnetic behaviour in an iron(III) porphyrin complex: A dichotomy between high-spin and 5/2–3/2 spin admixture. *Chem. Euro. J.* **2020**, *26*, 14242–14251.

[74] Stavretis, S. E.; Atanasov, M.; Podlesnyak, A. A.; Hunter, S. C.; Neese, F.; Xue, Z.-L. Magnetic transitions in iron porphyrin halides by inelastic neutron scattering and ab initio studies of zero-field splittings. *Inorg. Chem.* **2015**, *54*, 9790–9801.

[75] Miller, J. S.; Calabrese, J. C.; Rommelmann, H.; Chittipeddi, S. R.; Zhang, J. H.; Reiff, W. M.; Epstein, A. J. Ferromagnetic behavior of [Fe (C5Me5) 2]+. bul.[TCNE]-. bul.. Structural and magnetic characterization of decamethylferrocenium tetracyanoethenide,[Fe (C5Me5) 2]+. bul.[TCNE]-. bul.. cntdot.

MeCN and decamethylferrocenium pentacyanopropenide,[Fe (C5Me5) 2]+. bul.[C3 (CN) 5]-. *J. Am. Chem. Soc.* **1987**, *109*, 769–781.

[76] Ratera, I.; Veciana, J. Playing with organic radicals as building blocks for functional molecular materials. *Chem. Soc. Rev.* **2012**, *41*, 303–349.

[77] Hicks, R. G. What's new in stable radical chemistry? *Org. Biomol. Chem.* **2007**, *5*, 1321–1338.

[78] Gomberg, M. An instance of trivalent carbon: Triphenylmethyl. *J. Am. Chem. Soc.* **1900**, *22*, 757–771.

[79] Ballester, M.; Riera-Figueras, J.; Castaner, J.; Badfa, C.; Monso, J. M. Inert carbon free radicals. I. Perchlorodiphenylmethyl and perchlorotriphenylmethyl radical series. *J. Am. Chem. Soc.* **1971**, *93*, 2215–2225.

[80] Lebedev, O.; Kazarnovskii, S. Catalytic oxidation of aliphatic amines with hydrogen peroxide. *Zh. Obshch. Khim* **1960**, *30*, 1631–1635.

[81] Altwicker, E. R. The chemistry of stable phenoxy radicals. *Chem. Rev.* **1967**, *67*, 475–531.

[82] Kinoshita, M. p-nitrophenyl nitronyl nitroxide: the first organic ferromagnet. *Philos. Trans. Royal Soc. A* **1999**, *357*, 2855–2872.

[83] Blatter, H. M.; Lukaszewski, H. A new stable free radical. *Tetrahedron Lett.* **1968**, *9*, 2701–2705.

[84] Constantinides, C. P.; Koutentis, P. A.; Krassos, H.; Rawson, J. M.; Tasiopoulos, A. J. Characterization and Magnetic Properties of a "Super Stable" Radical 1, 3-Diphenyl-7-trifluoromethyl-1, 4-dihydro-1, 2, 4-benzotriazin-4-yl. *J. Org. Chem.* **2011**, *76*, 2798–2806.

[85] Kaszyński, P.; Constantinides, C. P.; Young Jr, V. G. The Planar Blatter Radical: Structural Chemistry of 1, 4-Dihydrobenzo [e][1, 2, 4] triazin-4-yls. *Angew. Chem.* **2016**, *55*, 11149–11152.

[86] Abe, M. Diradicals. *Chem. Rev.* **2013**, *113*, 7011–7088.

[87] Zeng, Z.; Shi, X.; Chi, C.; Navarrete, J. T. L.; Casado, J.; Wu, J. Pro-aromatic and anti-aromatic π-conjugated molecules: an irresistible wish to be diradicals. *Chem. Soc. Rev.* **2015**, *44*, 6578–6596.

[88] Ovchinnikov, A. A. Multiplicity of the ground state of large alternant organic molecules with conjugated bonds. *Theor. Chim. Acc.* **1978**, *47*, 297–304.

[89] Shil, S.; Misra, A. Photoinduced antiferromagnetic to ferromagnetic crossover in organic systems. *J. Phys. Chem. A* **2009**, *114*, 2022–2027.

[90] Sinha, B.; Ramasesha, S. Direct versus kinetic exchange in multiband models for organic ferromagnetism. *Phys. Rev. B* **1993**, *48*, 16410.

[91] Pal, A. K.; Mañeru, D. R.; Latif, I. A.; de PR Moreira, I.; Illas, F.; Datta, S. N. Theoretical and computational investigation of meta-phenylene as ferromagnetic coupler in nitronyl nitroxide diradicals. *Theor. Chem. Acc.* **2014**, *133*, 1–12.

[92] Gallagher, N. M.; Olankitwanit, A.; Rajca, A. High-spin organic molecules. *J. Org. Chem.* **2015**, *80*, 1291–1298.

[93] Fang, S.; Lee, M.-S.; Hrovat, D. A.; Borden, W. T. Ab initio calculations show why m-phenylene is not always a ferromagnetic coupler. *J. Am. Chem. Soc.* **1995**, *117*, 6727–6731.

[94] Zhang, J.; Zhang, H.; Wang, L.; Wang, R.; Wang, L. Effect of configuration and conformation on the spin multiplicity in xylylene type biradicals. *Sci. China, Ser. B: Chem.* **2000**, *43*, 524–530.

[95] Latif, I. A.; Hansda, S.; Datta, S. N. High magnetic exchange coupling constants: a density functional theory based study of substituted Schlenk diradicals. *J. Phys. Chem. A* **2012**, *116*, 8599–8607.

[96] Burnea, F. K. B.; Nam, Y.; Lee, J. Y. H-Bonding on spin centres enhances spin–spin coupling for organic diradicals. *J. Mater. Chem. C* **2020**, *8*, 3402–3408.

[97] Calder, A.; Forrester, A. R.; James, P. G.; Luckhurst, G. R. Nitroxide radicals. V. N,N'-Di-tert-butyl-m-phenylenebinitroxide, a stable triplet. *J. Am. Chem. Soc.* **1969**, *91*, 3724–3727.

[98] Rajca, A.; Takahashi, M.; Pink, M.; Spagnol, G.; Rajca, S. Conformationally Constrained, Stable, Triplet Ground State (S = 1) Nitroxide Diradicals. Antiferromagnetic Chains of S = 1 Diradicals. *J. Am. Chem. Soc.* **2007**, *129*, 10159–10170, PMID: 17655296.

[99] Tretyakov, E. V.; Zhivetyeva, S. I.; Petunin, P. V.; Gorbunov, D. E.; Gritsan, N. P.; Bagryanskaya, I. Y.; Bogomyakov, A. S.; Postnikov, P. S.; Kazantsev, M. S.; Trusova, M. E., et al. Ferromagnetically coupled S= 1 chains in crystals of verdazyl-nitronyl nitroxide diradicals. *Angew. Chem. Int. Ed.* **2020**, *59*, 20704–20710.

[100] Fedyushin, P.; Rybalova, T.; Asanbaeva, N.; Bagryanskaya, E.; Dmitriev, A.; Gritsan, N.; Kazantsev, M.; Tretyakov, E. Synthesis of nitroxide diradical using a new approach. *Molecules* **2020**, *25*, 2701.

[101] Ali, M. E.; Datta, S. N. Density functional theory prediction of enhanced photomagnetic properties of nitronyl nitroxide and imino nitroxide diradicals with substituded dihydropyrene couplers. *J. Phys. Chem. A* **2006**, *110*, 10525–10527.

[102] Dressler, J. J.; Valdivia, A. C.; Kishi, R.; Rudebusch, G. E.; Ventura, A. M.; Chastain, B. E.; Gómez-García, C. J.; Zakharov, L. N.; Nakano, M.; Casado, J., et al. Diindenoanthracene diradicaloids enable rational, incremental tuning of their singlet-triplet energy gaps. *Chem* **2020**, *6*, 1353–1368.

[103] Chen, Z.; Li, Y.; Huang, F. Persistent and stable organic radicals: design, synthesis, and applications. *Chem* **2021**, *7*, 288–332.

[104] Gallagher, N. M.; Bauer, J. J.; Pink, M.; Rajca, S.; Rajca, A. High-spin organic diradical with robust stability. *J. Am. Chem. Soc.* **2016**, *138*, 9377–9380.

[105] Gallagher, N.; Zhang, H.; Junghoefer, T.; Giangrisostomi, E.; Ovsyannikov, R.; Pink, M.; Rajca, S.; Casu, M. B.; Rajca, A. Thermally and magnetically robust triplet ground state diradical. *J. Am. Chem. Soc.* **2019**, *141*, 4764–4774.

[106] Zhang, S.; Pink, M.; Junghoefer, T.; Zhao, W.; Hsu, S.-N.; Rajca, S.; Calzolari, A.; Boudouris, B. W.; Casu, M. B.; Rajca, A. High-Spin (S = 1) Blatter-Based Diradical with Robust Stability and Electrical Conductivity. *J. Am. Chem. Soc.* **2022**, *144*, 6059–6070.

[107] Zhang, Y.; Zheng, Y.; Zhou, H.; Miao, M.-S.; Wudl, F.; Nguyen, T.-Q. Temperature Tunable Self-Doping in Stable Diradicaloid Thin-Film Devices. *Adv. Mater.* **2015**, *27*, 7412–7419.

[108] Hu, X.; Chen, H.; Zhao, L.; Miao, M.-s.; Zheng, X.; Zheng, Y. Nitrogen-coupled blatter diradicals: the fused versus unfused bridges. *J. Mater. Chem. C* **2019**, *7*, 10460–10464.

[109] Hu, X.; Chen, H.; Zhao, L.; Miao, M.; Han, J.; Wang, J.; Guo, J.; Hu, Y.; Zheng, Y. Nitrogen analogues of Chichibabin's and Müller's hydrocarbons with small singlet–triplet energy gaps. *Chem. Commun.* **2019**, *55*, 7812–7815.

[110] Hu, X.; Chen, H.; Xue, G.; Zheng, Y. Correlation between the strength of conjugation and spin–spin interactions in stable diradicaloids. *J. Mater. Chem. C* **2020**, *8*, 10749–10754.
[111] Thiele, J.; Balhorn, H. Ueber einen chinoïden Kohlenwasserstoff. *Ber. Dtsch. Chem. Ges.* **1904**, *37*, 1463–1470.
[112] Tschitschibabin, A. Über einige phenylierte Derivate des p, p-Ditolyls. *Ber. Dtsch. Chem. Ges.* **1907**, *40*, 1810–1819.
[113] Kubo, T.; Shimizu, A.; Sakamoto, M.; Uruichi, M.; Yakushi, K.; Nakano, M.; Shiomi, D.; Sato, K.; Takui, T.; Morita, Y., et al. Synthesis, intermolecular interaction, and semiconductive behavior of a delocalized singlet biradical hydrocarbon. *Angew. Chem. Int. Ed.* **2005**, *44*, 6564–6568.
[114] Shimizu, A.; Kubo, T.; Uruichi, M.; Yakushi, K.; Nakano, M.; Shiomi, D.; Sato, K.; Takui, T.; Hirao, Y.; Matsumoto, K., et al. Alternating covalent bonding interactions in a one-dimensional chain of a phenalenyl-based singlet biradical molecule having Kekulé structures. *J. Am. Chem. Soc.* **2010**, *132*, 14421–14428.
[115] Casado, J. *Physical Organic Chemistry of Quinodimethanes*; Springer, 2017; pp 209–248.
[116] Rudebusch, G. E.; Zafra, J. L.; Jorner, K.; Fukuda, K.; Marshall, J. L.; Arrechea-Marcos, I.; Espejo, G. L.; Ortiz, R. P.; Gómez-García, C. J.; Zakharov, L. N., et al. Diindeno-fusion of an anthracene as a design strategy for stable organic biradicals. *Nat. Chem.* **2016**, *8*, 753–759.
[117] Frederickson, C. K.; Rose, B. D.; Haley, M. M. Explorations of the indenofluorenes and expanded quinoidal analogues. *Acc. Chem. Res.* **2017**, *50*, 977–987.
[118] Zeng, W.; Sun, Z.; Herng, T. S.; Gonçalves, T. P.; Gopalakrishna, T. Y.; Huang, K.-W.; Ding, J.; Wu, J. Super-heptazethrene. *Angew. Chem. Int. Ed.* **2016**, *55*, 8615–8619.
[119] Konishi, A.; Hirao, Y.; Kurata, H.; Kubo, T.; Nakano, M.; Kamada, K. Anthenes: Model systems for understanding the edge state of graphene nanoribbons. *Pure Appl. Chem.* **2014**, *86*, 497–505.
[120] Rudebusch, G. E.; Zafra, J. L.; Jorner, K.; Fukuda, K.; Marshall, J. L.; Arrechea-Marcos, I.; Espejo, G. L.; Ponce Ortiz, R.; Gomez-Garcia, C. J.; Zakharov, L. N., et al. Diindeno-fusion of an anthracene as a design strategy for stable organic biradicals. *Nat. Chem.* **2016**, *8*, 753–759.
[121] Thomas, L. H. The calculation of atomic fields. Math. Proc. Camb. Philos. Soc. 1927; pp 542–548.
[122] Hohenberg, P.; Kohn, W. Density functional theory (DFT). *Phys. Rev.* **1964**, *136*, B864.
[123] Kohn, W.; Sham, L. J. Self-consistent equations including exchange and correlation effects. *Phys. Rev.* **1965**, *140*, A1133.
[124] Dirac, P. A. M. Quantised singularities in the electromagnetic field. *Proc. Math. Phys. Eng. Sci.* **1931**, *133*, 60–72.
[125] Becke, A. D. Perspective: Fifty years of density-functional theory in Chem. Phys. *J. Chem. Phys.* **2014**, *140*, 18A301.
[126] Noodleman, L. Valence bond description of antiferromagnetic coupling in transition metal dimers. *J. Chem. Phys.* **1981**, *74*, 5737–5743.

[127] Ruiz, E.; Cano, J.; Alvarez, S.; Alemany, P. Broken symmetry approach to calculation of exchange coupling constants for homobinuclear and heterobinuclear transition metal complexes. *J. Comput. Chem.* **1999**, *20*, 1391–1400.
[128] Caballol, R.; Castell, O.; Illas, F.; de PR Moreira, I.; Malrieu, J. Remarks on the proper use of the broken symmetry approach to magnetic coupling. *J. Phys. Chem. A* **1997**, *101*, 7860–7866.
[129] Ginsberg, A. Magnetic exchange in transition metal complexes. 12. Calculation of cluster exchange coupling constants with the X. alpha.-scattered wave method. *J. Am. Chem. Soc.* **1980**, *102*, 111–117.
[130] Noodleman, L. Valence bond description of antiferromagnetic coupling in transition metal dimers. *J. Chem. Phys.* **1981**, *74*, 5737–5743.
[131] Noodleman, L.; Davidson, E. R. Ligand spin polarization and antiferromagnetic coupling in transition metal dimers. *Chem. Phys.* **1986**, *109*, 131–143.
[132] Bencini, A.; Totti, F.; Daul, C. A.; Doclo, K.; Fantucci, P.; Barone, V. Density functional calculations of magnetic exchange interactions in polynuclear transition metal complexes. *Inorg. Chem.* **1997**, *36*, 5022–5030.
[133] Martin, R. L.; Illas, F. Antiferromagnetic exchange interactions from hybrid density functional theory. *Phys. Rev. Lett.* **1997**, *79*, 1539.
[134] Nishino, M.; Yamanaka, S.; Yoshioka, Y.; Yamaguchi, K. Theoretical approaches to direct exchange couplings between divalent chromium ions in naked dimers, tetramers, and clusters. *J. Phys. Chem. A* **1997**, *101*, 705–712.
[135] Ferré, N.; Guihéry, N.; Malrieu, J.-P. Spin decontamination of broken-symmetry density functional theory calculations: deeper insight and new formulations. *Phys. Chem. Chem. Phys.* **2015**, *17*, 14375–14382.
[136] David, G.; Trinquier, G.; Malrieu, J.-P. Consistent spin decontamination of broken-symmetry calculations of diradicals. *J. Chem. Phys.* **2020**, *153*, 194107.
[137] Neese, F. The ORCA program system. *Wiley Interdiscip. Rev. Comput. Mol. Sci.* **2012**, *2*, 73–78.
[138] Neese, F.; Wennmohs, F.; Becker, U.; Riplinger, C. The ORCA quantum chemistry program package. *J. Chem. Phys.* **2020**, *152*, 224108.
[139] Kruszewski, J.; Krygowski, T. Definition of aromaticity basing on the harmonic oscillator model. *Tetrahedron Lett.* **1972**, *13*, 3839 – 3842.
[140] Krygowski, T. M.; Cyrański, M. Separation of the energetic and geometric contributions to the aromaticity. Part IV. A general model for the π-electron systems. *Tetrahedron* **1996**, *52*, 10255 – 10264.
[141] Cavallini, M.; Gomez-Segura, J.; Ruiz-Molina, D.; Massi, M.; Albonetti, C.; Rovira, C.; Veciana, J.; Biscarini, F. Magnetic information storage on polymers by using patterned single-molecule magnets. *Angew. Chem.* **1994**, *117*, 910–914.
[142] Affronte, M.; Troiani, F.; Ghirri, A.; Candini, A.; Evangelisti, M.; Radini, V.; Carretta, S.; Santini, P.; Amoretti, G.; Tuna, F., et al. Single molecule magnets for quantum computation. *J. Phys. D: Appl. Phys.* **2007**, *40*, 2999.
[143] Bogani, L.; Wernsdorfer, W. Molecular spintronics using single-molecule magnets. *Nat. Mater.* **2008**, *7*, 179–186.
[144] Corradini, V.; Ghirri, A.; Candini, A.; Biagi, R.; del Pennino, U.; Dotti, G.; Otero, E.; Choueikani, F.; Blagg, R. J.; McInnes, E. J. L., et al. Magnetic cooling at a single molecule level: a spectroscopic investigation of isolated molecules on a surface. *Adv. Mater.* **2013**, *25*, 2816–2820.

[145] Gatteschi, D.; Sessoli, R.; Villain, J. *Molecular Nanomagnets*; Oxford University Press, 2006; Vol. 5.

[146] Ding, Y.-S.; Chilton, N. F.; Winpenny, R. E. P.; Zheng, Y.-Z. On approaching the limit of molecular magnetic anisotropy: A near-perfect pentagonal bipyramidal dysprosium(III) single-molecule magnet. *Angew. Chem., Int. Ed.* **2016**, *55*, 16071–16074.

[147] Randall McClain, K.; Gould, C. A.; Chakarawet, K.; Teat, S. J.; Groshens, T. J.; Long, J. R.; Harvey, B. G. High-temperature magnetic blocking and magneto-structural correlations in a series of dysprosium(III) metallocenium single-molecule magnets. *Chem. Sci.* **2018**, *9*, 8492–8503.

[148] Guo, F.-S.; Day, B. M.; Chen, Y.-C.; Tong, M.-L.; Mansikkamäki, A.; Layfield, R. A. Magnetic hysteresis up to 80 kelvin in a dysprosium metallocene single-molecule magnet. *Science* **2018**, *362*, 1400–1403.

[149] Gupta, S. K.; Shanmugan, S.; Rajeshkumar, T.; Borah, A.; Damjanović, M.; Schulze, M.; Wernsdorfer, W.; Rajaraman, G.; Murugavel, R. A single-ion single-electron cerrous magnet. *Dalton Trans.* **2019**, *48*, 15928–15935.

[150] Gupta, S. K.; Murugavel, R. Enriching lanthanide single-ion magnetism through symmetry and axiality. *Chem. Commun.* **2018**, *54*, 3685–3696.

[151] Kalita, P.; Acharya, J.; Chandrasekhar, V. Mononuclear pentagonal bipyramidal Ln (III) complexes: Syntheses and magnetic properties. *J. Magn. Magn. Mater* **2020**, *498*, 166098.

[152] Singh, S. K.; Cramer, C. J.; Gagliardi, L. Correlating electronic structure and magnetic anisotropy in actinide complexes [An(COT)$_2$], An(III/IV) = U, Np, and Pu. *Inorg. Chem.* **2020**, *59*, 6815–6825.

[153] Gaggioli, C. A.; Gagliardi, L. Theoretical investigation of plutonium-based single-molecule magnets. *Inorg. Chem.* **2018**, *57*, 8098–8105.

[154] Yu, K.-X.; Kragskow, J. G.; Ding, Y.-S.; Zhai, Y.-Q.; Reta, D.; Chilton, N. F.; Zheng, Y.-Z. Enhancing magnetic hysteresis in single-molecule magnets by ligand functionalization. *Chem* **2020**, 1777–1793.

[155] Zheng, Y.-Z.; Ding, Y.-S.; Han, T.; Zhai, Y.-Q.; Reta, D.; Chilton, N. F.; Winpenny, R. E. A study of magnetic relaxation in Dysprosium (III) single-molecule magnets. *Chem. Euro. J.* **2020**, *26*, 5893–5902.

[156] Harman, W. H.; Harris, T. D.; Freedman, D. E.; Fong, H.; Chang, A.; Rinehart, J. D.; Ozarowski, A.; Sougrati, M. T.; Grandjean, F.; Long, G. J., et al. Slow magnetic relaxation in a family of trigonal pyramidal iron(II) pyrrolide complexes. *J. Am. Chem. Soc.* **2010**, *132*, 18115–18126.

[157] Yao, X.-N.; Du, J.-Z.; Zhang, Y.-Q.; Leng, X.-B.; Yang, M.-W.; Jiang, S.-D.; Wang, Z.-X.; Ouyang, Z.-W.; Deng, L.; Wang, B.-W., et al. Two-coordinate Co(II) imido complexes as outstanding single-molecule magnets. *J. Am. Chem. Soc.* **2017**, *139*, 373–380.

[158] Zadrozny, J. M.; Xiao, D. J.; Atanasov, M.; Long, G. J.; Grandjean, F.; Neese, F.; Long, J. R. Magnetic blocking in a linear iron(I) complex. *Nat. Chem.* **2013**, *5*, 577–581.

[159] Mossin, S.; Tran, B. L.; Adhikari, D.; Pink, M.; Heinemann, F. W.; Sutter, J.; Szilagyi, R. K.; Meyer, K.; Mindiola, D. J. A mononuclear Fe(III) single molecule magnet with a 3/2-5/2 spin crossover. *J. Am. Chem. Soc.* **2012**, *134*, 13651–13661.

[160] Feng, X.; Hwang, S. J.; Liu, J.-L.; Chen, Y.-C.; Tong, M.-L.; Nocera, D. G. Slow magnetic relaxation in intermediate spin S = 3/2 mononuclear Fe(III) complexes. *J. Am. Chem. Soc.* **2017**, *139*, 16474–16477.

[161] Roy Chowdhury, S.; Mishra, S. Ab initio investigation of magnetic anisotropy in intermediate spin iron (III) complexes. *J. Chem. Phys.* **2018**, *149*, 234302.

[162] Becke, A. D. A new mixing of Hartree–Fock and local density-functional theories. *J. Chem. Phys.* **1993**, *98*, 1372–1377.

[163] Lee, C.; Yang, W.; Parr, R. G. Development of the Colle-Salvetti correlation-energy formula into a functional of the electron density. *Phys. Rev. B* **1988**, *37*, 785–789.

[164] Weigend, F.; Ahlrichs, R. Balanced basis sets of split valence, triple zeta valence and quadruple zeta valence quality for H to Rn: Design and assessment of accuracy. *Phys. Chem. Chem. Phys.* **2005**, *7*, 3297–3305.

[165] Neese, F.; Wennmohs, F.; Hansen, A.; Becker, U. Efficient, approximate and parallel Hartree-Fock and hybrid DFT calculations. A 'chain-of-spheres' algorithm for the Hartree-Fock exchange. *Chem. Phys.* **2009**, 98–109.

[166] Izsák, R.; Neese, F. An overlap fitted chain of spheres exchange method. *J. Chem. Phys.* **2011**, *135*, 144105.

[167] Weigend, F. Hartree Fock exchange fitting basis sets for H to Rn. *J. Comput. Chem.* **2007**, *29*, 167–175.

[168] Grimme, S.; Antony, J.; Ehrlich, S.; Krieg, H. A consistent and accurate ab initio parametrization of density functional dispersion correction (DFT-D) for the 94 elements H-Pu. *J. Chem. Phys.* **2010**, *132*, 154104.

[169] Grimme, S.; Ehrlich, S.; Goerigk, L. Effect of the damping function in dispersion corrected density functional theory. *J. Comput. Chem.* **2011**, *32*, 1456–1465.

[170] Åke Malmqvist, P.; Roos, B. O. The CASSCF state interaction method. *Chem. Phys. Lett.* **1989**, *155*, 189 – 194.

[171] Angeli, C.; Cimiraglia, R.; Malrieu, J.-P. N-electron valence state perturbation theory: a fast implementation of the strongly contracted variant. *Chem. Phys. Lett.* **2001**, *350*, 297 – 305.

[172] Angeli, C.; Cimiraglia, R.; Evangelisti, S.; Leininger, T.; Malrieu, J.-P. Introduction of n-electron valence states for multireference perturbation theory. *J. Chem. Phys.* **2001**, *114*, 10252–10264.

[173] Mayer, I. Charge, bond order and valence in the ab initio SCF theory. *Chem. Phys. Lett.* **1983**, *97*, 270–274.

[174] Helmich-Paris, B. CASSCF linear response calculations for large open-shell molecules. *J. Chem. Phys.* **2019**, *150*, 174121.

[175] Roemelt, M.; Krewald, V.; Pantazis, D. A. Exchange coupling interactions from the density matrix renormalization group and N-electron valence perturbation theory: Application to a biomimetic mixed-valence manganese complex. *J. Chem. Theory Comput.* **2018**, *14*, 166–179.

[176] Maurice, R.; Bastardis, R.; Graaf, C. d.; Suaud, N.; Mallah, T.; Guihéry, N. Universal theoretical approach to extract anisotropic spin hamiltonians. *J. Chem. Theory Comput.* **2009**, *5*, 2977–2984.

[177] Neese, F. Efficient and accurate approximations to the molecular spin-orbit coupling operator and their use in molecular g-tensor calculations. *J. Chem. Phys.* **2005**, *122*, 034107.

[178] Llanos, L.; Aravena, D. Effect of low spin excited states for magnetic anisotropy of transition metal mononuclear single molecule magnets. *Inorganics* **2018**, *6*, 24.

[179] Maurice, R.; Sivalingam, K.; Ganyushin, D.; Guihéry, N.; de Graaf, C.; Neese, F. Theoretical determination of the zero-field splitting in copper acetate monohydrate. *Inorg. Chem.* **2011**, *50*, 6229–6236.

[180] Reiher, M.; Salomon, O.; Hess, B. A. Reparameterization of hybrid functionals based on energy differences of states of different multiplicity. *Theor. Chem. Acc.* **2001**, *107*, 48–55.

[181] Reiher, M. Theoretical study of the $Fe(phen)_2(NCS)_2$ spin-crossover complex with reparametrized density functionals. *Inorg. Chem.* **2002**, *41*, 6928–6935.

[182] Salomon, O.; Reiher, M.; Hess, B. A. Assertion and validation of the performance of the B3LYP* functional for the first transition metal row and the G2 test set. *J. Chem. Phys.* **2002**, *117*, 4729–4737.

[183] Ye, S.; Neese, F. Accurate modeling of spin-state energetics in spin-crossover systems with modern density functional theory. *Inorg. Chem.* **2010**, *49*, 772–774.

[184] Chowdhury, S. R.; Mishra, S. Heavy ligand atom induced large magnetic anisotropy in Mn (II) complexes. *Phys. Chem. Chem. Phys.* **2017**, *19*, 16914–16922.

[185] Neese, F.; Solomon, E. I. Calculation of zero-field splittings, g-values, and the relativistic nephelauxetic effect in transition metal complexes. Application to high-spin ferric complexes. *Inorg. Chem.* **1998**, *37*, 6568–6582.

[186] Ruamps, R.; Batchelor, L. J.; Maurice, R.; Gogoi, N.; Jiménez-Lozano, P.; Guihéry, N.; de Graaf, C.; Barra, A.-L.; Sutter, J.-P.; Mallah, T. Origin of the magnetic anisotropy in heptacoordinate Ni^{II} and Co^{II} Complexes. *Chem. Euro. J.* **2013**, *19*, 950–956.

[187] Gomez-Coca, S.; Cremades, E.; Aliaga-Alcalde, N.; Ruiz, E. Mononuclear single-molecule magnets: Tailoring the magnetic anisotropy of first-row transition-metal complexes. *J. Am. Chem. Soc.* **2013**, *135*, 7010–7018.

[188] Drahoš, B.; Herchel, R.; Trávníček, Z. Impact of halogenido coligands on magnetic anisotropy in seven-coordinate Co(II) complexes. *Inorg. Chem.* **2017**, *56*, 5076–5088.

[189] Zadrozny, J. M.; Xiao, D. J.; Atanasov, M.; Long, G. J.; Grandjean, F.; Neese, F.; Long, J. R. Magnetic blocking in a linear iron (I) complex. *Nat. Chem.* **2013**, *5*, 577–581.

[190] Zadrozny, J. M.; Xiao, D. J.; Long, J. R.; Atanasov, M.; Neese, F.; Grandjean, F.; Long, G. J. Mossbauer spectroscopy as a probe of magnetization dynamics in the linear iron (I) and iron (II) complexes $[Fe(C(SiMe_3)_3)_2]^{1-/0}$. *Inorg. Chem.* **2013**, *52*, 13123–13131.

[191] Werncke, C. G.; Bunting, P. C.; Duhayon, C.; Long, J. R.; Bontemps, S.; Sabo-Etienne, S. Two-coordinate iron (I) complex $[Fe\{N(SiMe_3)_2\}_2]^-$: Synthesis, properties, and redox activity. *Angew. Chem.* **2015**, *127*, 247–250.

[192] Ouyang, Z.; Du, J.; Wang, L.; Kneebone, J. L.; Neidig, M. L.; Deng, L. Linear and T-shaped iron (I) complexes supported by N-heterocyclic carbene ligands: Synthesis and structure characterization. *Inorg. Chem.* **2015**, *54*, 8808–8816.

[193] Meng, Y.-S.; Ouyang, Z.; Yang, M.-W.; Zhang, Y.-Q.; Deng, L.; Wang, B.-W.; Gao, S. Multiple magnetic relaxation pathways in T-shaped N-heterocyclic

carbene-supported Fe(I) single-ion magnets. *Inorg. Chem. Front.* **2019**, *6*, 1050–1057.

[194] Ni, C.; Ellis, B. D.; Fettinger, J. C.; Long, G. J.; Power, P. P. Univalent transition metal complexes of arenes stabilized by a bulky terphenyl ligand: differences in the stability of Cr(I), Mn(I) or Fe(I) complexes. *Chem. Commun.* **2008**, 1014–1016.

[195] Ung, G.; Rittle, J.; Soleilhavoup, M.; Bertrand, G.; Peters, J. C. Two-coordinate Fe^0 and Co^0 complexes supported by cyclic(alkyl)(amino) carbenes. *Angew. Chem. Int. Ed.* **2014**, *53*, 8427–8431.

[196] Malmqvist, P.-Å.; Roos, B. O. The CASSCF state interaction method. *Chem. Phys. Lett.* **1989**, *155*, 189–194.

[197] Angeli, C.; Cimiraglia, R.; Evangelisti, S.; Leininger, T.; Malrieu, J.-P. Introduction of n-electron valence states for multireference perturbation theory. *J. Chem. Phys.* **2001**, *114*, 10252–10264.

[198] Pantazis, D. A.; Chen, X.-Y.; Landis, C. R.; Neese, F. All-electron scalar relativistic basis sets for third-row transition metal atoms. *J. Chem. Theory Comput.* **2008**, *4*, 908–919.

[199] Stoychev, G. L.; Auer, A. A.; Neese, F. Automatic generation of auxiliary basis sets. *J. Chem. Theory Comput.* **2017**, *13*, 554–562.

[200] Heß, B. A.; Marian, C. M.; Wahlgren, U.; Gropen, O. A mean-field spin-orbit method applicable to correlated wavefunctions. *Chem. Phys. Lett.* **1996**, *251*, 365–371.

[201] Neese, F. Efficient and accurate approximations to the molecular spin-orbit coupling operator and their use in molecular g-tensor calculations. *J. Chem. Phys.* **2005**, *122*, 034107.

[202] Maurice, R.; Bastardis, R.; Graaf, C. d.; Suaud, N.; Mallah, T.; Guihery, N. Universal theoretical approach to extract anisotropic spin hamiltonians. *J. Chem. Theory Comput.* **2009**, *5*, 2977–2984.

[203] Atanasov, M.; Ganyushin, D.; Sivalingam, K.; Neese, F. In *Molecular Electronic Structures of Transition Metal Complexes II*; Mingos, D. M. P., Day, P., Dahl, J. P., Eds.; Springer Berlin Heidelberg: Berlin, Heidelberg, 2012; pp 149–220.

[204] Chibotaru, L. F.; Ungur, L. Ab initio calculation of anisotropic magnetic properties of complexes. I. Unique definition of pseudospin Hamiltonians and their derivation. *J. Chem. Phys.* **2012**, *137*, 064112.

[205] Ungur, L.; Chibotaru, L. F. Ab initio crystal field for lanthanides. *Chem. Eur. J.* **2017**, *23*, 3708–3718.

[206] Escalera-Moreno, L.; Suaud, N.; Gaita-Ariño, A.; Coronado, E. Determining key local vibrations in the relaxation of molecular spin qubits and single-molecule magnets. *J. Phys. Chem. Lett.* **2017**, *8*, 1695–1700, PMID: 28350165.

[207] Fdez. Galvan, I.; Vacher, M.; Alavi, A.; Angeli, C.; Aquilante, F.; Autschbach, J.; Bao, J. J.; Bokarev, S. I.; Bogdanov, N. A.; Carlson, R. K., et al. OpenMolcas: From source code to insight. *J. Chem. Theory Comput.* **2019**, *15*, 5925–5964.

[208] Aquilante, F.; Autschbach, J.; Baiardi, A.; Battaglia, S.; Borin, V. A.; Chibotaru, L. F.; Conti, I.; De Vico, L.; Delcey, M.; Fdez. Galván, I., et al. Modern quantum chemistry with [Open]Molcas. *J. Chem. Phys.* **2020**, *152*, 214117.

[209] Roos, B. O.; Lindh, R.; Malmqvist, P.-Å.; Veryazov, V.; Widmark, P.-O. New Relativistic ANO Basis Sets for Transition Metal Atoms. *J. Phys. Chem. A* **2005**, *109*, 6575–6579.

[210] Aquilante, F.; Pedersen, T. B.; Veryazov, V.; Lindh, R. MOLCAS—a software for multiconfigurational quantum chemistry calculations. *Wiley Interdiscip. Rev. Comput. Mol. Sci.* **2013**, *3*, 143–149.

[211] Damgaard-Møller, E.; Krause, L.; Lassen, H.; Malaspina, L. A.; Grabowsky, S.; Bamberger, H.; McGuire, J.; Miras, H. N.; Sproules, S.; Overgaard, J. Investigating complex magnetic anisotropy in a Co(II) molecular compound: A charge density and correlated ab initio electronic structure study. *Inorg. Chem.* **2020**, *59*, 13190–13200.

[212] Boča, R. Zero-field splitting in metal complexes. *Coord. Chem. Rev.* **2004**, *248*, 757–815.

[213] Gatteschi, D.; Sessoli, R. Quantum tunneling of magnetization and related phenomena in molecular materials. *Angew. Chem. Int. Ed.* **2003**, *42*, 268–297.

[214] Freedman, D. E.; Harman, W. H.; Harris, T. D.; Long, G. J.; Chang, C. J.; Long, J. R. Slow magnetic relaxation in a high-spin iron (II) complex. *J. Am. Chem. Soc.* **2010**, *132*, 1224–1225.

[215] Ungur, L.; Chibotaru, L. F. Magnetic anisotropy in the excited states of low symmetry lanthanide complexes. *Phys. Chem. Chem. Phys.* **2011**, *13*, 20086–20090.

[216] Korchagin, D. V.; Palii, A. V.; Yureva, E. A.; Akimov, A. V.; Misochko, E. Y.; Shilov, G. V.; Talantsev, A. D.; Morgunov, R. B.; Shakin, A. A.; Aldoshin, S. M.; Tsukerblat, B. S. Evidence of field induced slow magnetic relaxation in cis-$[Co(hfac)_2(H2O)_2]$ exhibiting tri-axial anisotropy with a negative axial component. *Dalton Trans.* **2017**, *46*, 7540–7548.

[217] Amoza, M.; Maxwell, L.; Aliaga-Alcalde, N.; Gómez-Coca, S.; Ruiz, E. Spin-phonon coupling and slow-magnetic relaxation in pristine ferrocenium. *Chem. Eur. J.* **2021**, *27*, 16440–16447.

[218] Meng, Y.-S.; Mo, Z.; Wang, B.-W.; Zhang, Y.-Q.; Deng, L.; Gao, S. Observation of the single-ion magnet behavior of d^8 ions on two-coordinate Co(I)–NHC complexes. *Chem. Sci.* **2015**, *6*, 7156–7162.

[219] Lunghi, A.; Totti, F.; Sanvito, S.; Sessoli, R. Intra-molecular origin of the spin-phonon coupling in slow-relaxing molecular magnets. *Chem. Sci.* **2017**, *8*, 6051–6059.

[220] Chibotaru, L. F., et al. Spin-lattice relaxation of magnetic centers in molecular crystals at low temperature. *Phys. Rev. B* **2018**, *97*, 024427.

[221] Albino, A.; Benci, S.; Tesi, L.; Atzori, M.; Torre, R.; Sanvito, S.; Sessoli, R.; Lunghi, A. First-principles investigation of spin–phonon coupling in vanadium-based molecular spin quantum bits. *Inorg. Chem.* **2019**, *58*, 10260–10268.

[222] Albino, A.; Benci, S.; Atzori, M.; Chelazzi, L.; Ciattini, S.; Taschin, A.; Bartolini, P.; Lunghi, A.; Righini, R.; Torre, R.; Totti, F.; Sessoli, R. Temperature dependence of spin–phonon coupling in $[VO(acac)_2]$: A computational and spectroscopic study. *J. Phys. Chem. C* **2021**, *125*, 22100–22110.

[223] Datta, S. N.; Trindle, C.; Illas, F. *Theoretical and computational aspects of magnetic organic molecules*; World Scientific, 2014.

[224] Wolf, S.; Awschalom, D.; Buhrman, R.; Daughton, J.; Von Molnar, S.; Roukes, M.; Chtchelkanova, A. Y.; Treger, D. Spintronics: a spin-based electronics vision for the future. *Science* **2001**, *294*, 1488–1495.
[225] Hu, X.; Wang, W.; Wang, D.; Zheng, Y. The electronic applications of stable diradicaloids: present and future. *J. Mater. Chem. C* **2018**, *6*, 11232–11242.
[226] Sanvito, S. Molecular spintronics. *Chem. Soc. Rev.* **2011**, *40*, 3336–3355.
[227] Vela, S.; Reardon, M. B.; Jakobsche, C. E.; Turnbull, M. M.; Ribas-Arino, J.; Novoa, J. J. Bistability in Organic Magnetic Materials: A Comparative Study of the Key Differences between Hysteretic and Non-hysteretic Spin Transitions in Dithiazolyl Radicals. *Chem.: Eur. J* **2017**, *23*, 3479–3489.
[228] Gilroy, J. B.; McKinnon, S. D.; Kennepohl, P.; Zsombor, M. S.; Ferguson, M. J.; Thompson, L. K.; Hicks, R. G. Probing electronic communication in stable benzene-bridged verdazyl diradicals. *J. Org. Chem.* **2007**, *72*, 8062–8069.
[229] Abe, M. Diradicals. *Chem. Rev.* **2013**, *113*, 7011–7088.
[230] Blatter, H. M.; Lukaszewski, H. A new stable free radical. *Tetrahedron Lett.* **1968**, *9*, 2701–2705.
[231] Bazzi, F.; Danke, A. J.; Lawson, D. B.; Manoli, M.; Leitus, G.; Koutentis, P. A.; Constantinides, C. P. 1-(2-Methoxyphenyl)-3-(phenyl)-1, 4-dihydro-1, 2, 4-benzotriazin-4-yl: A Tricky "Structure-to-Magnetism" Correlation Aided by DFT Calculations. *CrystEngComm* **2020**, 4306–4316.
[232] Ciccullo, F.; Gallagher, N.; Geladari, O.; Chassé, T.; Rajca, A.; Casu, M. A derivative of the Blatter radical as a potential metal-free magnet for stable thin films and interfaces. *ACS Appl. Mater. Interfaces* **2016**, *8*, 1805–1812.
[233] Gallagher, N. M.; Bauer, J. J.; Pink, M.; Rajca, S.; Rajca, A. High-spin organic diradical with robust stability. *J. Am. Chem. Soc.* **2016**, *138*, 9377–9380.
[234] Gallagher, N.; Zhang, H.; Junghoefer, T.; Giangrisostomi, E.; Ovsyannikov, R.; Pink, M.; Rajca, S.; Casu, M. B.; Rajca, A. Thermally and Magnetically Robust Triplet Ground State Diradical. *J. Am. Chem. Soc.* **2019**, *141*, 4764–4774.
[235] Hu, X.; Chen, H.; Zhao, L.; Miao, M.; Han, J.; Wang, J.; Guo, J.; Hu, Y.; Zheng, Y. Nitrogen analogues of Chichibabin's and Müller's hydrocarbons with small singlet–triplet energy gaps. *Chem. Commun.* **2019**, *55*, 7812–7815.
[236] Hu, X.; Chen, H.; Xue, G.; Zheng, Y. Correlation between the strength of conjugation and spin–spin interactions in stable diradicaloids. *J. Mater. Chem. C* **2020**, 10749–10754, doi: 10.1039/d0tc00868k.
[237] Ovchinnikov, A. A. Multiplicity of the ground state of large alternant organic molecules with conjugated bonds. *Theor. Chim. Acta* **1978**, *47*, 297–304.
[238] Reta Mañeru, D.; Pal, A. K.; Moreira, I. d. P.; Datta, S. N.; Illas, F. The Triplet–Singlet Gap in the m-Xylylene Radical: A Not So Simple One. *J. Chem. Theory Comput.* **2013**, *10*, 335–345.
[239] Illas, F.; Moreira, I. P.; De Graaf, C.; Barone, V. Magnetic coupling in biradicals, binuclear complexes and wide-gap insulators: a survey of ab initio wave function and density functional theory approaches. *Theor. Chem. Acc.* **2000**, *104*, 265–272.
[240] Shil, S.; Herrmann, C. Performance of range-separated hybrid exchange–correlation functionals for the calculation of magnetic exchange coupling constants of organic diradicals. *J. Comput. Chem.* **2018**, *39*, 780–787.

[241] Valiev, M.; Bylaska, E. J.; Govind, N.; Kowalski, K.; Straatsma, T. P.; Van Dam, H. J.; Wang, D.; Nieplocha, J.; Apra, E.; Windus, T. L., et al. NWChem: A comprehensive and scalable open-source solution for large scale molecular simulations. *Comput. Phys. Commun.* **2010**, *181*, 1477–1489.

[242] Angeli, C.; Pastore, M.; Cimiraglia, R. New perspectives in multireference perturbation theory: the n-electron valence state approach. *Theor. Chem. Acc.* **2007**, *117*, 743–754.

[243] Barone, V.; Cacelli, I.; Ferretti, A. The role of the multiconfigurational character of nitronyl-nitroxide in the singlet–triplet energy gap of its diradicals. *Phys. Chem. Chem. Phys.* **2018**, *20*, 18547–18555.

[244] Bajaj, A.; Ali, M. E. First Principle Designing of Blatter's Diradicals with Strong Ferromagnetic Exchange Interactions. *J. Phys. Chem. C* **2019**, *123*, 15186–15194.

[245] Suaud, N.; Ruamps, R.; Guihéry, N.; Malrieu, J.-P. A strategy to determine appropriate active orbitals and accurate magnetic couplings in organic magnetic systems. *J. Chem. Theory Comput.* **2012**, *8*, 4127–4137.

[246] Malrieu, J. P.; Caballol, R.; Calzado, C. J.; de Graaf, C.; Guihéry, N. Magnetic interactions in molecules and highly correlated materials: physical content, analytical derivation, and rigorous extraction of magnetic Hamiltonians. *Chem. Rev.* **2014**, *114*, 429–492.

[247] Song, M.; Song, X.; Bu, Y. Tuning the Spin Coupling Interactions in the Nitroxide-Based Bisphenol-Like Diradicals. *ChemPhysChem* **2017**, *18*, 2487–2498.

[248] Pal, A. K.; Mañeru, D. R.; Latif, I. A.; de PR Moreira, I.; Illas, F.; Datta, S. N. Theoretical and computational investigation of meta-phenylene as ferromagnetic coupler in nitronyl nitroxide diradicals. *Theor. Chem. Acc.* **2014**, *133*, 1472.

[249] Ali, M. E.; Roy, A. S.; Datta, S. N. Molecular tailoring and prediction of strongly ferromagnetically coupled trimethylenemethane-based nitroxide diradicals. *J. Phys. Chem. A* **2007**, *111*, 5523–5527.

[250] Ko, K. C.; Cho, D.; Lee, J. Y. Systematic approach to design organic magnetic molecules: strongly coupled diradicals with ethylene coupler. *J. Phys. Chem. A* **2012**, *116*, 6837–6844.

[251] Faust, T. B.; Tuna, F.; Timco, G. A.; Affronte, M.; Bellini, V.; Wernsdorfer, W.; Winpenny, R. E. Controlling magnetic communication through aromatic bridges by variation in torsion angle. *Dalton Trans.* **2012**, *41*, 13626–13631.

[252] Ali, M. E.; Datta, S. N. Broken-symmetry density functional theory investigation on bis-nitronyl nitroxide diradicals: Influence of length and aromaticity of couplers. *J. Phys. Chem. A* **2006**, *110*, 2776–2784.

[253] Latif, I. A.; Panda, A.; Datta, S. N. Very strongly ferromagnetically coupled diradicals from mixed radical centers: nitronyl nitroxide coupled to oxoverdazyl via polyene spacers. *J. Phys. Chem. A* **2009**, *113*, 1595–1600.

[254] Ali, M. E.; Vyas, S.; Datta, S. N. Ab initio quantum chemical investigation of intramolecular magnetic interaction in some diradical derivatives of imino nitroxide and nitronyl nitroxide. *J. Phys. Chem. A* **2005**, *109*, 6272–6278.

[255] Vyas, S.; Ali, M. E.; Hossain, E.; Patwardhan, S.; Datta, S. N. Theoretical investigation of intramolecular magnetic interaction through an ethylenic coupler. *J. Phys. Chem. A* **2005**, *109*, 4213–4215.

[256] Hutchison, K.; Srdanov, G.; Hicks, R.; Yu, H.; Wudl, F.; Strassner, T.; Nendel, M.; Houk, K. Tetraphenylhexaazaanthracene: A Case for Dominance of Cyanine Ion Stabilization Overwhelming 16π Antiaromaticity. *J. Am. Chem. Soc.* **1998**, *120*, 2989–2990.

[257] Langer, P.; Amiri, S.; Bodtke, A.; Saleh, N. N.; Weisz, K.; Gorls, H.; Schreiner, P. R. 3, 5, 7, 9-Substituted Hexaazaacridines: Toward Structures with Nearly Degenerate Singlet- Triplet Energy Separations. *J. Org. Chem.* **2008**, *73*, 5048–5063.

[258] Constantinides, C. P.; Zissimou, G. A.; Berezin, A. A.; Ioannou, T. A.; Manoli, M.; Tsokkou, D.; Theodorou, E.; Hayes, S. C.; Koutentis, P. A. Tetraphenylhexaazaanthracenes: 16π Weakly Antiaromatic Species with Singlet Ground States. *Org. Lett.* **2015**, *17*, 4026–4029.

[259] Haas, Y.; Zilberg, S. Charge separation in ground-state 1, 2, 4, 5-tetra-substituted benzene derivatives. *J. Am. Chem. Soc.* **2004**, *126*, 8991–8998.

[260] Langer, P.; Bodtke, A.; Saleh, N. N.; Görls, H.; Schreiner, P. R. 3, 5, 7, 9-Tetraphenylhexaazaacridine: A Highly Stable, Weakly Antiaromatic Species with 16 π Electrons. *Angew. Chem. Int. Ed.* **2005**, *44*, 5255–5259.

[261] Braunstein, P.; Siri, O.; Taquet, J.-p.; Rohmer, M.-M.; Bénard, M.; Welter, R. A 6π+ 6π potentially antiaromatic zwitterion preferred to a quinoidal structure: Its reactivity toward organic and inorganic reagents. *J. Am. Chem. Soc.* **2003**, *125*, 12246–12256.

[262] Bendikov, M.; Duong, H. M.; Starkey, K.; Houk, K.; Carter, E. A.; Wudl, F. Oligoacenes: theoretical prediction of open-shell singlet diradical ground states. *J. Am. Chem. Soc.* **2004**, *126*, 7416–7417.

[263] Hachmann, J.; Dorando, J. J.; Avilés, M.; Chan, G. K.-L. The radical character of the acenes: a density matrix renormalization group study. *J. Chem. Phys.* **2007**, *127*, 134309.

[264] Constantinides, C. P.; Ioannou, T. A.; Koutentis, P. A. Manipulating the singlet–triplet energy gaps of arene-fused bis (1, 2, 3-dithiazoles): A computational study. *Polyhedron* **2013**, *64*, 172–180.

[265] Zhang, G.; Li, S.; Jiang, Y. Effects of Substitution on the Singlet- Triplet Energy Splittings and Ground-State Multiplicities of m-Phenylene-Based Diradicals: A Density Functional Theory Study. *J. Phys. Chem. A* **2003**, *107*, 5573–5582.

[266] Guevara-Level, P.; Pascal, S.; Siri, O.; Jacquemin, D. First principles investigation of the spectral properties of neutral, zwitterionic, and bis-cationic azaacenes. *Phys. Chem. Chem. Phys.* **2019**, *21*, 22910–22918.

[267] Shil, S.; Herrmann, C. Performance of range-separated hybrid exchange–correlation functionals for the calculation of magnetic exchange coupling constants of organic diradicals. *J. Comput. Chem.* **2018**, *39*, 780–787.

[268] Illas, F.; Moreira, I. P.; De Graaf, C.; Barone, V. Magnetic coupling in biradicals, binuclear complexes and wide-gap insulators: a survey of ab initio wave function and density functional theory approaches. *Theor. Chem. Acc.* **2000**, *104*, 265–272.

[269] Reta Maneru, D.; Pal, A. K.; Moreira, I. d. P.; Datta, S. N.; Illas, F. The Triplet–Singlet Gap in the m-Xylylene Radical: A Not So Simple One. *J. Chem. Theory Comput.* **2014**, *10*, 335–345.

[270] Shao, Y.; Head-Gordon, M.; Krylov, A. I. The spin–flip approach within time-dependent density functional theory: Theory and applications to diradicals. *J. Chem. Phys.* **2003**, *118*, 4807–4818.
[271] Yamaguchi, K. The electronic structures of biradicals in the unrestricted Hartree-Fock approximation. *Chem. Phys. Lett.* **1975**, *33*, 330–335.
[272] Head-Gordon, M. Characterizing unpaired electrons from the one-particle density matrix. *Chem. Phys. Lett.* **2003**, *372*, 508–511.
[273] Assfeld, X.; Rivail, J.-L. Quantum chemical computations on parts of large molecules: the ab initio local self consistent field method. *Chem. Phys. Lett.* **1996**, *263*, 100–106.
[274] Kaur, P.; Ali, M. E. First Principle Investigations of Long-range Magnetic Exchange Interactions via Polyacene Coupler. *Int. J. Quantum Chem.* **2021**, 1–11, doi:https://doi.org/10.1002/qua.26756.
[275] Orms, N.; Rehn, D. R.; Dreuw, A.; Krylov, A. I. Characterizing bonding patterns in diradicals and triradicals by density-based wave function analysis: A uniform approach. *J. Chem. Theory Comput.* **2018**, *14*, 638–648.
[276] Yang, H.; Chen, M.; Song, X.; Bu, Y. Structural fluctuation governed dynamic diradical character in pentacene. *Phys. Chem. Chem. Phys.* **2015**, *17*, 13904–13914.
[277] Hoffmann, R.; Zeiss, G. D.; Van Dine, G. W. The electronic structure of methylenes. *J. Am. Chem. Soc.* **1968**, *90*, 1485–1499.
[278] Constantinides, C. P.; Koutentis, P. A.; Schatz, J. A DFT study of the ground state multiplicities of linear vs angular polyheteroacenes. *J. Am. Chem. Soc.* **2004**, *126*, 16232–16241.
[279] David, G.; Guihéry, N.; Ferré, N. What Are the Physical Contents of Hubbard and Heisenberg Hamiltonian Interactions Extracted from Broken Symmetry DFT Calculations in Magnetic Compounds? *J. Chem. Theory Comput.* **2017**, *13*, 6253–6265.
[280] Grau-Crespo, R.; Corà, F.; Sokol, A. A.; de Leeuw, N. H.; Catlow, C. R. A. Electronic structure and magnetic coupling in $FeSbO_4$: A DFT study using hybrid functionals and GGA + U methods. *Phys. Rev. B* **2006**, *73*, 035116.
[281] Nakano, M. Electronic structure of open-shell singlet molecules: Diradical character viewpoint. *Top. Curr. Chem.* **2017**, *375*, 47.
[282] Rottschäfer, D.; Busch, J.; Neumann, B.; Stammler, H.-G.; Van Gastel, M.; Kishi, R.; Nakano, M.; Ghadwal, R. S. Diradical Character Enhancement by Spacing: N-Heterocyclic Carbene Analogues of Müller's Hydrocarbon. *Chem. Eur. J.* **2018**, *24*, 16537–16542.
[283] Hammett, L. P. The effect of structure upon the reactions of organic compounds. Benzene derivatives. *J. Am. Chem. Soc.* **1937**, *59*, 96–103.

List of Publications

Publications included in thesis

- **Khurana, R.**; and Ali, M.E., "Single-molecule magnetism in linear Fe(I) complexes with Aufbau and non-Aufbau ground-states" *Inorg. Chem.*, **2022**, *61*, 15335-15345.

- **Khurana, R.**; Bajaj, A.; and Ali, M.E., "Tuning the magnetic properties of diamagnetic di-Blatter's zwitterion to antiferro- and ferromagnetic coupled diradicals" *Phys. Chem. Chem. Phys.*, **2022**, *24*, 2543-2553.

- **Khurana, R.**; Gupta, S.; and Ali, M.E., "First-principles investigations of magnetic anisotropy and spin-crossover behavior of Fe(III)-TBP complexes" *J. Phys. Chem. A*, **2021**, *125*, 2197-2207.

- **Khurana, R.**; Bajaj, A.; and Ali, M.E., "How plausible is getting ferromagnetic interactions by coupling Blatter's radical via its fused benzene ring?" *J. Phys. Chem. A*, **2020**, *124*, 6707–6713.

Publications not a part of thesis

- Nain, S.; **Khurana, R.**; and Ali, M.E., "Harnessing colossal magnetic anisotropy in sandwiched $3d^2$-metallocenes" *J. Phys. Chem. A*, **2022**, *126*, 2811–2817.

- Bajaj, A.†; **Khurana, R.**†; and Ali, M.E., "Auxiliary atomic relay center facilitates enhanced magnetic couplings in Blatter's radical" *J. Phys. Chem. A*, **2021**, *125*, 4133-4142. †Equal contribution

- Bajaj, A.; **Khurana, R.**; and Ali, M.E., "Quantum interference and spin filtering effects in photo-responsive single molecule devices" *J. Mater. Chem. C*, **2021**, *9*, 11242-11251.

- **Khurana, R.**; Bajaj, A.; and Ali, M.E., "High-spin triradicals based on Blatter's radical" (In Manuscript).

Author's Biography

Rishu Khurana (Reg. No. **PH19210**) joined the **Institute of Nano Science and Technology, Mohali** (INST-Mohali) in July 2019 for her doctoral dissertation by research and registered at the **Indian Institute of Science Education and Research Mohali** (IISER-Mohali) for the award of the ***Degree of Doctor of Philosophy***. She earned her Bachelor of Science (Chemistry, Physics, and Mathematics) degree and Master of Science (Chemistry) degree with Gold medal from Mukand Lal National College, Kurukshetra University, Kurukshetra. Her scientific expertise and area of research include: *ab initio* investigation of magnetic anisotropy and isotropic magnetic exchange interactions of magnetic molecules for high-density data-storage and molecular spintronics devices.